Fatigue in flood gates due to dynamic wave loading

A probabilistic design method

by

T.N.J. Kleiberg

in partial fulfilment of the degree of Master of Science
at the Delft University of Technology,
to be defended publicly on Tuesday June 29, 2021 at 14:30 AM.

Student number:	4443411	
Project duration:	September 1, 2020 – June 29, 2021	
Thesis committee:	Dr. ir. B. Hofland,	TU Delft, chair
	Ir. O. C. Tieleman,	TU Delft, supervisor
	Ir. M. Versluis,	Witteveen+Bos
	Ir. E. ten Oever,	BAM Infraconsult
	Dr. ir. P. van der Male	TU Delft

TU Delft

Witteveen+Bos

Preface

This master thesis is submitted in partial fulfilment of the Hydraulic Engineering track of the Master of Science in Civil Engineering at the Delft University of Technology. The work has been conducted as part of an internship at Witteveen+Bos, to whom I am very grateful for their support and the opportunity to pursue this topic.

Despite the challenging circumstances created by the COVID-19 pandemic my supervisors, Marco Versluis and Orson Tieleman, were always available for feedback and discussions and their guidance has greatly benefited my ability to keep making progress while confined at home.

Similarly I would like to thank the rest my thesis committee, Dr. Bas Hofland, Erik ten Oever, and dr. Pim van der Male, for their input and constructive criticism during our online meetings. Their enthusiasm and knowledge was invaluable for keeping my work focused and on the right track. Finally a special thanks to Wim Kortlever from Rijkswaterstaat who joined the committee in an unofficial capacity to offer advice about current engineering practices, and Ruben Vorderegger for his help with implementing the SCIA model.

T.N.J. Kleiberg
Delft, June 2021

Contents

Nomenclature

Physics Constants		
ν	Poisson's ratio steel	–
ρ_s	steel density	kg/m^3
ρ_w	sea water density	kg/m^3
E_s	Young's modulus steel	MPa
g	gravity constant	m/s^2
System properties		
$\Delta\sigma_c$	detail category	N/m^2
γ_{Ff}	fatigue load safety factor	–
γ_{Mf}	material safety factor	–
ζ	damping ratio	–
c_r	reflection coefficient	–
F	wind fetch	m
f_yd	yield strength	MPa
h_G	gate height	m
h_L	lake water level	m
L_y	overhang length	m
l_{eff}	effective weld length	m
L_{girder}	horizontal stiffener length	m
L_{web}	vertical stiffener length	m
m_G	gate mass	kg
t_G	skin plate thickness	m
t_v	vertical stiffener thickness	m
t_h	horizontal stiffener thickness	m
W	gate width	m
Variables		
α	wave phase	rad
α_J	energy scale parameter	–
β	compressibility correction factor	–
δ	Vanmarcke parameter	–
$\Delta\sigma_D$	constant amplitude fatigue limit	N/m^2
$\Delta\sigma_L$	cut-off limit	N/m^2
$\Delta\sigma_{eq}$	equivalent stress range	N/m^2
γ	peak enhancement factor	–
ω	radial frequency	rad/s
ω_p	peak radial frequency	rad/s
$\rho_{h_S,U_{10}}$	Pearson correlation coefficient	–
σ	normal stress	N/m^2
σ_p	principal stress	N/m^2
$\sigma_{a,b}$	spectral width parameter	–
τ	wave impact duration	s
a	wave amplitude	m
A_m	modal coordinate	–
$C_{\%}$	relative modal stress contribution	%
C_{ts}	T_p to t_s ratio	–
D	fatigue damage factor	–
D_S	signal duration	s
D_E	expected lifetime fatigue	–
D_L	simulated lifetime fatigue	–
E_J	JONSWAP energy spectrum	m^2/Hz
E_{TMA}	TMA energy spectrum	m^2/Hz
f	frequency	Hz
f_H	probability density of h_S	–
f_J	joint pdf of h_S and U_{10}	–
f_N	Nyquist frequency	Hz
f_U	probability density of $U10$	–
f_{max}	Highest analysis frequency	Hz
FRF_m	frequency response function	–
H	wave height	m
h_S	still sea water level	m
H_{m0}	significant wave height	m

h_{SLR}	sea level rise	m	q_{ij}	average pressure on section i,j	N/m^2
k	wave number	rad/m	R	response spectrum	N/m^2
L_w	wave length	m	RI	relative fatigue importance	%
m	mode	–	S_a	amplitude spectrum	m
m_n	nth order spectral moment	$Hz^n m^2$	$S_{p,m}$	principal stress response mode	N/m^2
n	number of load cycles	–	T	wave period	s
N_c	load cycle capacity	–	t	time	s
N_G	number of wave height groups	–	T_p	peak wave period	s
n_G	wave group occurrences	–	t_s	sampling interval	–
n_m	Number of modes	–	T_L	fatigue lifetime	a
N_{tot}	total amount of waves	–	T_{m02}	average wave period	s
$n_{x/z}$	Number of gate subdivisions	–	U_w	vertical wave impact velocity	m/s
$n_{x/z}$	number of gate subdivisions	–	U_{10}	wind velocity at 10m+NAP	m/s
p_{hs}	hydrostatic pressure	N/m^2	w	deflection	m
P_{im}	pressure impulse	Ns/m^2	W_m	displacement response mode	m
p_{im}	impulsive wave pressure	N/m^2	res$_{h_S}$	case resolution for h_S	m
p_{qs}	quasi-static pressure	N/m^2	res$_{U_{10}}$	case resolution for U_{10}	m/s

Summary

The ability to predict the fatigue of flood gates due to dynamic wave loading is becoming increasingly important as coasts and waterways worldwide are being reinforced to suit a changing climate. There are few comprehensive ways to do so however, which often leads to conservative estimates and therefore cost-inefficient designs. This thesis presents an integral framework with which the fatigue of flood gates due to dynamic wave loading can be described in much more detail, while also being efficient and adaptable to different circumstances. It considers the entire wave spectrum rather than individual waves, takes higher response modes into account, models the full fluid-structure interaction, and models the lifetime probabilistically rather than as a set of normative events.

The problem is split into smaller self-contained modules, which are then combined to answer the main question. The first set of modules aims to solve the fatigue experienced by a single load event based on readily available data. This was done by creating a wave spectrum from the site properties, average wind velocity, and average water level, and using that spectrum to generate random realisations of wave load spectra on the gate by employing the random phase-amplitude model. These wave loads can then be transformed to pressure spectra which will dynamically excite the fluid-structure system. The pressures were split up into a quasi-static and an impulsive part. The quasi-static pressures were solved with linear wave theory, while the impulsive pressures due to the overhang were found using Wood & Peregrine pressure-impulse theory.

The gate is then parametrically modelled in a FEM software package in order to export the in-vacuo response modes. These are combined with the fluid-structure interaction model from Tieleman et al. [33] to derive the response of the fluid-structure system to external pressures. Discretising and multiplying the previously derived pressure spectra then gives the response of the system for a particular load event.

The fatigue was evaluated with both the standard Eurocode method and a common spectral method for comparison, and results in a fatigue damage factor which shows what fraction of the materials fatigue capacity is depleted by the imposed load. This concludes the section on the fatigue to a single load event.

Next, the load events imposed on the gate over its lifetime were probabilistically defined. This was done by fitting two independent probability distributions to historical wind- and water level data, the latter of which was also adjusted for climate change. These probability distributions are then split into segments which are integrated to obtain discrete load cases with representative values for the average wind velocity, water level, and probability of occurrence. Two filters were also applied to remove the load cases which cause a negligible amount of fatigue over the lifetime of the gate.

Computing the fatigue damage caused by the average values of each of these load case bins then gives a set of fatigue damage factors with an associated probability of occurrence, which can be used to perform a Monte Carlo analysis (or direct integration). From this analysis an expected lifetime can be determined.

A case study for a hypothetical parametrically defined gate with an overhang located in the Afsluitdijk was performed, where the response for different gate configurations and environmental conditions was evaluated. The fatigue response was evaluated for fatigue across the gate, at the critical coordinate, and per mode. A ULS check was also done for the chosen design. Results following from the model were also compared to those of methods commonly used in practice.

The method gives insight into the relative importance of different modes and load events, can compute fatigue for the entire gate or just a critical coordinate, and does so in a much more time-efficient manner than current numerical models. It gives a more comprehensive view of the fatigue over the lifetime of the gate by modelling its entire lifespan rather than a set of design load events. The modular structure of the integral framework allows for easy adaptation to other use cases in hydraulic engineering where fatigue due to hydrodynamic loading is of interest.

1

Introduction

Flood gates are commonly used in storm surge barriers and discharge sluices to regulate discharges and prevent flooding. During low tide water is pumped or allowed to flow freely through them out to sea, while during storms they keep out the high water levels and waves attacking the structure from the sea. Many of these complexes are ageing, and increased flood safety standards have made renovations or replacements necessary. As sea levels rise drainage windows become shorter and the hydraulic loads larger. New complexes such as the revamped Afsluitdijk discharge facilities will therefore be outfitted with pumps and more drainage capacity to be able to continue discharging water if necessary, and outfitted with better gates to be able to withstand these higher loads.

These gates are embedded in a larger structure, which sometimes encloses them in a covered recess. The previous Afsluitdijk design for example included a defence beam which acted as an overhang in front of the gate. It has been removed in the new design because it caused an unexpected amount of extra pressures an vibrations in the system, which accelerated its structural degradation. When a wave hits the gate it reflects and crashes into the bottom of the overhang, which causes complex interactions between the hydrodynamic pressures, vibrations of the gate, and constraints imposed by the overhang. While it won't be relevant for the new Afsluitdijk design, the behaviour of these systems is important to understand in order to properly design systems where overhangs can't be avoided.

Pressures caused by this fluid-structure interaction with the overhang can be unpredictable, and similarly the long- and short-term loads acting on the system are subject to a lot of variation and uncertainty. This means a probabilistic assessment of how the accumulation of these loads cause fatigue failure could add a lot of value and create a more accurate representation of the problem. While designing flood gates a well-supported assessment of this failure mode is crucial to create a cost-effective structure which can resist the ever increasing demands imposed on it. Formulating a method which can give a fatigue assessment for any set of boundary conditions and system properties will therefore be the main goal of this thesis.

Figure 1.1: Cross-section of new Afsluitdijk

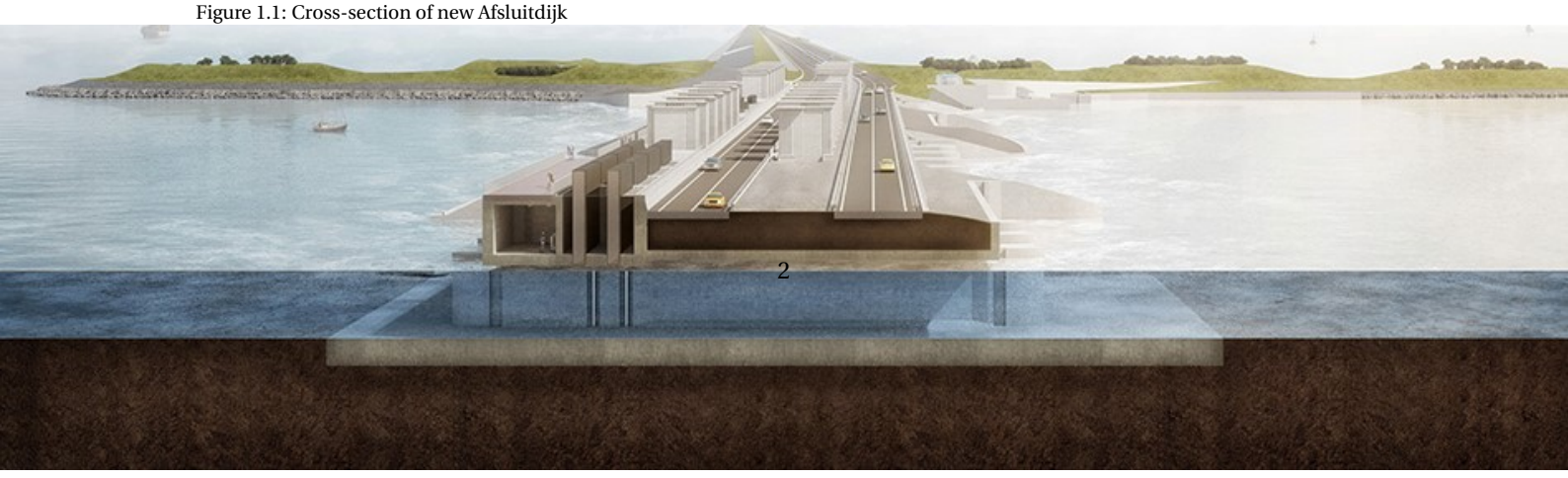

2

Problem statement and approach

This section will describe the main goal of the thesis and the intermediate problems that have to be solved in order to achieve it. These problems will then be condensed into research questions.

2.1. Problem statement

Flood gates are exposed to a range of time-varying loads such as waves impacts, tides, storm set-up, and climate change effects. A method which sets out to describe the fatigue behaviour of flood gates will have to include a description of how to probabilistically model these parameters and their uncertainties. The method should only rely on data which is either already available or can reasonably be obtained.

Subsequently, the response of the gate-fluid system to these loads has to be determined. Current methods are often fragmentary, not user-friendly, and reliant on slow numerical simulations. A promising new model for evaluating stresses in flood gates immersed in fluids, developed in Tieleman et al. [33] and expanded to include non-homogeneous gate shapes in Vorderegger [36], does this accurately and efficiently. It enables the evaluation of large number of simulations and therefore a probabilistic assessment, but so far this method has only been applied to calculate structural failure due to peak loads. A fatigue assessment would not be limited to a number of repetitions of an extreme load event, but the entire lifetime of the structure. This means that these models will have to be adapted in a way which enables the user to simulate more load events without the computation time becoming unacceptably long.

Finally, once the response of the gate to a given load event has been derived it has to be converted to a fatigue damage factor. These fatigue damage factors than have to be calculated for the entire lifetime of the gate and probabilistically combined to determine whether the gate design is sufficient. The final result will be a probabilistic assessment of whether the gate is prone to fatigue failure under the given environmental conditions, or whether the design could be more cost-efficient. Furthermore it should be modular, so that specific sections can be replaced with more in-depth alternatives if necessary.

2.1.1. Research questions

The problem statement gives rise to a set of overarching and intermediate questions which will have to be answered in order to achieve the goal of the thesis. The main research question is:

> How can a more efficient and modular framework be developed which accurately predicts the fatigue failure due to wave impacts of flood gates with an overhang?

The sub-questions following from the main question are:

I) Which hydraulic boundary conditions are relevant and how can they be obtained and probabilistically modelled?

II) How can the hydrodynamic pressures on the gate be derived from the boundary conditions?

III) What are the internal gate stresses associated with these pressure spectra?

IV) How much fatigue damage do these internal gate stresses cause?

V) How can the fatigue lifetime of the structure be accurately predicted?

VI) How sensitive is the model to statistical uncertainties and changes in the model parameters?

2.2. Report structure

The thesis will follow a modular approach to answer the research questions. Each module start with a given set of inputs and produces an output which will be used as input in the following module. The techniques employed in the individual modules can be swapped out for different methods, as long as the input and output variables stay the same. The first four modules will determine the fatigue damage caused by a single load event. Afterwards a method is presented to apply this process to a set of probabilistic boundary conditions to find the fatigue over the lifetime of a flood gate. The modules are as follows:

1 **Wave field description**
First, the wave field will be defined with the use of a spectrum in order to describe the water level fluctuations at the location of the gate under any combination of environmental conditions like the wind velocity and average water level. Certain simplifications and assumptions will be made to be able to create wave amplitude spectra from readily available data by using the appropriate wave theory for the situation under consideration.

2 **Hydrodynamic pressures**
Water surface fluctuations described by the wave amplitude spectra impose two types of pressure on the system, which will require different methods to describe. These are the pressures caused by the pulsating water level fluctuations against the surface of the gate, and the impulsive pressures caused by the water surface hitting the overhang. The latter will be much shorter and cause a highly dynamic response in the system.

3 **Structural response**
In order to turn these pressures applied to the gate surface into internal stresses, an efficient method which replicates the dynamic behaviour of the fluid-structure system should be applied to a numerical representation of the gate. The model will be coupled with an FEM model for this purpose, but in a way which minimises the amount of computation time required. The result will be a response spectrum for each gate coordinate.

4 **Structural fatigue**
By using prevailing fatigue standards, the response spectra will either be transformed into a time series with an inverse Fourier transform and evaluated based on the amount of stress cycles, or with suitable frequency domain methods. The resulting fatigue damage factor shows how much of the fatigue capacity is depleted due to the considered load event.

5 **Probabilistic boundary conditions and lifetime fatigue**
Based on the defined input parameters and available data, (correlated) probability distributions are created to describe the probability that a given load event occurs, and discretized in a way which allows a large amount of simulations to be performed without losing a significant amount of accuracy. The discretized load cases and their probability of occurrence are computed, which gives a set of fatigue damage factors and their associated probabilities. Using a Monte Carlo simulation, the entire lifetime of the gate is simulated repeatedly by picking load events based on their probability of occurrence and adding the damage factors.

6 **Case study**
Finally, the method described in the previous chapters is applied to a hypothetical case study based on the Afsluitdijk to demonstrate how it can be used to analyse and design a flood gate.

A graphical overview of the report structure is shown in Figure 2.1.

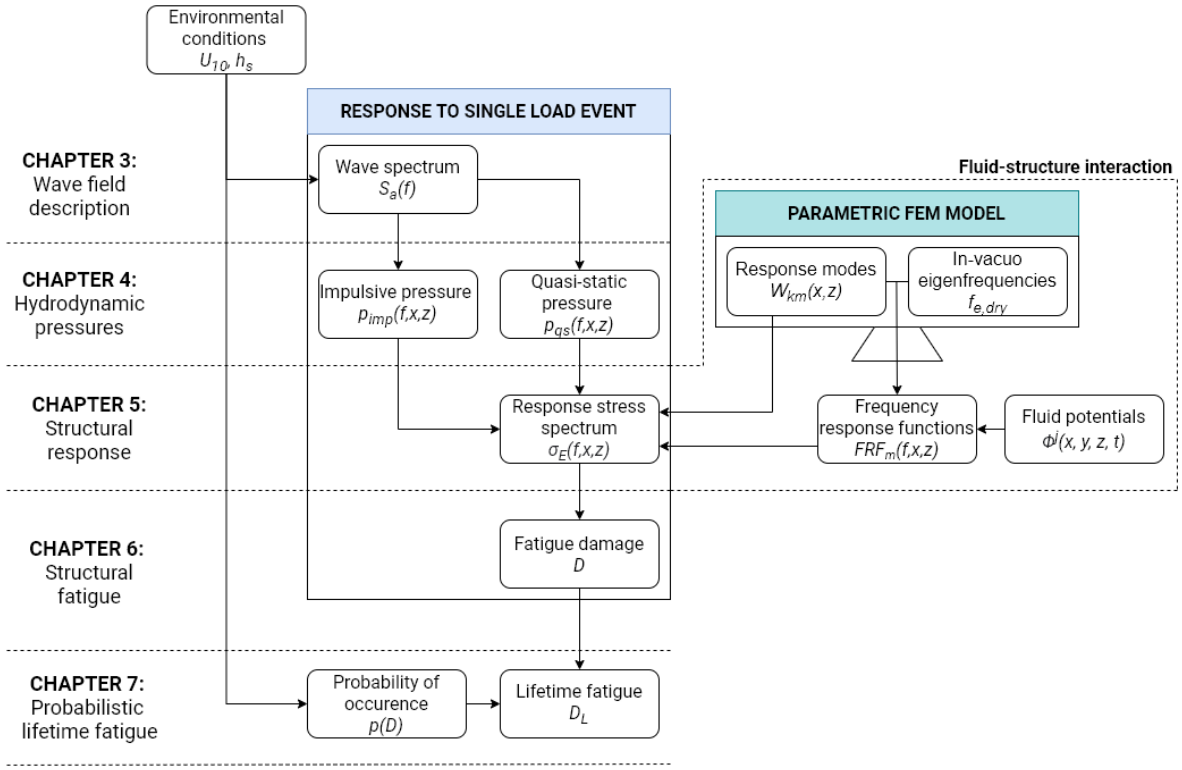

Figure 2.1: Structure of the report. Each chapter is associated with a specific module.

2.3. System description

Before proceeding with the model, the general shape of the system and some important parameters will be introduced. The flood gate under consideration is situated on the seaward-facing side of a large dam. Its height and width are given by h_G and W respectively. In front of the gate there is a short, closed, and rigid overhang with length L_y, which sufficiently high waves will crash into. Beyond the overhang lies the sea, which for the purposes of the hydrodynamic response stretches to infinity in both the x and y directions. The sea is assumed to be shallow and h_S meter deep everywhere. Waves are locally generated by the wind velocity at 10m+NAP, U_{10} and their loads are assumed to be motion-independent (other fluctuation will be discussed in Chapter 3). On the other side of the gate lies a discharge sluice, which is connected to a lake with a controlled water level. The channel is constrained by two rigid walls on either side, and equally wide as the gate. The water levels of the sea and lake are given by h_S and h_L. For the hydrodynamic response this channel is also assumed to be infinitely long in the y-direction.
The gate can deflect in the y-direction ($w(x,z)$), and is only supported at its sides at $x = 0$ and $x = W$. The top and bottom of the gate are free to move.

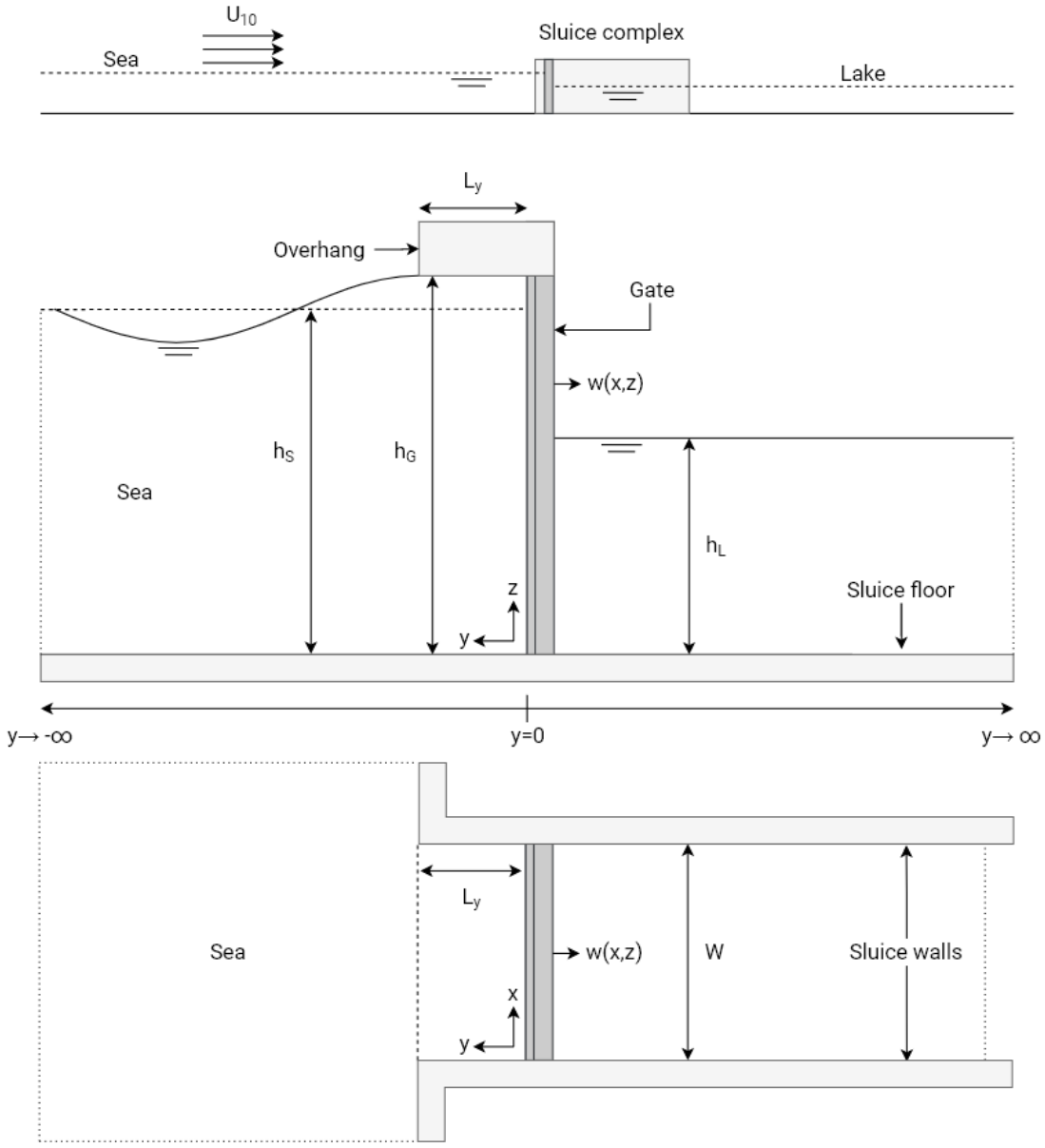

Figure 2.2: Cross-sections and important parameters of the system

3

Wave field description

The goal of this module is to describe how the boundary conditions of system will be defined, and how they can be used to generate a wave field description which describes the fluctuations of the water level.

3.1. Background

In Dutch engineering practice the wave loads imposed on a structure for a fatigue analysis are almost always derived from a set of normative storm events, each of which is defined by a return period, storm duration D_S, mean water level h_S, and a significant wave height H_{m0}. The way in which these design storms are chosen will be further discussed in Chapter 7; what is of interest for this chapter is how such an event is transformed into a series of waves. There is no universal design standards for how this should be done, but one commonly applied method will be briefly summarised here. Some issues will be highlighted, and in Section 8.7 an example of a full fatigue assessment will be worked out and compared to the spectral method described in the upcoming chapter.

For a given storm event the prevalence of different wave heights H within this design storm is given by a Rayleigh distribution (Groenendijk [11]).

$$f_R(H) = \frac{4H}{H_{m0}^2} e^{-2(\frac{H}{H_{m0}})^2} \tag{3.1}$$

This probability distribution is then discretised into N_G groups, as shown in Figure 3.1, which gives a discrete set of average wave heights which can be evaluated separately.

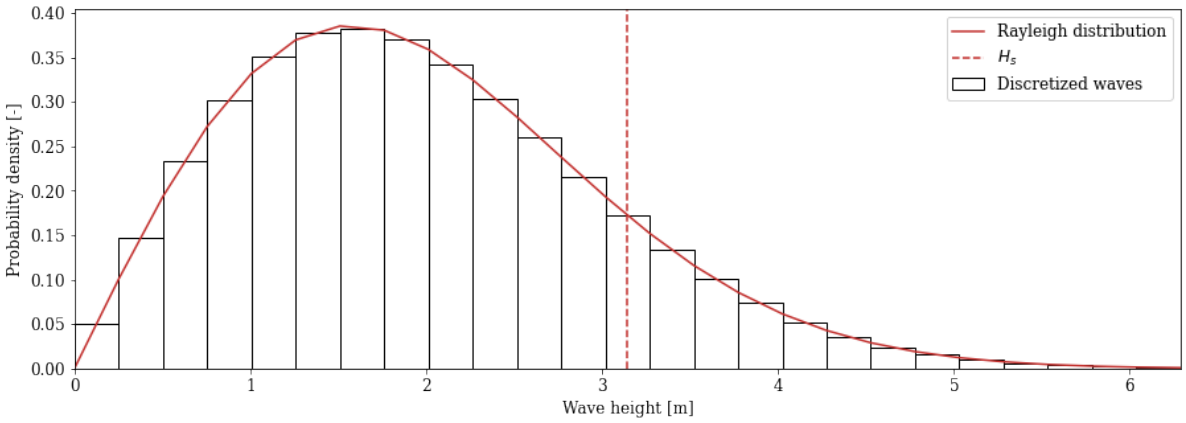

Figure 3.1: Continuous and discrete probability distributions of wave heights

The response to each of these N_G representative waves is multiplied with how many of them are expected to occur over the duration the storm event, according to the Rayleigh distribution:

$$n_{G,i} = \cdot p(H_{m0,i} < H < H_{m0,i+1}) \cdot N_{tot} \tag{3.2}$$

Where $n_{G,i}$ is the amount of times a specific wave height is expected to occur during the period D_S, and N_{tot} is the total amount of wave peaks occurring during that time.
Some problems with this method are:

- The storm duration D_S is uncertain and also hard to define because storms rarely have discrete beginnings and ends.
- The wave period T associated with each of the individual waves has a large effect on the result but is also very uncertain.
- For larger waves the structural response has likely not damped out before the next wave arrives, which means the impacts can reinforce each other. By calculating each wave individually this wave train effect is lost.
- No straightforward way to include waves other than locally generated wind waves, e.g. swell waves.
- Slower than the method presented in this report for the same level of accuracy, especially when probabilistic effects have to be accounted for.

Because the fluid-structure interaction model from Tieleman et al. [33] can resolve the response of the system in the frequency domain rather than as a time series, defining the wave inputs as random realisations of a wave spectrum is a promising alternative to the method described above. Besides being faster, evaluating the entire wave spectrum at once also takes wave train effects into account and does away with the need to assign each wave its own period. The need for design storm events is also superseded, but this will be further explained in Chapter 7.

3.2. Wave spectra

A wave spectrum describes the water surface as a stochastic process rather than as a single observation. All possible sea states are contained in the spectrum, and can be derived from it with a random-phase/amplitude model. This is because every observation of water level fluctuations can be described as a sum of a large number N harmonic wave components:

$$\eta(t) = \sum_{i=1}^{N} a_i cos(2\pi f_i t + \alpha_i) \tag{3.3}$$

where a_i and α_i are respectively the amplitude and phase associated with the frequencies $f_i = i \cdot \Delta f \quad (i = 1,2,3,...$ and $\Delta f = 1/D_S)$. Performing a Fourier analysis on this record gives the values of the amplitude and phase for each frequency. Plotting them against the frequency then gives the amplitude (a) and phase (α) spectra for this record, as shown in Figure 3.2.

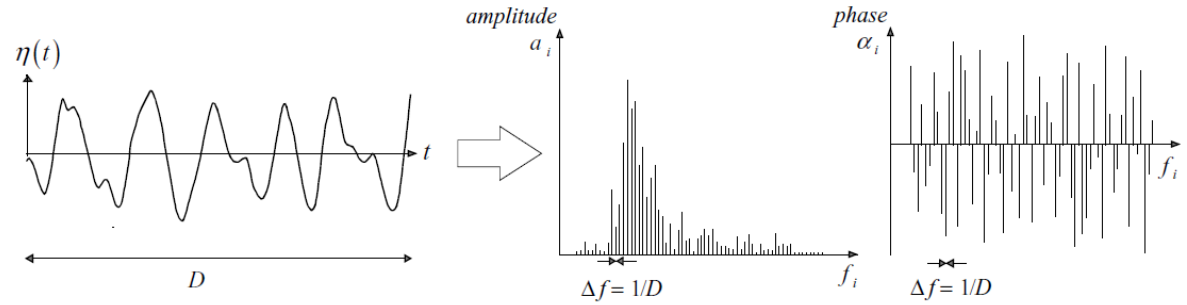

Figure 3.2: A water surface observation and its amplitude and phase spectra (Holthuijsen [14])

Over a large number of observations and with a spectral resolution Δf close to zero, the phase spectrum will approach a uniform distribution for non-steep waves and the amplitude spectrum a certain spectral shape characterised by a set of shape parameters. Steep waves and the definition of these shape parameters will be discussed in Section 3.3. The spectral shapes are usually defined in terms of variance density rather than amplitude, which requires one final transformation:

$$E(f) = \lim_{\Delta f \longrightarrow 0} \frac{1}{2\Delta f} \overline{a}^2 \tag{3.4}$$

3.3. Wave spectrum shape

In the North Sea the variance density spectrum as a function of the radial frequency ω is usually based on the JONSWAP-spectrum[13], which itself is an adaptation of the Pierson-Moskowitz spectrum. It defines the variance density based on a set of shape parameters, the wind velocity U_{10}, and the wind fetch F. The wave state is assumed to be fully developed. The equations used to create the JONSWAP-spectra $E_J(\omega)$ are given in 3.5.

$$E_J(\omega) = \alpha_J g^2 \omega^{-5} \exp\left[-\frac{5}{4}\left(\frac{\omega}{\omega_p}\right)^{-4}\right] \gamma^{\exp\left[-\frac{1}{2}\left(\frac{\omega/\omega_p - 1}{\sigma_{a,b}}\right)^2\right]} \tag{3.5}$$

For the shape parameters (peak enhancement factor γ, spectral width parameter $\sigma_{a,b}$, dimensionless peak frequency $\widetilde{f}_p$, and energy scale parameter α_J). There are competing theories for which values are most accurate, but the parametric definitions by Lewis and Allos [19] will be used in this report:

$$\widetilde{f}_p = 2.18\left(\frac{gF}{U_{10}^2}\right)^{-0.27} \tag{3.6}$$

$$\alpha_J = 0.0317\widetilde{f}_p^{0.67} \tag{3.7}$$

$$\omega_p = 2\pi\widetilde{f}_p\frac{g}{U_{10}} \tag{3.8}$$

$$\gamma = 5.87\widetilde{f}_p^{0.86} \tag{3.9}$$

$$\sigma_{a,b} = \begin{cases} 0.0547\widetilde{f}_p^{0.32} & \omega \le \omega_p \\ 0.0783\widetilde{f}_p^{0.16} & \omega > \omega_p \end{cases} \tag{3.10}$$

Figure 3.3 shows a few examples for different U_{10} and a fetch of 30km. The dashed lines indicate the peak period T_p.

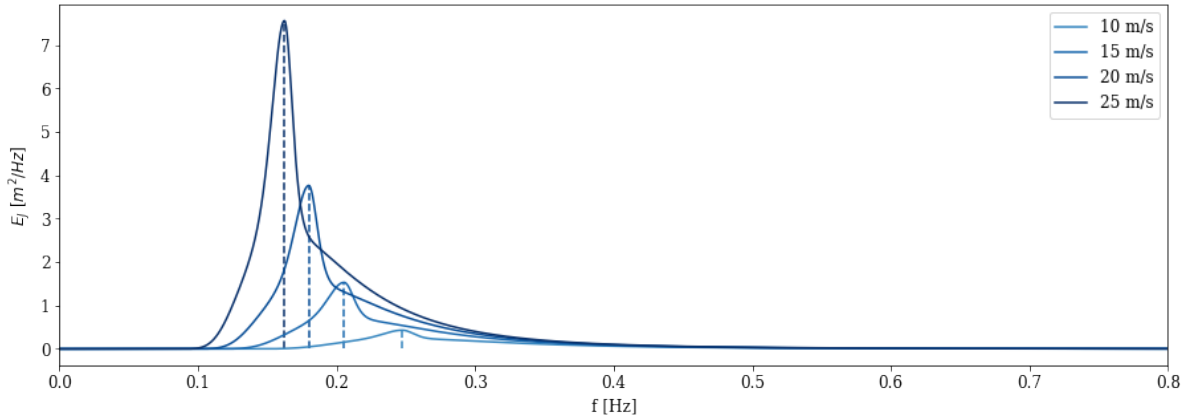

Figure 3.3: JONSWAP amplitude spectra for different wind velocities.

The size and the resolution of the spectra are determined by the sampling interval t_s and the duration of the signal D_S. A shorter sampling interval will increase the Nyquist frequency ($f_N = \frac{1}{2t_s}$) (the highest resolvable frequency). Longer segments will increase the resolution of the frequency spectrum ($\Delta f = 1/D_S$). Because the energy of the JONSWAP spectrum is concentrated in a predictable range which increases with the T_p found in Figure 3.3, the error caused by the trade-off between computational efficiency and accuracy can be quantified.

The signal duration is set at 1 hour because this is the interval for which the statistical boundary conditions are defined (the reasons for this are discussed in Chapter 7). To test the effect of different t_s on the resulting spectrum it was computed for an array of sampling intervals and peak periods, characterised by a ratio $C_{ts} = \frac{T_p}{t_s}$. The highest of these was made impractically precise at $C_{t_s} = 10.000$ to serve as a reference point. The spectra were then integrated to find their total energy, and compared.

Because the wave spectrum has a long tail, using a shorter sampling interval (and therefore higher f_N) will capture more of the spectral energy. Plotting the total energy of the spectrum as a function of T_p/t_s shows

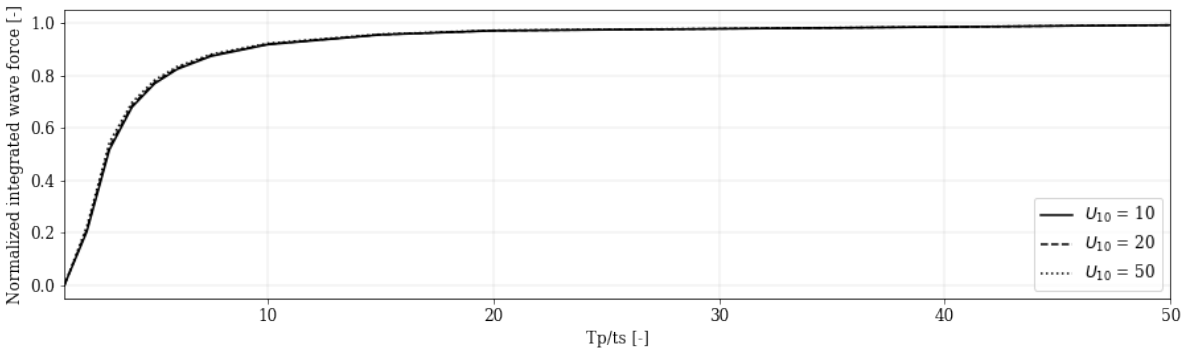

Figure 3.4: Normalized spectral energy as function of T_p/t_s for different wind loads.

that the accuracy follows the same curve for all T_p. The optimal computationally efficient ratio C_{t_s} is chosen at 30. At this point the integrated spectral energy captures 99% of the energy obtained from the reference ratio of 10.000 while the computation time keeps rising with rapidly diminishing returns.
The JONSWAP-spectrum was defined for open sea however, and does not necessarily apply to shallow waters. To better model those, an adapted version of the JONSWAP-spectrum can be used. The TMA-spectrum defined in Bouws et al. [7] is suitable for this purpose. It is obtained by multiplying the JONSWAP spectrum by a non-dimensional shape function $\phi(f, h_S)$:

$$E_{TMA}(f) = \phi(f, h_S) \cdot E_J(f) \tag{3.11}$$

$$\phi(f, h_S) = \left(\frac{k(f, h_S)}{k(f, \infty)} \right)^{-3} \frac{\frac{\delta k(f, h_S)}{\delta f}}{\frac{\delta k(f, \infty)}{\delta f}} \tag{3.12}$$

where $k(f, h_S)$ is the wave number for a given water depth and frequency. It can be found by solving the transcendental equation given in 3.13. For deep water this expression simplifies to $(2\pi f)^2 = kg$. The factor $\phi(f, h_S)$ and its effect on a normalised JONSWAP spectrum are plotted in Figure 3.5.

$$(2\pi f)^2 = kg \cdot \tanh(kh_S) \tag{3.13}$$

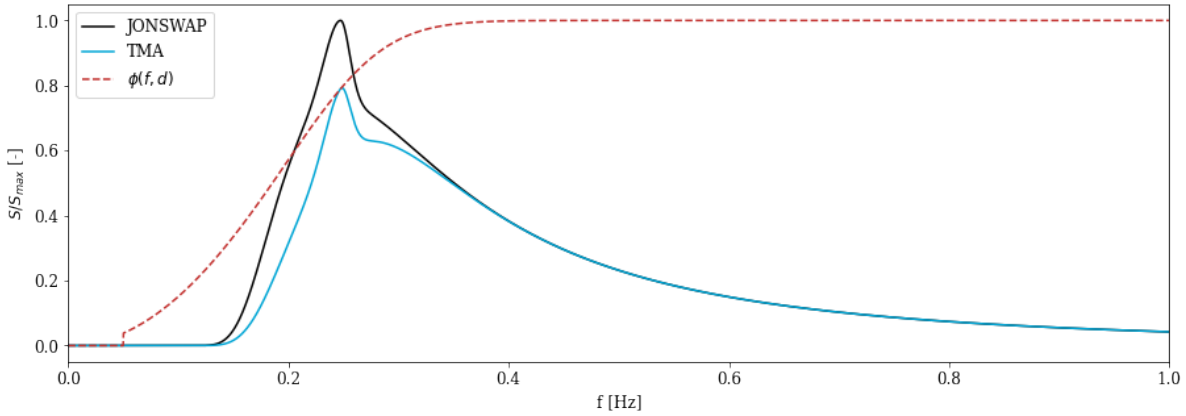

Figure 3.5: A JONSWAP amplitude spectrum and the corresponding TMA spectrum for $h_S = 7.5m$ and $U_{10} = 25m/s$

This spectral shape will be used to characterise the wind waves at the location of the gate. However by defining it this way some implicit simplifications are made. These will be briefly summarised here, and could be accounted for in later iterations to make the model more accurate:

- **Wave steepness/non-linearity**
  Wave steepness refers to the non-linear shape waves tend to take on due to gravity. It can be described

by higher-order theories such as Stokes expansions or cnoidal theory, depending on how large the waves are compared to the local depth (see Figure 3.6). The internal stress calculations employed in this report are able to calculate non-linear waves just as well as linear ones. The wave impacts will likely be larger because steeper waves have higher peaks and deeper troughs.

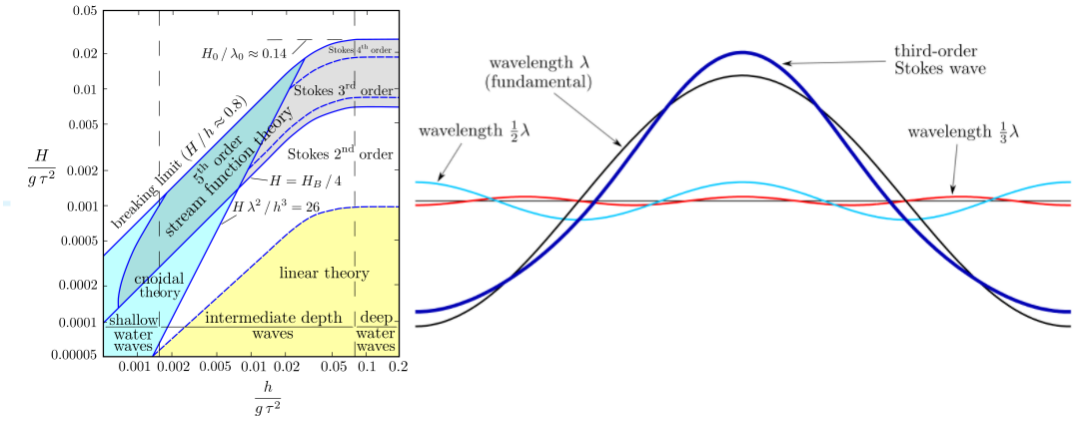

Figure 3.6: Left: Wave theories and their regions of applicability [18] [14]. Right: Non-linear wave example

- **Approach angle**
  Because wind is rarely unidirectional and complex wave interactions and sea floor geometry cause scattering, waves hitting a structure tend to approach from a range of directions. Even though the methods employed in this report can theoretically also model oblique wave impacts, they haven't been validated for this purpose. Furthermore these gates are usually recessed into the dam, which limits the possible angles of approach. Due to refraction most of the wave energy also tends to be concentrated in the direction perpendicular to the dam. Therefore the situation is simplified and all waves are assumed to approach the gate perpendicularly.

- **Swell**
  Not all waves are generated locally; some are created in far-away storms and can travel long distances before reaching the shore. These so-called swell waves have longer periods than locally generated wind waves (See Figure 7.1). For seas which are not connected to a larger body of water these can be assumed to play no significant part in the hydraulic loads. Their long periods are also unlikely to cause a dynamic response due to the slow loading- and unloading cycles. Wave spectrum descriptions which do include swell are available, such as for example the work by Ochi and Hubble [27].

3.4. Random phase model

For the random phase model the variance density spectrum will first be converted to an amplitude spectrum (inverse of Eq. 3.4).

$$S_a(f) = \sqrt{E_{TMA}(f) \cdot 2\Delta f} \tag{3.14}$$

This spectrum describes the amplitude a_i associated with a frequencies f_i in Eq.3.15. All that is needed to generate random instances of the spectrum is to add the phases. Because the rest of the model is also going to work in the frequency domain converting back and forth with Fourier transforms isn't necessary. The uniformly distributed random phase can also be added to $S_{a,r}(f)$ in the frequency domain:

$$S_{a,\phi}(f) = S_a(f) \cdot e^{-i \cdot U(0,2\pi)} \tag{3.15}$$

Where $U(0,2\pi)$ refers to a uniform distribution from 0 to 2π. This is equivalent to adding the phases to equation 3.15. Finally, the spectrum is multiplied with a reflection coefficient c_r, which depends on the geometry of the structure. A coefficient of 0 would mean zero reflection whereas a coefficient of 1 refers to full wave reflection, which doubles the amplitude of the wave at the gate. A rigid vertical gate will give almost full reflection, but due to interference by the overhang $c_r = 0.8$ is assumed for the purpose of this model.

$$S_{a,r}(f) = (1 + c_r) \cdot S_{a,\phi}(f) \tag{3.16}$$

This random realisation of the (reflected) amplitude spectrum now describes the fluctuations of the water level at the gate due to wind waves. They can be transformed to the time domain with an inverse Fast Fourier transform (IFFT):

$$\eta(t) = \sum_{f=0}^{N-1} S_{a,r}(f) e^{i2\pi f t} \tag{3.17}$$

The reflected fluctuations are added to the average depth of the load event to get a full description of the water surface elevation at the gate, as plotted in 3.7.

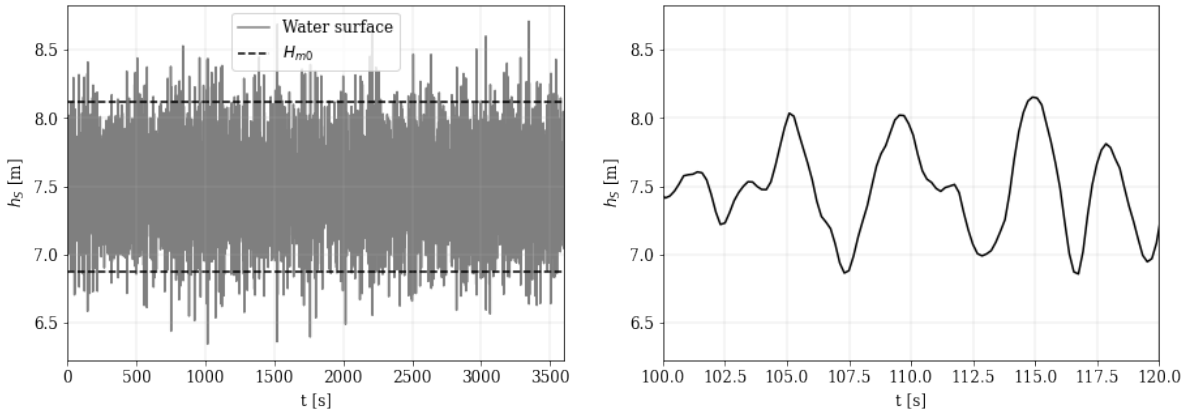

Figure 3.7: A random realisation of the surface elevation at the gate for $U_{10} = 20$m/s and $h_S = 7.5$.
Left: full record, Right: zoomed in section

The significant wave height can be found by taking the mean of the highest one-third of waves found in this time series, but can also be derived directly from the spectrum with the zeroth order moment of the variance density spectrum associated with $S_{a,r}$. The relation is $H_{m0} = 4\sqrt{m_0}$, where the n$^{\text{th}}$-order moment is calculated as follows:

$$m_n = \int_0^\infty f^n E(f) df = \int_0^\infty f^n \frac{S_{a,r}(f)^2}{2\Delta f} df \tag{3.18}$$

With that, a spectrum which describes the short-term water level fluctuations has been derived based on a set of readily available input parameters, and can be used to calculate the pressures exerted on the flood gate. A summary of the variables introduced in this chapter is given in Table 3.1:

Symbol	Description	Value	Unit
c_r	Reflection constant	0.8	-
C_{ts}	Ratio between T_p and t_s	30	-
D_S	Duration of load event	3,600	s
α	Scale parameter	See Eq. 3.5	
ω_p	Peak frequency		
γ	Peak factor		
σ	Peak-width parameter		
g	Gravity constant	9.81	m/s^2

Table 3.1: Summary of variables introduced in this chapter.

4

Gate pressures

In this chapter the wave spectra derived in Chapter 3 will be turned into pressure spectra acting on the surface of the gate. This pressure field will consist of two types of loads: the most important are the highly dynamic wave impacts that follow happen when the water surface hits the overhang from below. Quasi-static pressures are caused by fluctuations in the water level, and are called that because their low excitation frequencies generally cause a very limited dynamic response. A schematisation of the two load types is shown in 4.1. They will be calculated separately.

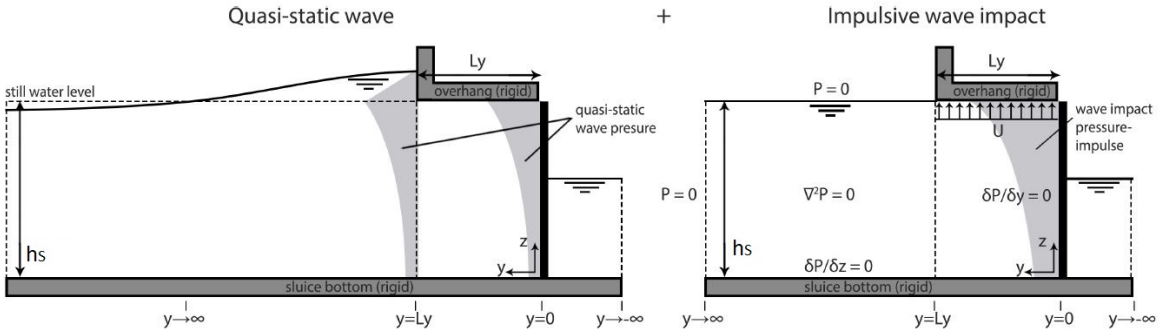

Figure 4.1: Example of the quasi-steady wave pressure (at the moment of a wave top) and the wave impact pressure impulse (at the moment of impact) acting on the gate [33]

4.1. Quasi-static pressures

Quasi-static pressures are wave pressures which fluctuate relatively slowly over time, which means that the frequency of the excitation is much smaller than the natural frequency of the gate. Rather than having a highly dynamic response the gate will therefore experience these pressures almost as if they were static. Pressure fluctuations caused by the sinusoidal movement of long waves, as described by linear wave theory, are quasi-static in this case.

4.1.1. Linear wave theory

There are competing theories about the description of wave pressures on a straight wall, some of which will be briefly introduced here. Which one is most accurate depends of the type of structure and type of waves being considered. Linear wave theory is common and holds for waves with a low steepness in intermediate to deep water. Waves with longer wavelengths relative to the depth tend to form long, shallow troughs and steeper peaks. These are described by nonlinear cnoidal or Stokes theory (See Figure 3.6) and will require for example the Sainflou method, which defines the following pressure distribution:

$$h_0 = \frac{1}{2} k H_i^2 \cdot coth(k \cdot d) \tag{4.1a}$$

$$p_1 = \rho g (H_i + h_0) \tag{4.1b}$$

$$p_0 = \frac{\rho g H_i}{cosh(k \cdot d')} \tag{4.1c}$$

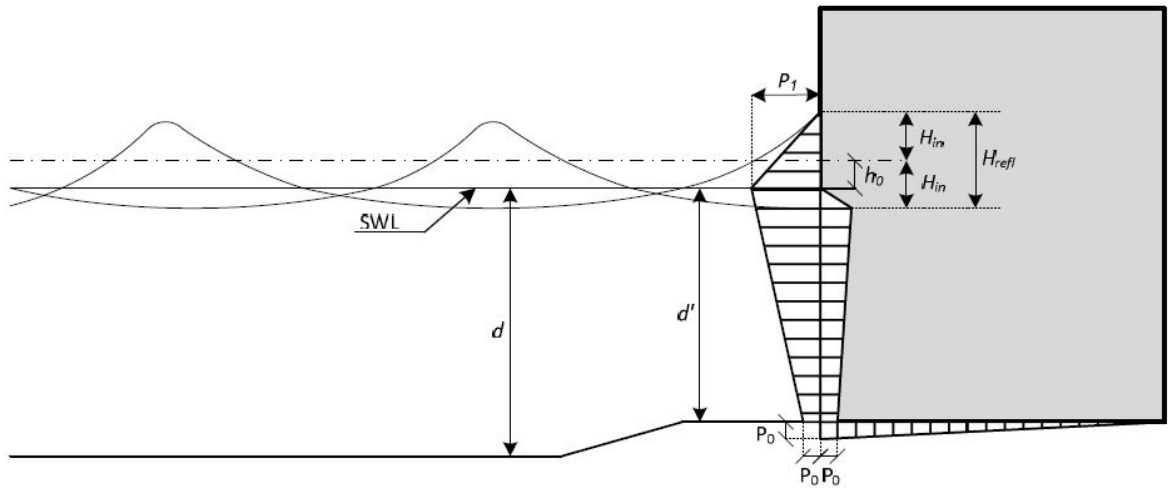

Figure 4.2: Sainflou wave pressure, [24]

Additionally, Goda's equations are often applied for the design of breakwaters because they also take wave breaking into account [24].
Because wave breaking on the structure is not taken into account, linear wave theory gives a more accurate pressure profile, and the waves were also described with linear wave theory, applying it for the quasi-static pressure field as well is the most practical. Assuming the wave pressure is uniform over the width of the gate due to the perpendicular angle of the waves, the pressure imposed by non-breaking waves against a vertical wall is as follows:

$$p_{qs}(y = 0, z, f) = \rho g S_{a,r}(f) \frac{\cosh(k(h_G - z))}{\cosh(k h_S)} \tag{4.2}$$

where k is the wave number, which can be calculated based on the frequency f and the average local water depth h_S according to Eq. 4.3. For deep and shallow water the equation can be simplified. The deep and shallow water regimes are defined based on the ratio between the wavelength $L = \frac{2\pi}{k}$ and h_S.

$$\begin{aligned} h_S > L_w/2: &\quad \omega = \sqrt{kg} && \text{(Deep water)} \\ L_w/2 > h_S > L_w/20: &\quad \omega = \sqrt{kg \cdot \tanh(kd)} && \text{(Intermediate depth)} \\ L_w/20 > h_S: &\quad \omega = k\sqrt{gd} && \text{(Shallow water)} \end{aligned} \tag{4.3}$$

The result is a pressure field $p_{qs}(z, f)$ which describes the pressure over the entire surface of the gate for every frequency of the spectrum $S_{a,r}(f)$.

4.1.2. Hydrostatic pressure

The spectrum $S_{a,r}(f)$ only describes fluctuations from the mean, which means that the hydrostatic pressure due to the average water level still has to be added. The hydrostatic pressures on both the sea- ($p_{hs,S}(x,z)$) and lake ($p_{hs,L}(x,z)$) sides of the gate are combined and will partially cancel each other out. The individual terms can't be lower than zero.

$$p_{hs}(x,z) = p_{hs,S}(x,z) - p_{hs,L}(x,z) = \rho g(h_S - z) - \rho g(h_L - z) \tag{4.4}$$

The net result is added at the zero frequency of the quasi-static pressure spectrum, which is where the average of the spectrum is stored.

$$p_{qs}(x,z,f=0) = p_{hs}(x,z) \tag{4.5}$$

The combined spectrum is transformed to the time domain with Eq. 4.6 and plotted for certain z-coordinates in Figure 4.3. It can be seen how for higher z the average hydrostatic pressure decreases while the magnitude of the fluctuations increases because the quasi-static wave impact is stronger closer to the water level. But this is only for visualisation; the response will be calculated with the pressure matrix $p_{qs}(z,f)$

$$p_{qs}(z,t) = \sum_{f=0}^{N-1} p_{qs}(z,f)e^{i2\pi ft} \tag{4.6}$$

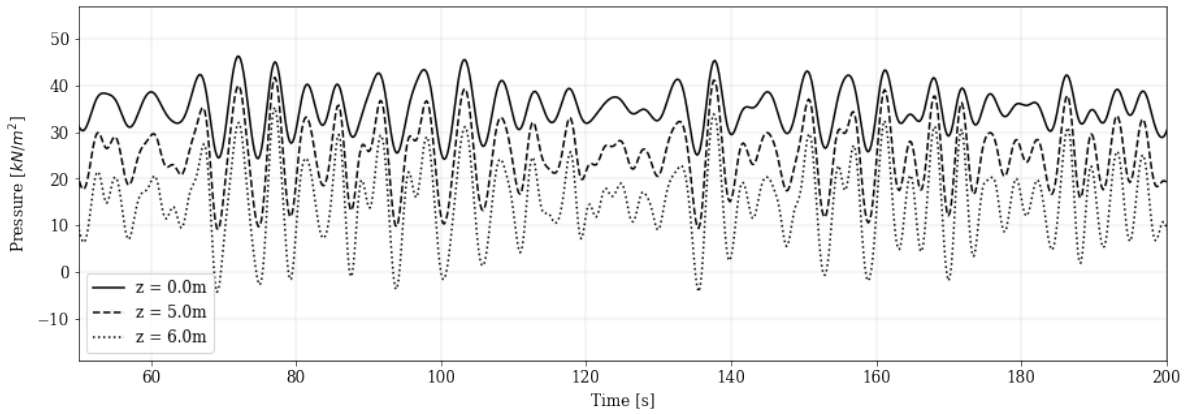

Figure 4.3: A random realisation of the quasi-static pressure on the gate.

4.2. Wave impact loads

The impulsive wave impact is much more intense than the quasi-static part, but only last a short time (order of 10-200ms [8]). Because this generally corresponds to the first resonance frequencies of the immersed gate it is more likely to cause significant gate vibrations. The overhang constrains the wave when it rises to the same level, which causes impact pressures proportional to the upward velocity of the water at that location. The forces exerted on the structure by these wave impacts are very unpredictable however, which makes basic pressure-based methods unsuitable. The pressure-impulse theory from Wood and Peregrine [37] offers a solution by instead characterising the wave impacts as impulses ($P_{im}(x,y,z)$), which are remarkably constant for similar waves. These impulses can then be converted to pressure peaks with the following equation:

$$P_{im}(x,y=0,z) = \int_{t_0}^{t_1} p_{im}(x,z,t)\,dt \tag{4.7}$$

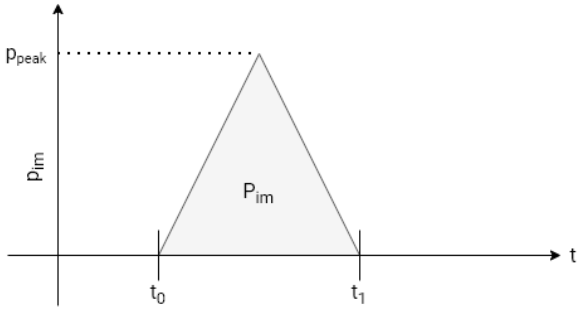

Figure 4.4: Relation between the pressure and impulse.

Because the surface area of the impulse is constant for a given wave, the magnitude of the pressures caused by different instances of the same wave depends on the shape of the impulse and the probabilistic impact duration $t_1 - t_0 = \tau$. The values and shape used in this report are based on the validation study by de Almeida and Hofland [8] for short overhangs, where it was found that a triangle best approximates the shape of wave impacts and that the probabilistic impact duration τ can be modelled by drawing it from a triangular probability distribution with a lower bound of 0.01s, an upper bound of 0.2s, and a statistical mode of 0.1s. These results follow from small-scale tests however; it is not certain how they scale to larger structures like the ones discussed in this report due to the influence of atmospheric pressure. Alternative approaches which account for this exist, for example the ones in Mitsuyasi [23] and Ramkema [28]. The sensitivity to the impact duration will be quantified in Section 8.9.
The distribution of impact pressures over the surface of the gate is derived from the following equation for the dimensionless pressure impulse:

$$\overline{P}(x, y = 0, z) = \frac{P_{im}(x, y = 0, z)}{\beta_{im}\rho_w U_w L_y} = \frac{\int_{t_0}^{t_1} p_{im}(x, z, t)dt}{\beta_{im}\rho_w U_w L_y} \tag{4.8}$$

$$\int_{t_0}^{t_1} p_{im}(x, z, t)dt = \beta_{im} U_w \cdot \overline{P}(x, y = 0, z)\rho_w L_y \tag{4.9}$$

Because the area of a triangle is also given by $A = 1/2 \cdot \text{base} \cdot \text{height}$, this further reduces to:

$$\int_{t_0}^{t_1} p_{im}(x, z, t)dt = \frac{1}{2}\tau p_{peak} \tag{4.10}$$

$$p_{peak}(x, z) = \frac{\beta_{im} U_w}{\tau} 2\overline{P}(x, y = 0, z)\rho_w L_y \tag{4.11}$$

where p_{peak} is the highest pressure of the triangular pressure profile, β_{im} is a probabilistic correction factor for the compressibility of entrapped air between the wave crest and the structure, U_w is the vertical impact velocity of the water surface, and L_y is the length of the overhang. The derivation of the semi-analytic solution of the dimensionless pressure-impulse shape $\overline{P}(x, y, z)$ can be found in de Almeida and Hofland [8]. Four examples are plotted in Figure 4.5, for different values of L_y. $\overline{P}(x, y, z,)$, ρ_w, and L_y are constant, which

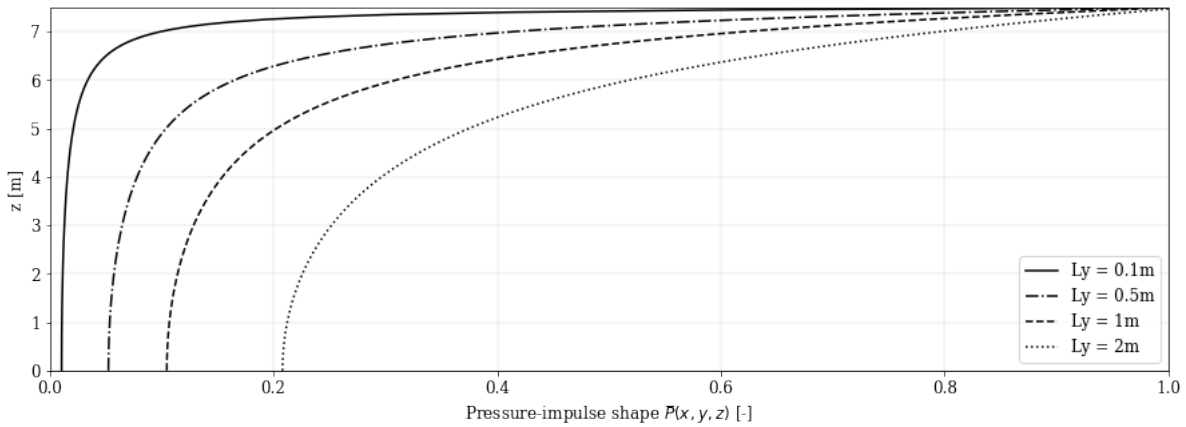

Figure 4.5: Pressure impulse shape over the gate height, for different values of L_y.

means that the pressure at the gate scales linearly with the term $\frac{\beta_{im} U_w}{\tau}$. The probabilistic correction factor β_{im} is drawn from a normal distribution with $\mu_\beta = 1.17$ and $\sigma_\beta = 0.11$ for every wave [8]. In order to find the pressures exerted by a wave impact only U_w remains undefined. Due to the assumption of a perpendicular wave approach angle the pressure will be uniform over the width, so the pressure is equal for all x.
U_w can be found by taking the local derivative of the random wave records generated in Equation 3.17 whenever it crosses the level of the overhang. But first, the time series is interpolated to a smaller time step Δt in order to accommodate the short duration of wave impact loads. A Δt of 0.0025s is sufficiently accurate to model the short wave impact durations (the shortest of which are around 0.01s). At every time step where the

water level crosses the overhang elevation from below the derivative of this interpolated time series is calculated, combined with randomly chosen values of τ and β_{im} from their respective probability distributions, and finally evaluated with Eq. 4.11 to find the peak pressure $p_{peak}(z)$.

$$U_{w,i} = \frac{\delta\eta(t_i)}{\delta t} \approx \frac{\eta(t_i) - \eta(t_{i+1})}{\Delta t} \tag{4.12}$$

where t_i is a point in time just before the water surface crosses the level of the overhang. Finally, $p_{peak}(z)$, τ, and the triangular shape can be used to turn the peak pressure into a time series:

$$p_{im,i}(z,t) = \begin{cases} 0 & t < t_i \\ \frac{p_{peak}(z)}{\tau/2}(t - t_i) & t_i < t \leq t_i + \frac{\tau}{2} \\ p_{peak}(z) - \frac{p_{peak}(z)}{\tau/2}(t - t_i - \frac{\tau}{2}) & t_i + \frac{\tau}{2} < t \leq t_i + \tau \\ 0 & t > t_i + \tau \end{cases} \tag{4.13}$$

Summing all of the separate wave impacts $p_{im,i}(t)$ that occur in a record gives the pressure time series $p_{im}(z,t) = \sum_{i=1}^{N} p_{im,i}(t)$, which looks as follows:

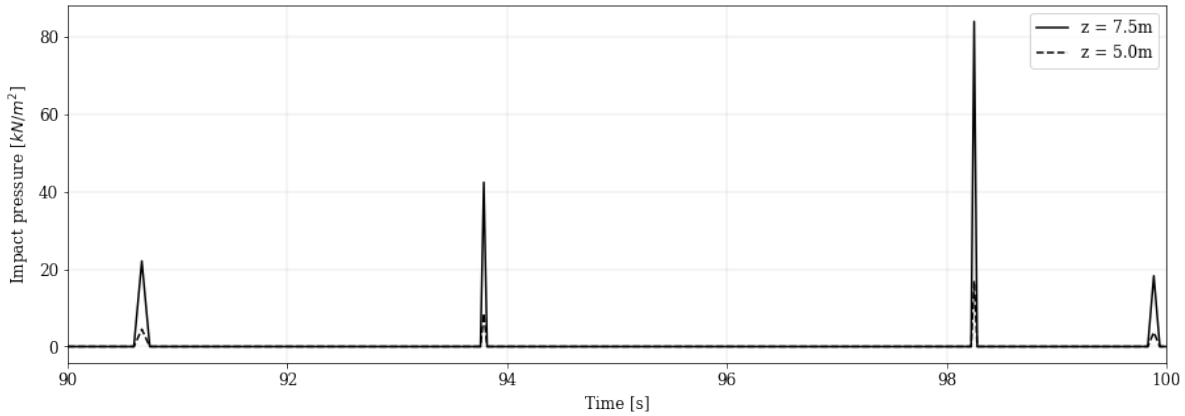

Figure 4.6: 10 second record of impact pressures on the gate surface at different z, for $U_{10} = 25m/s$, $h_S = 7.5m$, and $L_y = 1m$.

The influence of the impact duration can be observed through the lower peak pressures for waves with longer impact durations. The combined effect of the two pressure series $p_{qs}(t)$ and $p_{im}(t)$ are shown in Figure 4.7:

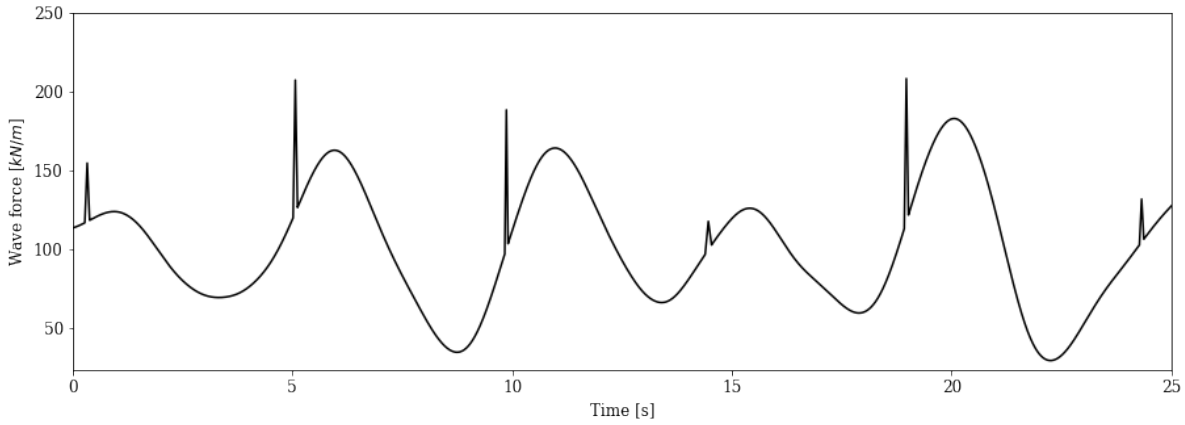

Figure 4.7: Combined effect of $p_{qs}(t)$ and $p_{im}(t)$ for $L_y = 1m$ integrated over z.

This also shows that the peak pressures increase when the slope of the water surface is steeper, as should be expected. The two-dimensional impulse pressure matrix $p_{im}(z,t)$ is transformed to the frequency domain so it can be solved in the following module:

$$p_{im}(f) = \sum_{f=0}^{N-1} p_{im}(t) e^{-i2\pi f t} \tag{4.14}$$

The two wave spectra $p_{im}(f)$ and $p_{qs}(f)$ can be evaluated separately and combined later due to the linearity of the model. The method by which these pressure fields are going to be transformed to internal gate stresses will be discussed in the next chapter.

4.2.1. Applicability of impulse method

It should be noted that this method is only validated for non-breaking waves, low steepness waves, and short overhangs relative to the wave length ($\frac{L_y}{L_w} < 0.1$). The first two conditions were already assumed to be true in Chapter 3. The latter is harder to definitively rule out. If the waves are relatively short to the overhang the entire wave won't hit it simultaneously and the pressure-impulse theory will deviate from the actual pressure field. Because the spectral method described here applies the entire wave spectrum to the structure rather than individual waves, some shorter ones will also be included. For for example $L_y = 1m$, this would limit verified applicability to waves with a wavelength longer than 10m. To check how much energy is concentrated in these short waves, some spectra are plotted on the second axis of Figure 4.8 along with the wavelength on the first. The frequency where the wavelength equals 10m has been marked:

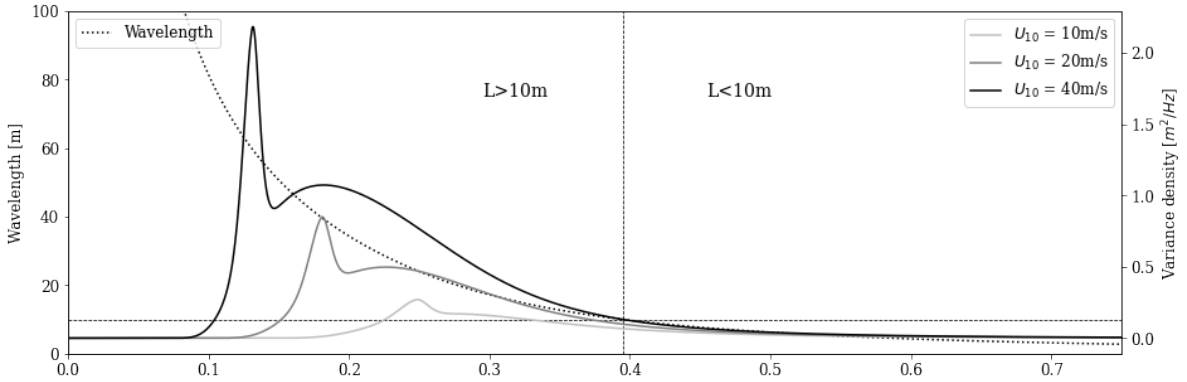

Figure 4.8: Applicability of pressure-impulse theory for $L_y = 1m$.

where the wavelength is derived from the Eq.4.3. For all wave spectra of interest the variance density of short waves is concentrated in the tail, which accounts for a small part of the total spectral energy. Because these small waves won't play a major part in when the water surface hits the overhang, it is assumed that applying pressure impulse theory to the system is justifiable in this particular case. For longer overhangs or spectra with more energy in shorter wavelengths this assumption might not prove to be valid.
Other methods, such as smoothed particle hydrodynamic modelling as discussed in Been [4], offer a more general alternative but are also numeric and more computationally demanding for the same level of accuracy in cases where the semi-analytic impulse model does apply.

Symbol	Description	Value	Unit
d_t	Time step	0.0025	s
ρ_w	Density of water	1025	kg/m^3

Table 4.1: Summary of deterministic constants introduced in preceding chapter.

Symbol	Description	Distribution	Parameters	Unit
ϕ_i	Phase shift of wave harmonic i	Uniform	$0 < \phi < 2\pi$	rad
τ	Wave impact duration	Triangular	[0.01; 0.105; 0.2]	s
β_{im}	Compressibility constant	Normal	$\mu = 1.17, \sigma = 0.11$	s

Table 4.2: Summary of probabilistic parameters introduced in preceding chapter.

5

Gate response to wave loads

In this section the previously generated pressure spectra will be imposed on the gate to compute its response. This is done based on a parametric FEM-model developed by Vorderegger [36] and Tieleman et al. [33], which describes the response of the gate in terms of its mode shapes and transfer functions. First, the simplified parametric geometry of the gate under consideration will be defined in more detail.

5.1. Parametric geometry

The shape of the gate is parametrically defined as a plate with four horizontal webs and five vertical girders to add stiffness (see Figure 5.1). Any of these parameters can be tweaked until a design is obtained which satisfies the fatigue and strength requirements formulated in the upcoming chapters. There are multiple ways to meet these requirements, which will have different dynamical effects and cost-efficiencies. A configuration with more stiffness concentrated in the flanges is more likely to mobilise higher modes, for example. Furthermore the gate is supported at the left and right sides and free to move on the bottom and at the top. This shape is much simpler than a real gate, but will serve to illustrate the process. Complex geometries can be evaluated just as well as long as they can be recreated in a finite element model.

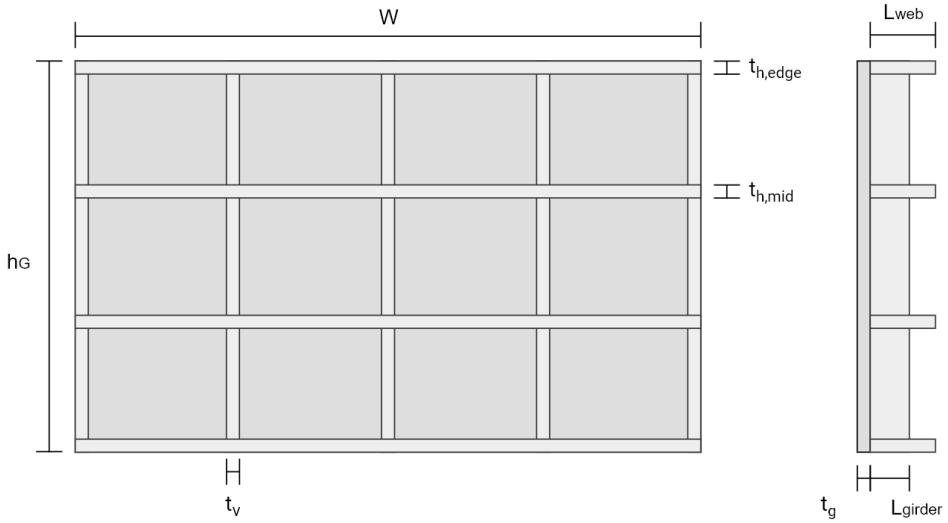

Figure 5.1: Shape of the gate and its parametrically defined elements.

5.2. Plate mechanics

The numeric model will construct the gate based on the input parameters and evaluates it as a collection of interconnected plates. This chapter will provide a short overview of the linear equations used to describe the mechanics of these plate elements.

The two plate theories which are most commonly used are classical thin plate theory (Kirchhoff [5]) and first-order shear plate theory (Mindlin [22]). Kirchhoff extends Euler-Bernoulli theory to plates, and assumes that due to the low thickness of the plate its behaviour can be described by simplifying it to its 2D midplate for small amplitude vibrations. Mindlin expands on this by also accounting for shear deformations. The response for thick isotropic plates will be derived first because it's more general.

5.2.1. Thick plates

All plates are governed by a set of kinematic, constitutive, and equilibrium equations, which describe the way the plate deforms under perpendicular loading when substituted into each other. Normal stresses perpendicular to the plane (σ_{yy}) are ignored.

$$\boldsymbol{u} = \begin{Bmatrix} w \\ \phi_x \\ \phi_z \end{Bmatrix} \qquad \boldsymbol{e} = \begin{Bmatrix} \kappa_{xx} \\ \kappa_{zz} \\ \rho_{xz} \\ \gamma_x \\ \gamma_z \end{Bmatrix} \qquad \boldsymbol{n} = \begin{Bmatrix} m_{xx} \\ m_{zz} \\ m_{xz} \\ v_x \\ v_z \end{Bmatrix} \qquad \boldsymbol{u} = \begin{Bmatrix} p \\ q_x \\ q_z \end{Bmatrix} \tag{5.1}$$

Applying a load causes the plate element to deform. These deformations can be expressed as three curvatures κ_{ii} and ρ_{ij}, and two shear deformations γ_i. They will first be related to the two orthogonal bending angles ϕ_i and a displacement w in the perpendicular y-direction (see Figure 5.2).

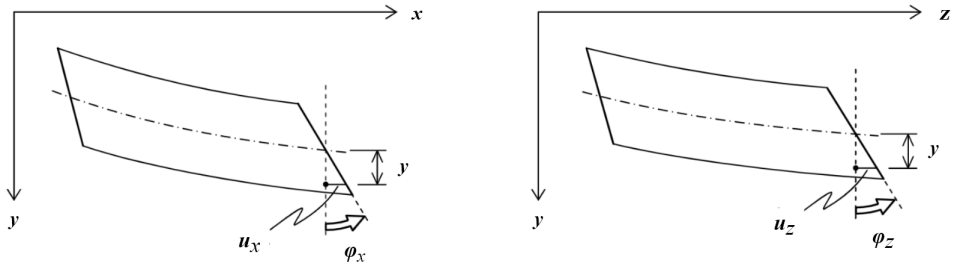

Figure 5.2: Principal deformations of a plate. [5]

The relation between the displacements and the deformations is given by the following kinematic equations:

$$\kappa_{xx} = \frac{\delta \phi_x}{\delta x} \tag{5.2}$$

$$\kappa_{zz} = \frac{\delta \phi_z}{\delta z} \tag{5.3}$$

$$\rho_{xz} = \frac{\delta \phi_x}{\delta z} + \frac{\delta \phi_z}{\delta x} \tag{5.4}$$

$$\gamma_{xy} = \phi_x + \frac{\delta w}{\delta x} \tag{5.5}$$

$$\gamma_{zy} = \phi_z + \frac{\delta w}{\delta z} \tag{5.6}$$

Because the stresses are linearly dependent on the plane-perpendicular coordinate y, they will cause bending moments over the thickness t_G:

$$m_{ij} = \int_{-t/2}^{t/2} y \cdot \sigma_{ij} dy \qquad \text{[Nm/m]} \tag{5.7}$$

Substituting the curvatures from equations 5.2-5.6 and expressing them in terms of moments gives the following equations:

$$m_{xx} = D(\kappa_{xx} + \nu\kappa_{zz}) \tag{5.8}$$
$$m_{zz} = D(\kappa_{zz} + \nu\kappa_{xx}) \tag{5.9}$$
$$m_{xz} = \frac{1}{2}D(1-\nu)\rho_{xz} \tag{5.10}$$
$$v_x = D_\gamma \gamma_{xy} \tag{5.11}$$
$$v_z = D_\gamma \gamma_{zy} \tag{5.12}$$

where ν is the Poisson's ratio of the material, which defines the lateral contraction in the direction perpendicular to the load. For most materials it is somewhere between 0 and 0.5. Steel generally has $\nu = 0.3$, and this will be the case for this project as well. E_s represents the Young's modulus for steel, which is 210,000 MPa [24]. The normal plate stiffness D and shear plate stiffness D_γ are calculated as follows:

$$D = \frac{E_s t_G^3}{12(1-v^2)} \tag{5.13}$$
$$D_\gamma = \frac{E_s t}{2\eta(1+\nu)} \tag{5.14}$$

in which η is shape factor which is equal to 6/5 for rectangles [3]. Finally, the equilibrium equations are defined:

$$\frac{\delta v_x}{\delta x} + \frac{\delta v_z}{\delta z} + p = 0 \tag{5.15}$$
$$\frac{\delta m_{xx}}{\delta x} + \frac{\delta m_{zx}}{\delta z} - v_x + q_x = 0 \tag{5.16}$$
$$\frac{\delta m_{zz}}{\delta z} + \frac{\delta m_{xz}}{\delta x} - v_z + q_z = 0 \tag{5.17}$$

where p is the pressure acting perpendicular to the plate surface. Substituting the kinematic equations into the constitutive relations, and those into the equilibrium equations gives a set of differential equations in terms of ϕ_x, ϕ_y, and w with which the response for every plate element can be found:

$$D_\gamma \frac{\delta w}{\delta x} + \left(D_\gamma - D\frac{\delta^2}{\delta x^2} - \frac{1}{2}(1-\nu)D\frac{\delta^2}{\delta z^2}\right)\phi_x - \frac{1}{2}(1+\nu)D\frac{\delta^2\phi_z}{\delta x \delta z} = q_x \tag{5.18}$$

$$D_\gamma \frac{\delta w}{\delta z} - \frac{1}{2}(1+\nu)D\frac{\delta^2\phi_x}{\delta x \delta z} + \left(D_\gamma - D\frac{\delta^2}{\delta z^2} - \frac{1}{2}(1-\nu)D\frac{\delta^2}{\delta x^2}\right)\phi_z = q_z \tag{5.19}$$

$$-D_\gamma\left(\frac{\delta^2}{\delta x^2} + \frac{\delta^2}{\delta z^2}\right)w - D_\gamma\left(\frac{\delta\phi_x}{\delta x} + \frac{\delta\phi_z}{\delta z}\right) = p \tag{5.20}$$

5.2.2. Thin plates

Thick plates, as described in the previous section, experience shear deformations through the thickness of the plate. For thin plates these can be assumed to be negligible, which means that:

$$\gamma_{xy} = \gamma_{zy} = 0 \tag{5.21}$$

Re-creating the differential equations with this change gives a partial differential equation in terms of w only:

$$D\left(\frac{\delta^4}{\delta x^4} + 2\frac{\delta^4}{\delta x^2 \delta z^2} + \frac{\delta^4}{\delta z^4}\right)w = D\nabla^2\nabla^2 w = p \tag{5.22}$$

All that remains is to impose boundary conditions and pressures, which will be different for each FEM-element. At the edges the following boundary conditions hold:

$$w(x=0,z) = w'(x=0,z) = w(x=W,z) = w'(x=W,z) = 0 \tag{5.23a}$$
$$V_{zy}(x,z=0) = M_{zz}(x,z=0) = M_{zz}(x,z=h_G) = V(x,z=h_G) = 0 \tag{5.23b}$$

Other boundary conditions can be found in basic mechanics reference books like Blaauwendraad [5]. The choice between the two methods described above depends on the properties of the structural elements. According to the SCIA Engineer manual [3] a plate is considered thin when:

$$t \leq \frac{L}{5} \tag{5.24}$$

where L is the shorter side of the rectangular element. When this holds and Kirchhoff is used, element sizes must not be smaller than the thickness of the plate. Conversely, for Mindlin it is important to refine the mesh around the edge zones (five or more elements over a width of about one thickness) to accurately render the shear stress concentrations in the edges [6]. Because the stiffeners from Figure 5.1 are going to approach the applicability limit in most cases the calculations in this report will be done according to Mindlin unless otherwise stated. This is the safer choice as long as the mesh is well constructed because it's more general than Kirchhoff.

5.3. Modal analysis

A numeric FEM-model can solve the set of plate equations defined in the previous section, but rather than evaluating every load case numerically inside the program it will only be used to obtain the in-vacuo response modes of the structure (meaning: without the influence of the water mass). For this thesis SCIA Engineer will be used to create the FEM-model, but any numeric software package which is able to take parametric inputs and perform a modal analysis will be equally suitable.

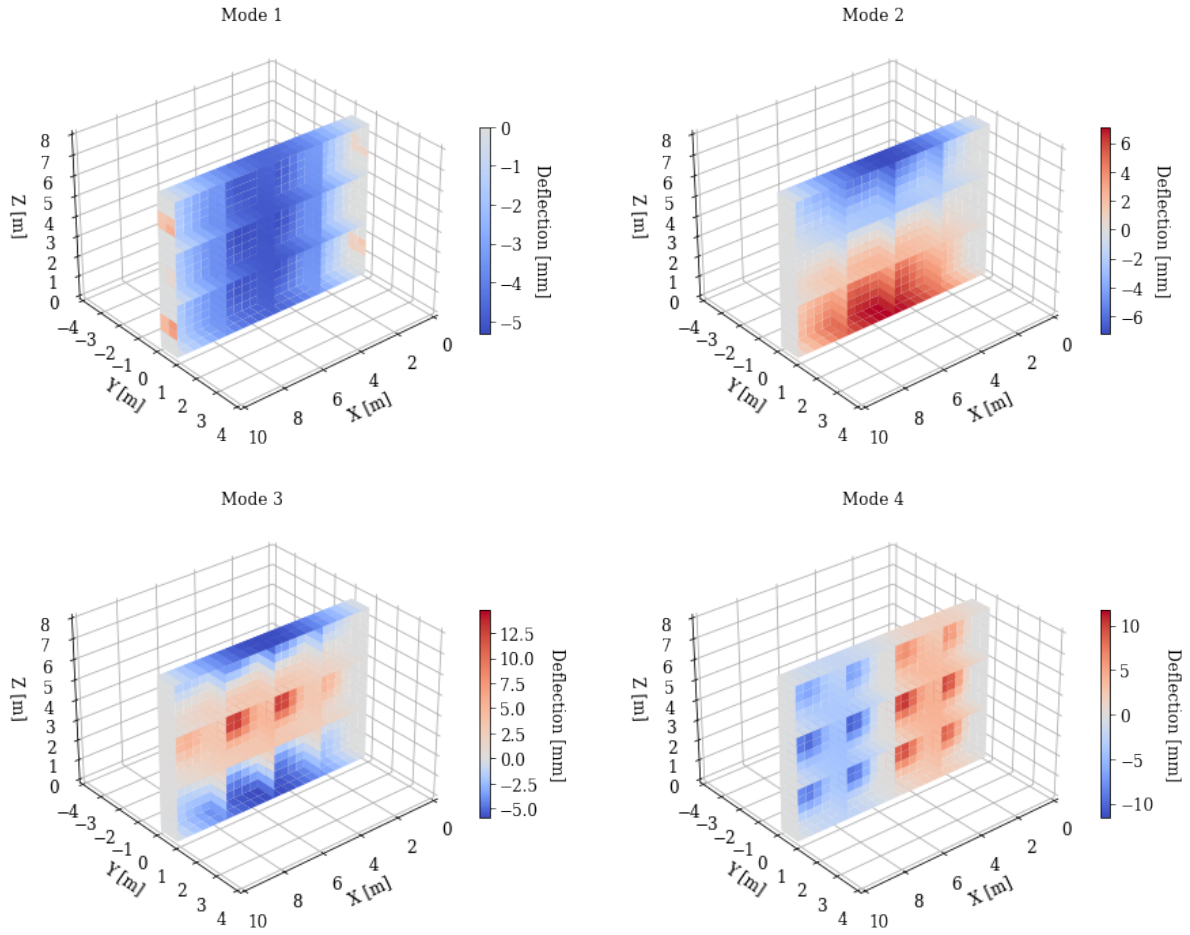

Figure 5.3: First four in-vacuo displacement modes, from SCIA

These determine how the gate would respond in a vacuum, but in order to include the effect of the water surrounding the structure the modes will be combined with the fluid potentials to obtain a full solution of the fluid-structure system. An appropriate amount of modes n_m is chosen, after which the natural frequencies

f_m and the in-vacuo response mode shapes $W_m(x,y,z)$ for the displacement and $S_{p,m}(x,y,z)$ principal stress can be exported (see Figure 5.3 for the first four displacement modes). The procedure described in the rest of this chapter applies to both the displacement and the stress, the only thing differentiating them is which in-vacuo response mode shape is applied. The total response is found by multiplying each mode with a frequency-dependent modal amplification factor and adding them together:

$$\sigma_p(x,y,z,f) = \sum_{m=1}^{n_m} A_m(f) S_{p,m}(x,y,z) \tag{5.25}$$

The stress σ_p is the principal stress, which is defined at both ends of the plate element as:

$$\sigma_p = \frac{1}{2}\left(\sigma_{xx} + \sigma_{yy}\sqrt{(\sigma_{xx}-\sigma_{yy})^2 + 4\cdot\sigma_{xy}^2}\right) \tag{5.26}$$

where σ_{ii} is the stress in direction i. The FEM model can output each of these separately, but for the purposes of this model the principal stress modes exported directly and used for the fatigue calculations. The modal amplification is influenced by the fluid-structure interaction, and will be derived with the mode-matching technique used in Tieleman et al. [33]. Based on the system properties it produces a set of Frequency Response Functions (FRF's) which give the modal coefficients $A_m(f)$ for every analysis frequency.

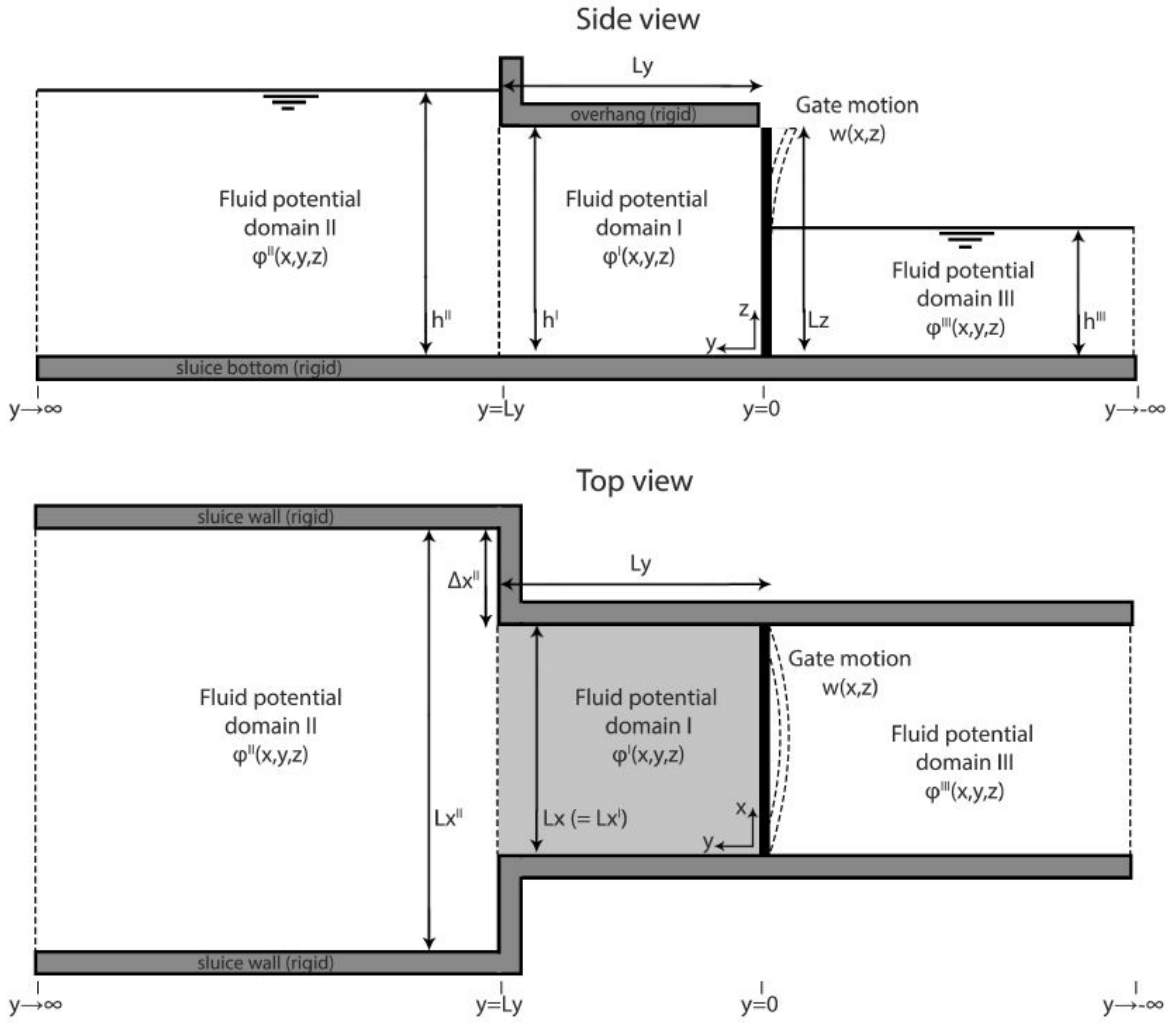

Figure 5.4: Side and top view of the model domain consisting of a flexible gate and three fluid regions, from Tieleman et al. [33]

Three separate fluid regions surrounded by impermeable boundaries are indicated in Figure 5.4, separated by the location of the gate and the edge of the overhang. In this case fluid regions I and II are located at the seaward side of the complex, and region III faces the shallower lake side. Only regions II and III have a

stress-free surface as it was shown in Tieleman et al. [32] that it can be assumed that radiating surface waves have a negligible effect. It was also found that wave impacts can be reasonably assumed to be independent excitation forces which are not altered by the response of the fluid-structure system. Another assumption made in this model is that the water level on the sea side remains constant at the level of the overhang. This is always true during impacts, but in reality it will recede along with the wave. This simplification can be made because most of the dynamic response happens in the first second or so after the impact, and damps out in a few more. This simplification therefore rests on the assumption that the most of the response happens while the water is still at the overhang level, the time after the wave fully retreats only experiences minor reverberations with a small fatigue contribution.
For the derivation of the fluid-structure interaction the gate can be simplified to a homogeneous isotropic thin plate. The equation of motion for the plate loaded by hydraulic pressures from both sides then looks as follows [32]:

$$\begin{aligned}\rho_s \frac{\delta^2 w(x,y,z,t)}{\delta t^2} + D\left(\frac{\delta^4}{\delta x^4} + 2\frac{\delta^4}{\delta x^2 \delta z^2} + \frac{\delta^4}{\delta z^4}\right)\sigma(x,y,z,t) = & p^I(x,y=0,z,t) - p^{III}(x,y=0,z,t) \\ & + \tilde{f}_e(x,y=0,z,t)\end{aligned} \tag{5.27}$$

where $\tilde{f}_e(x,y=0,z,t)$ is the wave pressure field derived in Chapter 4 and p^i refers to the fluid pressure in domain i. The fluid motion is described with the use of the velocity potential function $\phi^j(x,y,z,t)$:

$$p^j(x,y,z,t) = -\rho_f^j \frac{\delta \phi^j(x,y,z,t)}{\delta t}, \qquad j = I, II, III \tag{5.28}$$

$$\nabla \phi^j(x,y,z,t) = -\boldsymbol{v}^j(x,y,z,t) \tag{5.29}$$

After transforming the EOM to the frequency domain and performing a modal expansion on the terms, the following equation for the fluid-structure interface is found:

$$\begin{aligned}\sum_{m=1}^{\infty} \rho_s(\omega_m^2 - \omega^2) A_m(f) W_m(x,y,z) = \tilde{f}_e(x,z,f) + \rho_w i\omega \sum_{p=1}^{\infty} \left(B_p^-(f) e^{-ik_{y,p}^I L_y} + B_p^+(f)\right)\phi_p^I(x,z) \\ - \rho_w i\omega \sum_{t=1}^{\infty} D_p^+(f)\phi_t^{III}(x,z)\end{aligned} \tag{5.30}$$

in which $A_m(f)$, $B_p^+(f)$, $B_p^-(f)$, and $D_p^+(f)$ are unknown modal coefficients. A set of interface conditions will be defined in order to solve them. The infinite sums are truncated by checking the convergence of the amplitude fields by trial and error, and can be verified with the rules set out in Tsouvalas and Metrikine [34] and Tsouvalas et al. [35].
Fields I and II have dynamic and kinematic continuity at their interface because they are in direct contact. At the outer edges of regions II and III the radiation conditions holds ($|y| \to \infty$).

$$\frac{\delta \phi^j(x,y=0,z,t)}{\delta y} = -\frac{\delta w(x,z,t)}{\delta t} \tag{5.31a}$$

$$-\rho_f^I \frac{\delta \phi^I(x,y,z,t)}{\delta t}\bigg|_{y=L_y} = -\rho_f^I \frac{\delta \phi^I I(x,y,z,t)}{\delta t}\bigg|_{y=L_y} \tag{5.31b}$$

$$\frac{\delta \phi^I(x,y,z,t)}{\delta y}\bigg|_{y=L_y} = \frac{\delta \phi^I I(x,y,z,t)}{\delta y}\bigg|_{y=L_y} \tag{5.31c}$$

Finally, the gate, bottom, and walls impose a zero velocity boundary condition on their associated boundaries. For the overhang this is also the case if the surface level elevation is as at least as high as the overhang.

$$\left.\frac{\delta\phi^j(x,y,z,t)}{\delta x}\right|_{x=0} = \left.\frac{\delta\phi^j(x,y,z,t)}{\delta x}\right|_{x=L_x^j} = 0 \qquad (for\ \ j=I,III) \tag{5.32a}$$

$$\left.\frac{\delta\phi^{II}(x,y,z,t)}{\delta x}\right|_{x=-\Delta x^{II}} = \left.\frac{\delta\phi^{II}(x,y,z,t)}{\delta x}\right|_{x=L_x^{II}-\Delta x^{II}} = 0 \tag{5.32b}$$

$$\left.\frac{\delta\phi^{I}(x,y,z,t)}{\delta z}\right|_{z=0} = \left.\frac{\delta\phi^{I}(x,y,z,t)}{\delta z}\right|_{z=h^I} = 0 \tag{5.32c}$$

$$\left.\frac{\delta\phi^{j}(x,y,z,t)}{\delta z}\right|_{z=0} = \rho_f^j \left.\frac{\delta\phi^{j}(x,y,z,t)}{\delta t}\right|_{x=h^j} = 0 \qquad (for\ \ j=II,III) \tag{5.32d}$$

The system of equations 5.27-5.32 can now be solved by using the orthogonality of the modes. The full derivation and solution can be found in Tieleman et al. [33]. For the response of the gate only the modal coordinate $A_m(f)$ is of interest, which has now been defined in terms of the external pressure $\tilde{f}_e(x,z,f)$. Because the forcing is a variable input the modal coordinate $A_m(f)$ will instead be defined as the multiplication of a frequency response function $FRF_m(f)$ and the forcing. The full solution can therefore be obtained with the following equation:

$$\sigma_E(x,y,z,f) = \sum_{m=1}^{n_m} A_m(f) W_m(x,y,z) = \sum_{m=1}^{n_m} FRF_m(f) S_{E,m}(x,y,z) \tilde{f}_e(x,z,f) \tag{5.33}$$

The solution is truncated to a number of modes and a frequency range which captures most of the response. The proper truncation limit can vary based on the properties of the system; if higher modes or frequencies contribute significantly to the response the frequency range should be extended to include them.

5.4. Damping

The damping of the system determines how quickly the response to the excitation damps out. The total damping of the system consists of several components, the most important of which is the structural damping of the steel itself. The water mass on either side of the gate can also dissipate vibrations by radiating surface waves or due to the compressibility of water. At the supports there can be local damping as well, in the form of either dedicated dampers installed for that purpose or an elastic material like rubber used for the seal. The latter will not be considered here.

For hydrodynamic action on a welded steel structure a material damping factor ζ of 2-3% is advised for extreme loads and 1-2% for lighter fatigue loads [15]. This means ζ% of the critical damping ratio $2\sqrt{km}$ is mobilised (where m is the total mass of the system). 2% will be used for the remainder of this report. Depending on the water depth and natural frequency of the structure, the added damping due to wave radiation is negligible if the following condition holds [17]:

$$\frac{\omega^2 h}{g} > 10 \tag{5.34}$$

Which for an in-vacuo natural frequency (obtained from SCIA) somewhere between 5Hz and 25Hz gives the following results:

$$\frac{5^2 \cdot 7.5}{9.81} \leq \frac{\omega^2 h}{g} \leq \frac{25^2 \cdot 7.5}{9.81} \tag{5.35}$$

$$19 \leq \frac{\omega^2 h}{g} \leq 478 \tag{5.36}$$

The condition is therefore true for all expected gate designs. Furthermore this type of damping requires a free surface, whereas during wave impacts the water level is constrained by the overhang. Ignoring this additional source of damping is the conservative choice as well. For this same reason the FSI-model assumes a stress-free boundary condition based on conclusions from Tieleman [31]. This only leaves the 2% structural damping, which will therefore be used for the remainder of this report. This topic is worth researching further however, as the damping experienced by the added water mass and air pockets under the overhang will likely amount to more than just radiation damping.

In a more detailed analysis the damping could also be made frequency-dependent, though for steel constructions it's generally valid and conservative to use a constant value instead.

5.5. Response calculation

Because the model is numeric, the frequency response function $FRF_m(f)$ of the FSI will be calculated for a certain amount of sections. The load on each of these sections is therefore assumed to be uniform. The representative load on each of these sections is obtained by integrating the pressure matrix over the x-, and z-coordinates corresponding to each section, which ensures that the overall pressure remains constant.

$$q_{ij}(f) = \int_{z_j}^{z_{j+1}} \int_{x_i}^{x_{i+1}} \tilde{f}_e(x,z,f)\, dx dz \tag{5.37}$$

The iterator i iterates over n_x width sections and j over n_z height sections. The FRF associated with each of these ij-pairs will be reffered to as $FRF_{ijm}(f)$. An example of the discretized pressure is plotted in Figure 5.5:

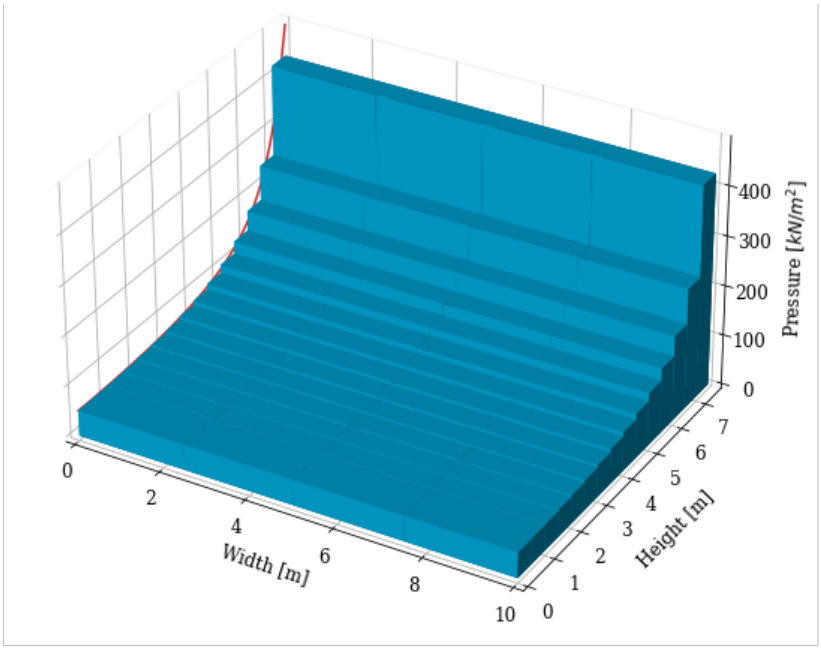

Figure 5.5: Example of discretized pressures for $n_x = 4$ and $n_z = 15$.

The FRF's obtained from the FSI-model are interpolated to the spectral resolution of the load spectra to enable proper multiplication. As an example the functions $FRF_{ijm}(f)$ for $i = 0$, $j = 7$, and $m = 1,2..9$ are plotted in Figure 5.6.

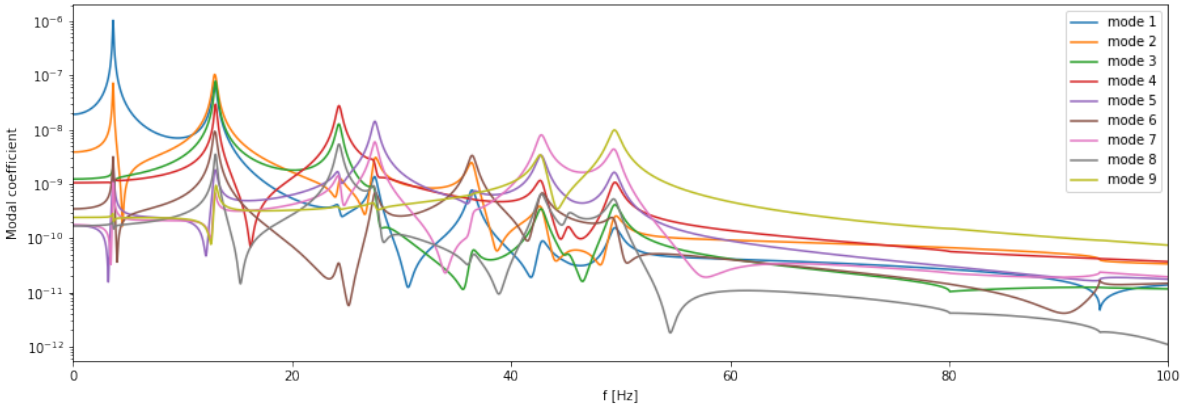

Figure 5.6: Example frequency response functions for the section $i = 0$, $j = 7$

With the discretized load spectra $q_{ij}(f)$, frequency response functions $FRF_{ijm}(f)$, and mode shape $S_{E,m}(x,y,z)$ the response spectrum $R_m(f,x,z)$ can be determined for every gate coordinate and mode by slightly modifying Equation 5.33:

$$R_m(f,x,z) = S_{E,m}(x,z) \sum_{i=1}^{n_x} \sum_{j=1}^{n_z} q_{ij}(f) \cdot FRF_{ijm}(f) \tag{5.38}$$

If the critical element has been identified, this matrix multiplication can be made more efficient by only multiplying with the modal shapes $S_{E,m}(x_c, z_c)$ rather than doing so for every coordinate. This saves a lot of computation time if a lot of simulations have to be run. In either case, summing all the modal contributions finally gives the total response:

$$R(f,x,z) = \sum_{m=1}^{n_m} R_m(f,x,z) \tag{5.39}$$

These steps are implemented for both the quasi-static and impact spectra, which were derived separately in Chapter 7. Because the resolution required to accurately represent the quasi-static spectrum is lower than the one for the impact loads, it can be computed faster. By only combining the two at the very end the total quasi-static response only has to be interpolated to the wave impact resolution once, whereas in earlier stages of the model it would have to be done at every gate surface coordinate. Because the model is linear the responses to both of these load spectra can be added afterwards:

$$R_t(f,x,z) = R_{imp}(f,x,z) + R_{qs}(f,x,z) \tag{5.40}$$

Performing an inverse Fourier transform allows the response to be plotted in the time domain as well.

$$\sigma_E(t,x,z) = \sum_{f=0}^{N-1} R_t(f,x,z) e^{i2\pi f t} \tag{5.41}$$

A 50-second section of the total response for a specific coordinate is plotted along with the force in Figure 5.7, to illustrate the effect of the loads on the gate response.

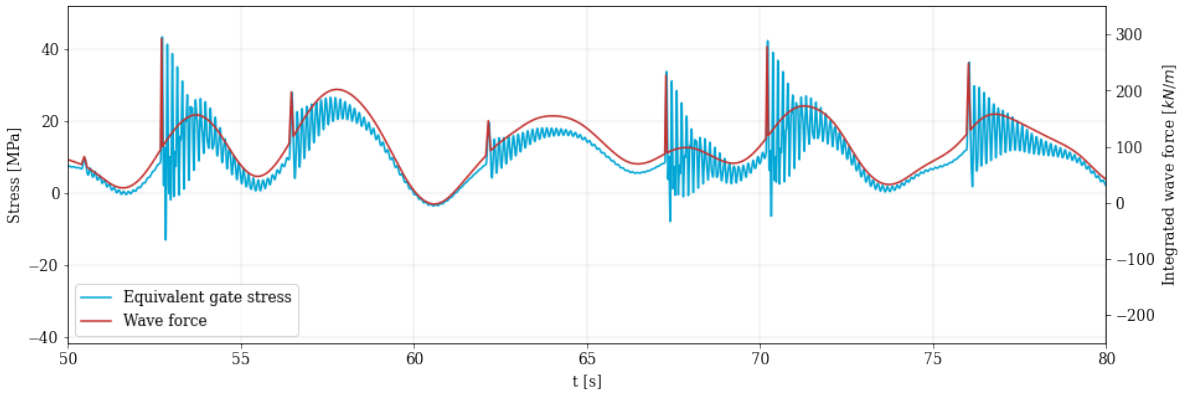

Figure 5.7: Example of impact loads and resulting gate reflection at (x=5;y=0;z=7.5) over time

The impulses cause a large initial spike which then damps out over time. The effect of quasi-static loading, with its lower amplitude and longer period, can also be distinguished but doesn't cause a strong dynamic response. The stress can also be plotted for every gate coordinate at once, such as in Figure 5.8. The colour of the plate sections indicates the average stress of the four mesh points bordering it.
This shows where stresses are concentrated and which structural elements are therefore likely to need the most reinforcement. Because the solution is calculated for each mode individually, it's also possible to graph the contribution of specific modes to the load at certain positions. The contribution of the six most important modes relative to the total stress response of the first 16 modes is plotted in Figure 5.9. The implications of this will be further discussed in the case study.

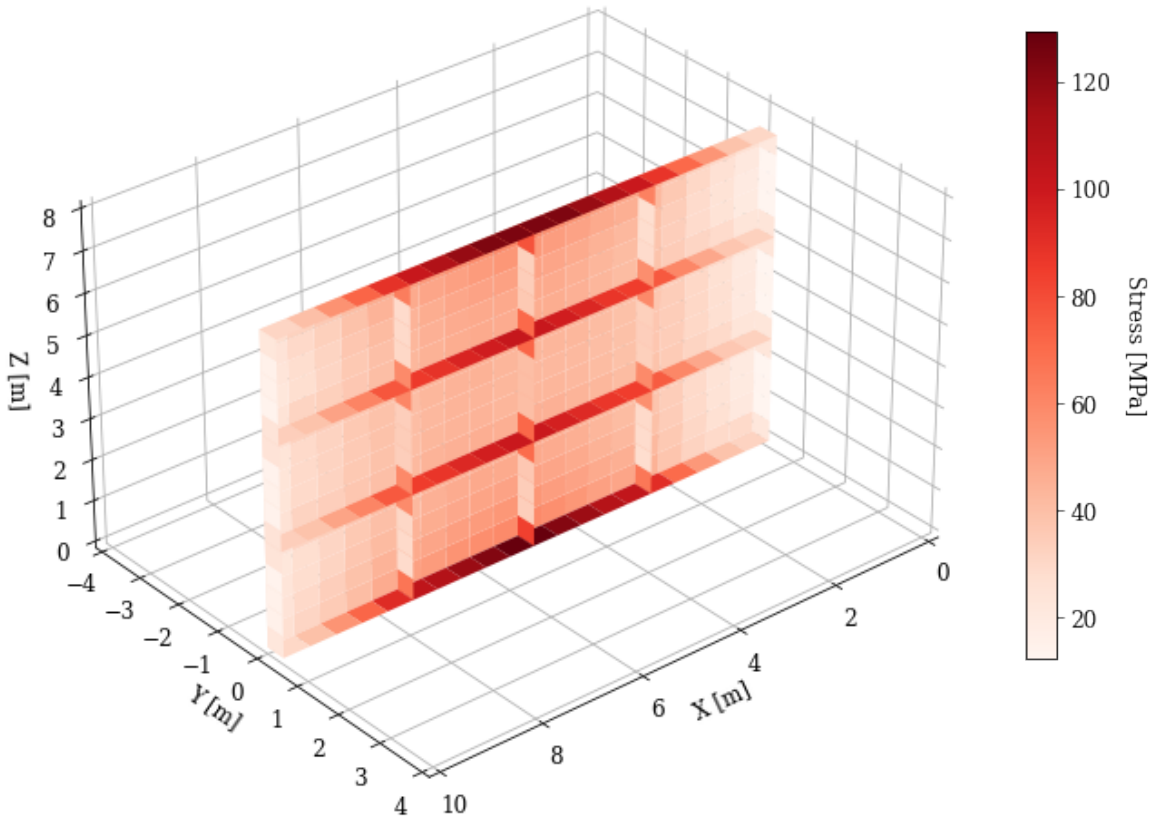

Figure 5.8: Maximum stress at every coordinate of an example of a gate for U_{10} = 50m/s, h_S = 7.5m, and a mesh size of 0.5m

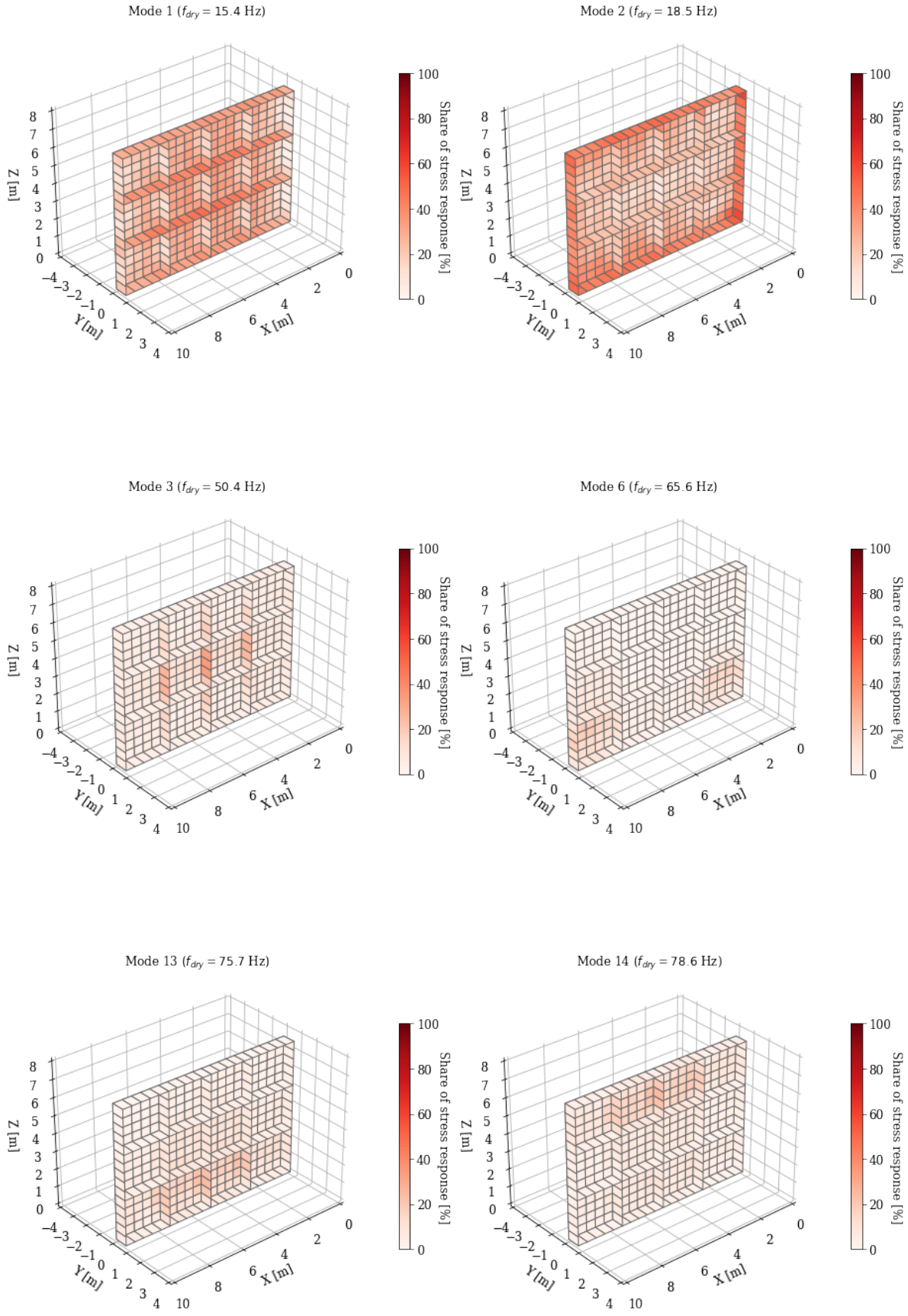

Figure 5.9: Relative contribution of the six most important modes to the total response at all gate coordinates

6

Fatigue

In the previous module the response spectrum $\sigma_E(f,x,z)$ was derived. In this chapter, the fatigue damage caused by this stress history is quantified. There is a wide variety of theories available to evaluate the fatigue caused by a given response spectrum. They can generally be subdivided into time- and frequency domain methods. Which is best for a particular application depends on which theory best matches the the applicability, accuracy, and efficiency demands of the problem, but for the purposes of this report only the most common theory from both categories will be presented and compared. These are the Palmgren-Miner method combined with Rainflow counting as defined in the Eurocode for the time domain, and the semi-empirical Dirlik method for the frequency domain.

6.1. Time domain

The Palmgren-Miner method is the most common and prescribed by the Eurocode EN 1993-1-9 [10]. It takes a stress time series $\sigma_E(t,x,z)$ as input, and calculates a fatigue damage factor D which shows how much of the fatigue capacity of the element is used by that load event. If the fatigue damage factor D exceeds 1 the material has failed. Because fatigue is caused by the cyclic loading and unloading of a material, the first step is to index which load- and unload cycles (also referred to as stress ranges) occur, as well as how often. Because the response amplitude is a superposition of a broad spectrum of harmonics, the peaks can't directly be counted like in cases where the load consists of just a single cyclic load.
The Rainflow counting algorithm developed in Matsuishi and Endo [20] offers a solution here, as it is able to reduce a broad spectrum of stresses into an equivalent set of simple stress reversals.

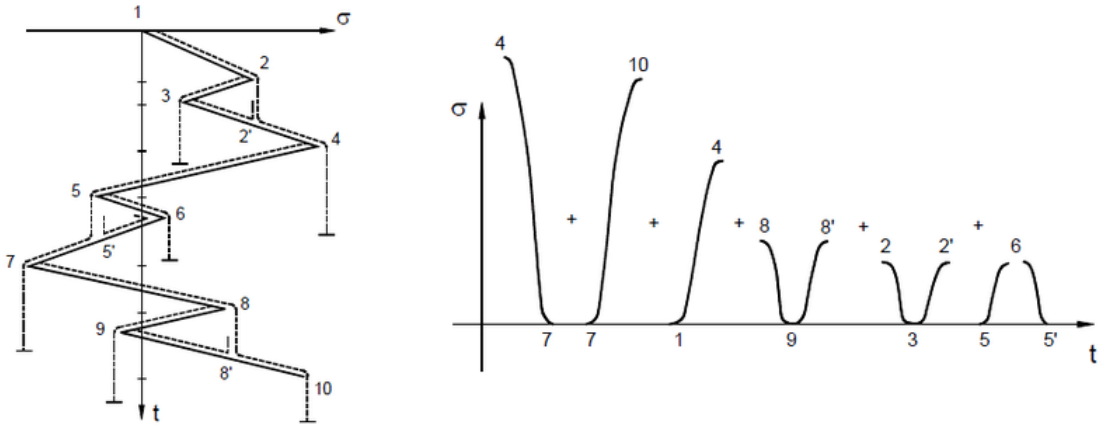

Figure 6.1: Rainflow algorithm (Ribeiro et al., 2012)

It identifies all the turning points in a time series (such as in Figure 6.1) and takes out the smallest intermediate reversals which cancel each other out (for example 2-3-2' and 5-6-5'). It then removes these pairs of points, and re-evaluates the sequence until no more pairs can be found. The resulting list of (approx. 10.000-

20.000) stress reversals can then be used to determine the fatigue.
To find how much cumulative damage these stress cycles do, Miners rule can be used. It states that the cumulative damage D can be found by adding all the ratios of the amount of stress cycles (n_i) and how many of those cycles the material can withstand ($N_{c,i}$):

$$D = \sum_{i=1}^{k} \frac{n_i}{N_{c,i}} \tag{6.1}$$

The resistance $N_{c,i}$ of the material is determined by its S-N curve, which relates any given stress S to the maximum amount of load cycles (N_c) the material can withstand. The definition of the curve varies for different material properties and detail categories ($\Delta\sigma_c$). The detail category reflects the fatigue resistance of a certain gate element, and is defined as the stress capacity at 2 million cycles. Rules for when to apply which category are given in the Eurocode [10].

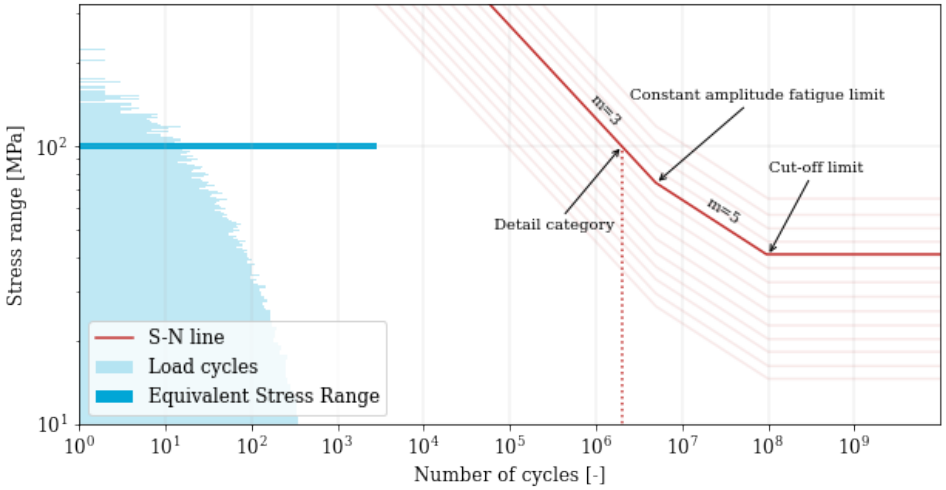

Figure 6.2: Plot of random stress history with S-N curve

The amount of cycles Nr the material can withstand at a certain stress cycle $\Delta\sigma_R$ is derived with Equation 6.2 from the Eurocodefor Standardisation [10]:

$$\begin{aligned}
\gamma_{Ff}\Delta\sigma_R^m N_R &= \frac{\Delta\sigma_C^m}{\gamma_{Mf}} 2\cdot 10^6 \\
\gamma_{Ff}\Delta\sigma_R^m N_R &= \frac{\Delta\sigma_D^m}{\gamma_{Mf}} 5\cdot 10^6 \qquad \text{with } m=3 \text{ for } N \le 5\cdot 10^6 \\
\gamma_{Ff}\Delta\sigma_R^m N_R &= \frac{\Delta\sigma_D^m}{\gamma_{Mf}} 5\cdot 10^6 \qquad \text{with } m=5 \text{ for } 5\cdot 10^6 \le N \le 10^8
\end{aligned} \tag{6.2}$$

Where $\Delta\sigma_D = 0.737\Delta\sigma_C$ is the constant amplitude fatigue limit, below which the slope m of the S-N curve flattens. At $\Delta\sigma_L = 0.549\Delta\sigma_D$ the cut-off limit is reached. Stress cycles below this level will not cause any fatigue damage to the material. γ_{Mf} and γ_{Ff} are safety factors for the material and loading respectively, and are defined for different situations in the Eurocode. A graph of the S-N curve for $\Delta\sigma_C = 100$ is plotted in Figure 6.2 along with a random load spectrum. The stress ranges can be combined into an equivalent stress range $\Delta\sigma_{eq}$:

$$\Delta\sigma_{eq} = \left(\frac{\sum n_i \Delta\sigma_i^3 + \sum n_j \Delta\sigma_j^3 \left(\frac{\Delta\sigma_j}{\Delta\sigma_D}\right)^2}{n_i + n_j} \right)^{1/3} \tag{6.3}$$

where the stress ranges $\Delta\sigma_i$ are below the constant amplitude fatigue limit $\Delta\sigma_D$, and $\Delta\sigma_j$ above it. The fatigue damage factor is then found with:

$$D = \frac{\gamma_{Ff} \Delta\sigma_{eq}}{\Delta\sigma_D \gamma_{Mf}} \tag{6.4}$$

This result is more intuitive, and has also been plotted in Figure 6.2.

6.2. Frequency domain

In offshore and mechanical engineering, where spectral loads are common, the semi-empirical method proposed by Dirlik [9] is often applied. It has been shown to be the most robust for Gaussian broad-band spectra by Mršnik et al. [25]. It creates a stress-cycle probability distribution $p(S)$ from the response spectrum $\sigma(f,x,z)$, which can then be used to estimate the fatigue damage. The probabilistic distribution of the stress ranges is derived with the following equations:

$$p(S) = \frac{1}{2\sqrt{m_0}} \left[\frac{D_1}{Q} e^{\frac{-Z}{Q}} + \frac{D_2 Z}{R^2} \cdot e^{-\frac{Z^2}{2R^2}} + D_3 \cdot Z \cdot e^{-\frac{Z^2}{2}} \right] \tag{6.5}$$

$$D_1 = \frac{2(x_m - \gamma^2)}{1+\gamma^2}, \qquad D_2 = \frac{1-\gamma-D_1+D_1^2}{1-R}, \qquad D_3 = 1 - D_1 - D_2, \qquad Z = \frac{S}{2\sqrt{m_0}}$$

$$Q = \frac{1.25(\gamma - D_3 - D_2 \cdot R)}{D_1}, \qquad R = \frac{\gamma - x_m - D_1^2}{1-\gamma-D_1+D_1^2}, \qquad \gamma = \frac{m_2}{\sqrt{m_0 \cdot m_4}}, \qquad x_m = \frac{m_1}{m_0}\sqrt{\frac{m_2}{m_4}}$$

where Z is the normalised amplitude, x_m is the mean frequency, and the parameter γ is a measure of the spectral width. The other values are intermediate results. The spectral moments m_n were defined in Equation 3.18. Equation 6.5 generates a probability density spectrum for the stress range S by fitting multiple distributions together and scaling them based on the constants. From this probability distribution the expected amount of damage can be derived by multiplying it with the expected amount of waves during the load event duration D_S:

$$n_S = x_m D_S \cdot p(S) \tag{6.7}$$

From here, Equations 6.3 and 6.4 can be applied to find the fatigue damage associated with the load event. This spectral method tends to be more conservative than the more exact time domain method [25], but is much more computationally efficient. To compare the fatigue outcomes of both methods, 250 simulations were run for different wave states. The result is plotted in Figure 6.3:

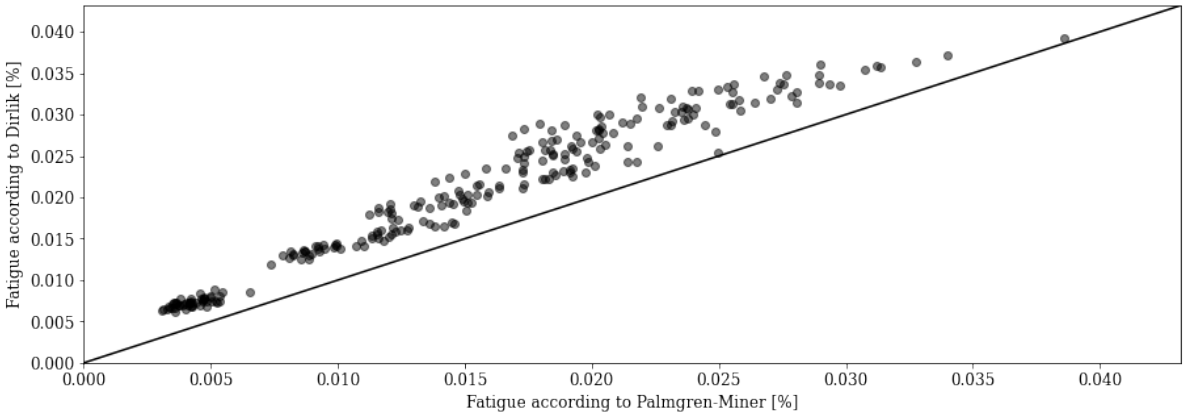

Figure 6.3: Comparison of Dirlik and Palmgren-Miner methods.

As expected the results for the Dirlik method are more conservative than the time-domain results obtained with the Palmgren-Miner method. The Palmgren-Miner method (incl. the Fourier transform) takes on average 1.70s to evaluate a load event of one hour whereas the Dirlik method only needs 0.5s per hour; more than thrice as efficient. However because time efficiency is not a major issue for the model in its current state, the more accurate result is prioritised over the faster but more conservative one.

6.2.1. Alternatives

The broadbandedness of a spectrum indicates whether it consists of a wide range of frequencies (broad) or just a few (narrow). There exists no hard cut-off where a process becomes either narrow- or broad-banded, but the Vanmarcke parameter is often used as a measure of broad-bandedness [38]. It ranges from 0 to 1, where 0 is an infinitesimally small bandwidth:

$$\delta = \sqrt{1-\gamma^2} \tag{6.8}$$

It approaches zero as the frequency range of a process gets infinitely small. $\delta < 0.1$ is generally used as a rule of thumb for a process to be considered narrow-banded. For the wave spectra used in this project the parameter lies between 0.95 and 0.97, which supports the assumption that the load spectrum is broad-banded.
However processes can also be multi-modal, meaning there are multiple distinct spectral peaks due to resonance at the natural frequencies (See Figure 6.4). For those cases Zheng et al. [38] has developed a bi- and tri-modal method, which give more accurate results than Dirliks method if the response is non-Gaussian.

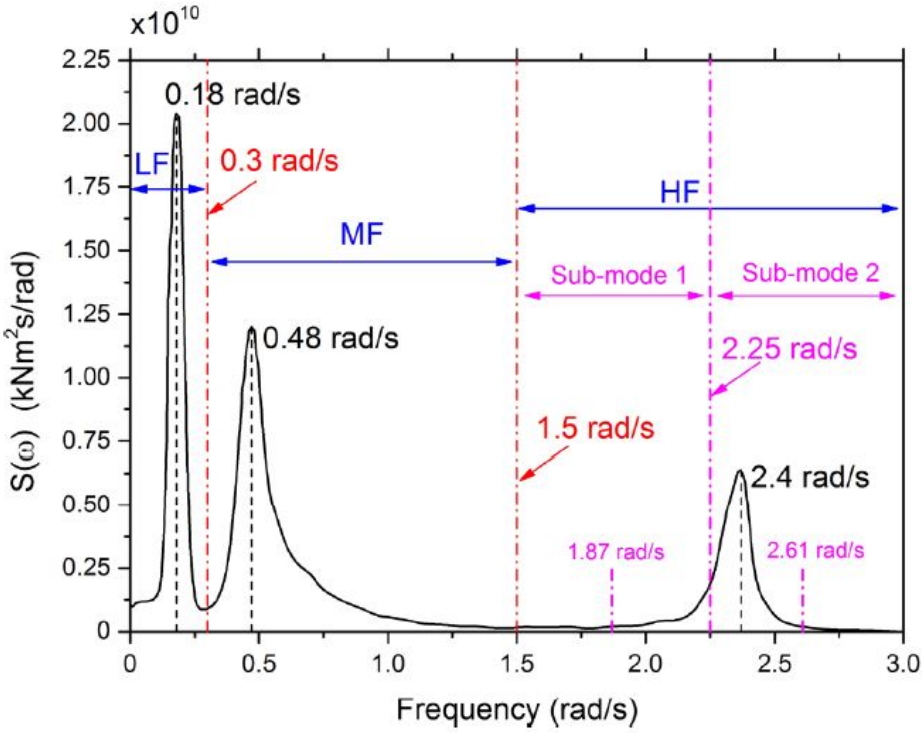

Figure 6.4: Example of a trimodal response spectrum and its separate low (LF), medium (MF), and high (HF) processes. [38]

Looking at some random examples of response power density spectra generated by the loads described in previous chapters confirms that this is the case here as well:
If it is therefore necessary to increase the efficiency of the model by using a frequency domain method, it's recommended to apply the model described in Zheng et al. [38] to account for the trimodal shape. Though even then, a phase-resolving time domain method will always be more accurate.

6.3. Multi-axial and local stresses

So far the validity of the principal stress as defined in Equation 5.26 has been assumed, but this is not always the case. For fatigue in the main construction elements (skin plate, stiffeners) this assumption is allowed depending on the detail category, but for welds the load has to be defined in terms of individual stress components (σ_{xx}, σ_{zz}, and τ). Their combined effect on the fatigue damage is then given by the following interaction formula [10]:

$$D = \left(\frac{\gamma_{Ff}\Delta\sigma_{E2}}{\sigma_C/\gamma_{Mf}}\right)^3 + \left(\frac{\gamma_{Ff}\Delta\tau_{E2}}{\tau_C/\gamma_{Mf}}\right)^5 \tag{6.9}$$

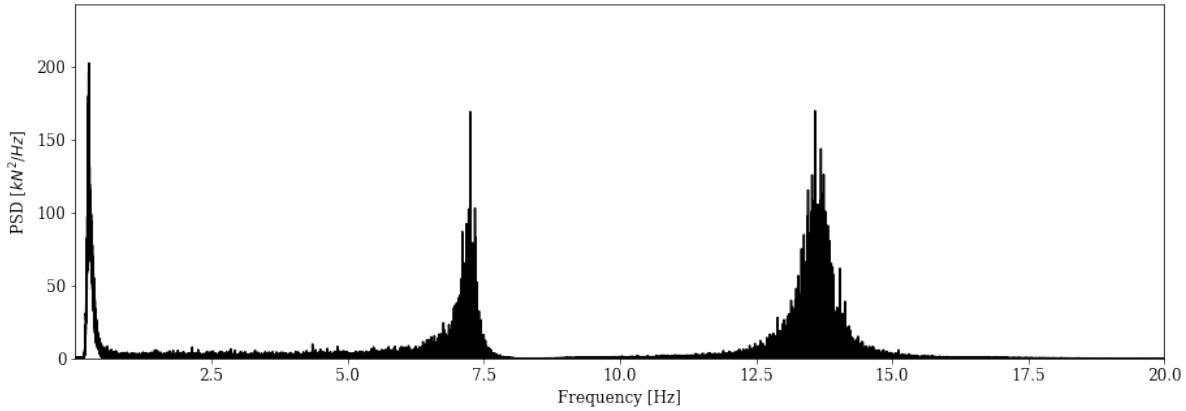

Figure 6.5: Example of a generated power density spectrum of the stress at the top of the gate exhibiting trimodal behaviour.

where the subscript E2 indicates the equivalent stress range at two million cycles. More details can be found in the Eurocode. In order to do this the FEM model from Section 5.3 has to output all the relevant stress components individually rather than as the combined principal stress. The force pulling on one of the flanges is then found by integrating all the stresses along it, and felt in the welds as shown in Figure 6.6:

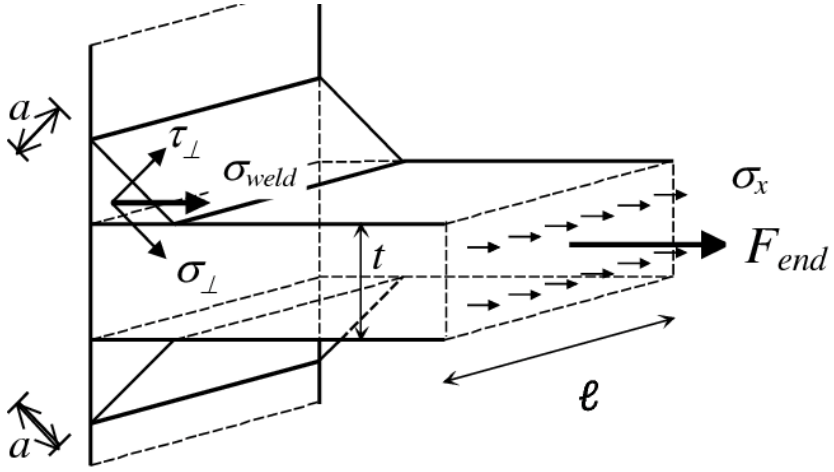

Figure 6.6: Forces in a fillet weld [10]

Which gives the following stresses:

$$\sigma_E = \tau_E = \frac{F_{end}\sqrt{2}}{4al_{eff}} \tag{6.10}$$

where l_{eff} is the effective length of the weld. A higher resolution is also required to model local stress concentrations in the corners and connections. If rendering the entire FEM model with a sufficiently high resolution becomes computationally prohibitive the detail in question can either be rendered with a locally increased resolution, or with the coarse grid supplemented with a local model. This local model (or 'submodel') takes the output of the coarse model as boundary conditions, and then evaluates the local effects in greater detail.

6.4. Fatigue sensitivity and variance

The modules described in Chapters 3 through 6 together describe how a sea state defined by its wind velocity U_{10} and the average sea water level h_S can be transformed to a fatigue assessment. Because the model introduces a number of probabilistic elements, such as the random phases and wave impact durations, the final fatigue outcome will also have a degree of variance. Even though it will mostly average out over thousands of simulations, the combined effect and sensitivity of the two parameters will be quantified in this section because it will help with some boundary condition modelling choices later.

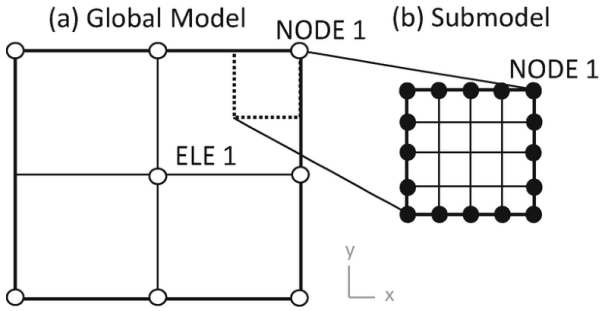

Figure 6.7: Example of a coarse global model and a finer local model from Sracic and Elke [30]

The variance is found by running the same simulation multiple times and assessing the spread of the results. This was done for a series of different load combinations to illustrate how the variance changes depending on the input. Every load combination plotted in Figure 6.8 was computed 20 times. The black error bars indicate the standard deviation of the outcomes.

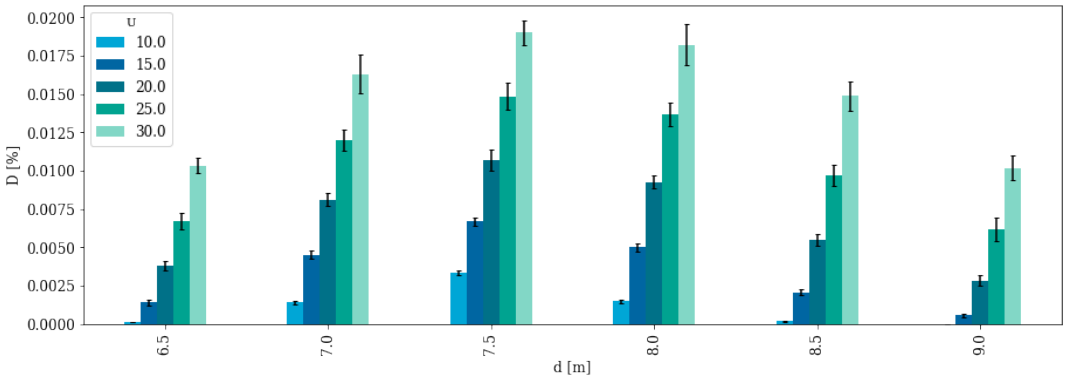

Figure 6.8: Fatigue results for different load combinations when the overhang is at 7.5m.

The results show that the fatigue scales roughly linearly with the wind velocity, and that the dependence on the average water level follows a curve which peaks at the height of the overhang. The most consequential load scenarios are therefore the ones with the highest wind velocity and an average water level equal to the height over the overhang. The variance increases sharply for extreme water levels and low wind velocities because fewer waves end up hitting the overhang, making the random nature of the wave spectrum more pronounced. Most load cases have a standard error of 5-10%, but some low-impact events can reach 20%.

7

Probabilistic load cases

In the previous chapters a method has been presented which can evaluate the fatigue damage caused by a single load event. Generally such a method would be used to evaluate a limited number of design load cases, but the high efficiency of the simulation steps defined here allows for a much more comprehensive approach. This chapter will present a way to probabilistically define a set of inputs representing the entire lifetime of the structure based on historical data.

7.1. Input definition

The water level is affected by short-term processes, such as wind- and swell waves, and long-term processes like tides, storm set-up, atmospheric pressure, and sea level rise. Figure 7.1 shows some of them and their frequency ranges. Each of these components will have to be dealt with differently. The goal is to condense the effects of this broad spectrum of fluctuations into two parameters; the average sea water level h_S and average local wind velocity U_{10}:

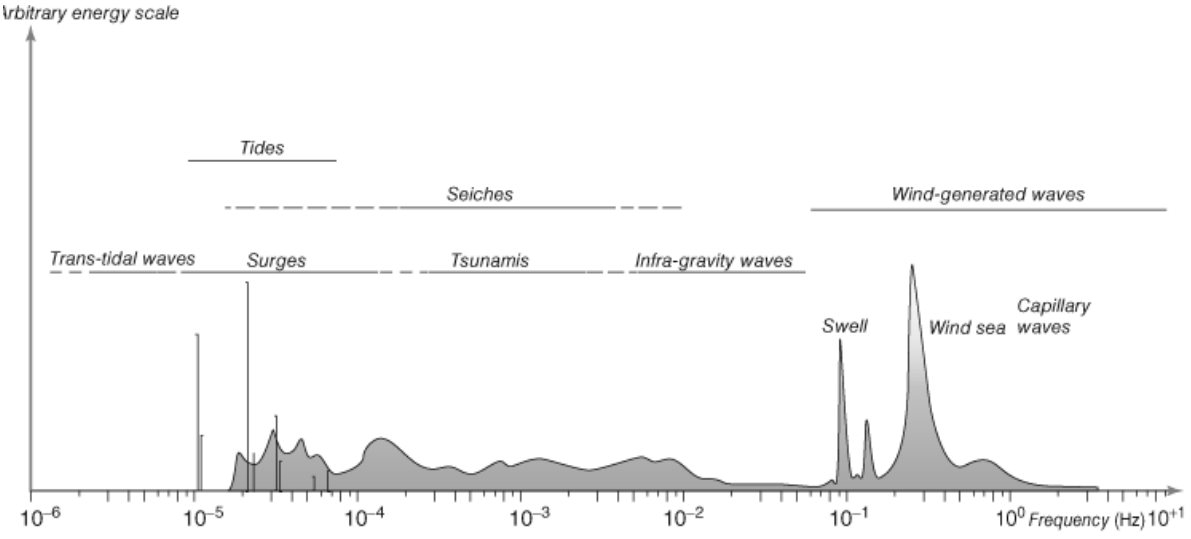

Figure 7.1: Wave type classifications and their associated frequencies. [14]

7.1.1. Short term processes

Short-term water level fluctuations occur on a scale between fractions of a second to a few minutes, and are mostly caused by wind. These waves can be formed by local winds shearing the water surface over a certain distance, but can also be the remnants of far-away storms. These so-called swell waves have longer periods than locally generated wind waves (See Figure 7.1). How these short term water level fluctuations are derived from the local wind velocity U_{10} and average sea water level h_S has already been described in Chapter 3.

7.1.2. Long term processes

Long term processes are defined as fluctuations in the water levels whose period can have an order of magnitude varying from several hours to decades. These can also be split into two types: recurring processes whose effects can be expected to average out and stay constant over the lifetime of the structure (e.g. tides), and processes which cause a non-periodic change over time (e.g. sea level rise).

- **Recurring long-term processes**
  This category mainly consists of tides, surges, atmospheric pressure fluctuations, and other recurring, slow, and temporary changes to the water level. Because these events are assumed to remain equally prevalent over time, probability distributions derived from historical data can be used to characterise events that will occur in the future. Historical data is available in hourly intervals, which offers an opportunity to include these effects without having to separately model every process. Because the periods of all of these processes are longer than several hours, the historical hourly average water level reflects all the different combinations of these effects and how often they occur. Short-term processes with periods below one hour on the other hand are averaged out.

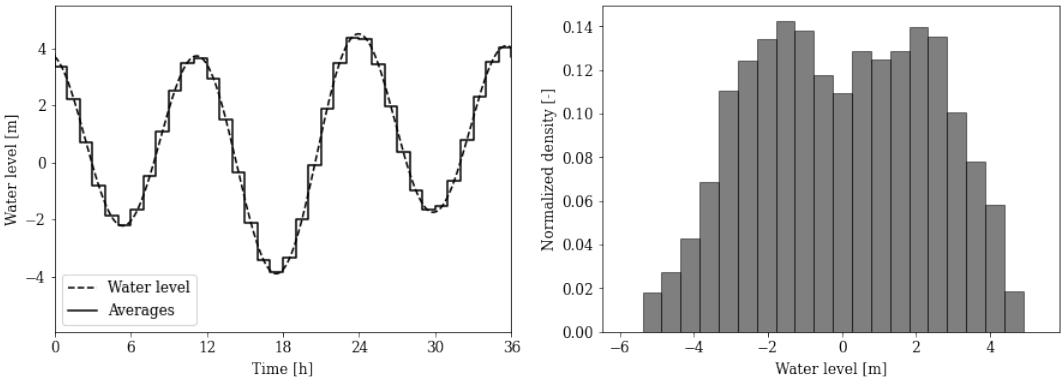

Figure 7.2: Left: Continuous and discretized water levels of hypothetical time series. Right: Histogram of the averages.

  Once the historical data is discretised like this, a probability distribution $f_p(h_{av})$ of the combined effect of long-term fluctuations can easily be obtained (Example in Figure 7.2). This probability distribution can then be used to generate random hourly average water levels h_{av} for future events.

- **Non-periodic long-term processes**
  This category mainly consists of two processes; climate change and soil settlement. Climate change stands apart from the previously mentioned effects because it adds up over time and the change between the start and end of the structural lifetime isn't present in historical data. Therefore climate change will have to be probabilistically added to all of the average water levels h_{av} generated from the probability distribution by randomly placing them on the timeline and adding the projected amount of sea level rise h_{SLR} at that point in time. It can be assumed that the wind velocities will not be significantly affected [1]. The same method can be applied to soil settlement, but for this thesis it is assumed not to occur.

With that, the hourly average water level h_S over the lifetime of the structure can be probabilistically estimated by generating the desired amount of hour-long averages from the probability distribution and adjusting them for climate change and soil settlement.

$$h_S = h_{av} + U(0, h_{SLR,T}) \tag{7.1}$$

where $U(0, h_{SLR,T})$ is a uniform distribution from 0 to the sea level rise at the end of the structural lifetime $h_{SLR,T}$. This does assume a single climate scenario; the total sea level rise could also be modelled as a probability function to reflect the uncertainty of long-term projections, but because flood defence projects are often designed for a specific scenario it is left as a constant. Modelling these processes as averages does ignore the contribution of their loading- and unloading cycles to the fatigue. This is justified because some quick checks show that the stress cycles associated with quasi-static tidal fluctuations are far below the cut-off limit of $\Delta\sigma_L \approx 40$MPa for detail category $\Delta\sigma_c = 100$MPa. Even a rather large tidal cycle from $h_S = 4m$ to

$h_S = 6m$ is found to cause a stress difference of only 12MPa at the middle of the gate (for Gate design 1 from the case study in Chapter 8). It is therefore deemed acceptable to ignore them.

7.1.3. Probability distributions

The adjusted probability distributions are derived from a limited dataset (50-100 years), and therefore don't necessarily include extreme events that only occur once every 10.000 years. Because these are very important from a design perspective the data will have to be extrapolated to give a more robust dataset to work with. There are e.g. complex SWAN models which can create projections in great detail, but for the purposes of this report a simpler method will be employed. For a proper design the boundary conditions will be more rigorously defined.
The degree of correlation between these variables can be determined with a metric like the Pearson correlation coefficient:

$$\rho_{h_S,U_{10}} = \frac{cov(h_S, U_{10})}{\sigma_{h_S}\sigma_{U_{10}}} \tag{7.2}$$

This value shows the degree of correlation between two variables, and varies between -1 and 1. Values smaller than 0.3 are generally modelled as independent, so this will also be assumed here. Tail events tend to exhibit higher correlations however, so a correlation could be applied there to increase the accuracy. Examples of independent fitted distributions for average wind and water level data are given in Figure 7.3.

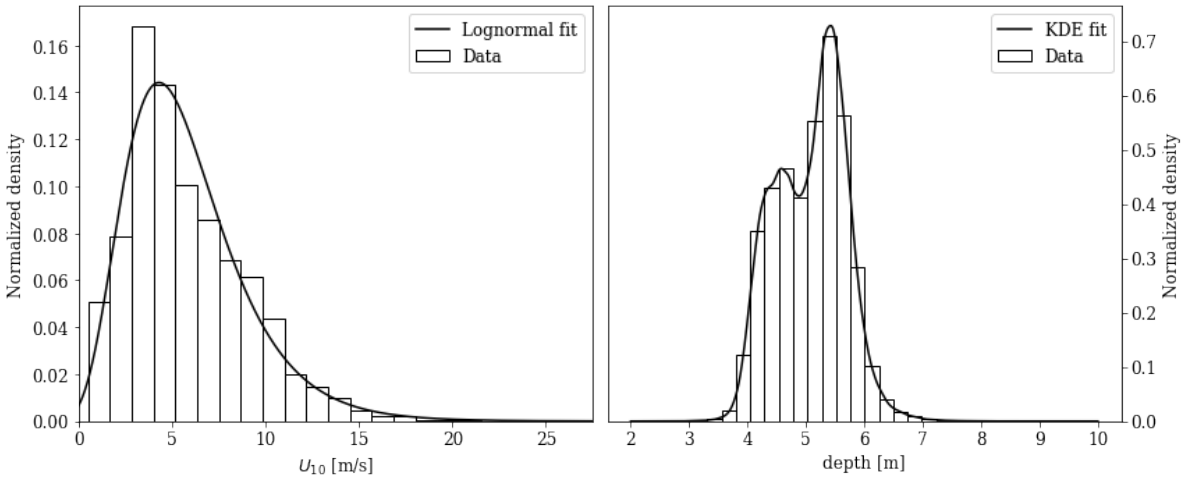

Figure 7.3: Histograms of raw U_{10} and h_S data, and their fitted probability density functions.

The average water level still has to be adjusted for climate change however. As mentioned in Section 7.1.2, this is done by adding a uniformly distributed value between 0 and the projected sea level rise at the end of the structure's lifetime (Eq. 7.1). A more sophisticated distribution which takes growth rates and different scenarios into account could also be used. Adding the probability distributions of two independent random variables is done with a convolution:

$$f_H(h_S) = \int_{\infty}^{\infty} f_1(\tau) f_2(h_S - \tau) d\tau \tag{7.3}$$

Where in this case f_1 and f_2 are the probability densities of the raw average water level data and climate change, and f_H is the probability density of the climate change-adjusted average water level. An example of two original probability distributions and the resulting convoluted probability density function are plotted in Figure 7.4.
Together with the fitted probability density function $f_U(U_{10})$ for U_{10} these two independent probability density functions can be multiplied to find the joint probability density function of U_10 and h_S.

$$f_J(h_S, U_{10}) = f_H(h_S) \cdot f_U(U_{10}) \tag{7.4}$$

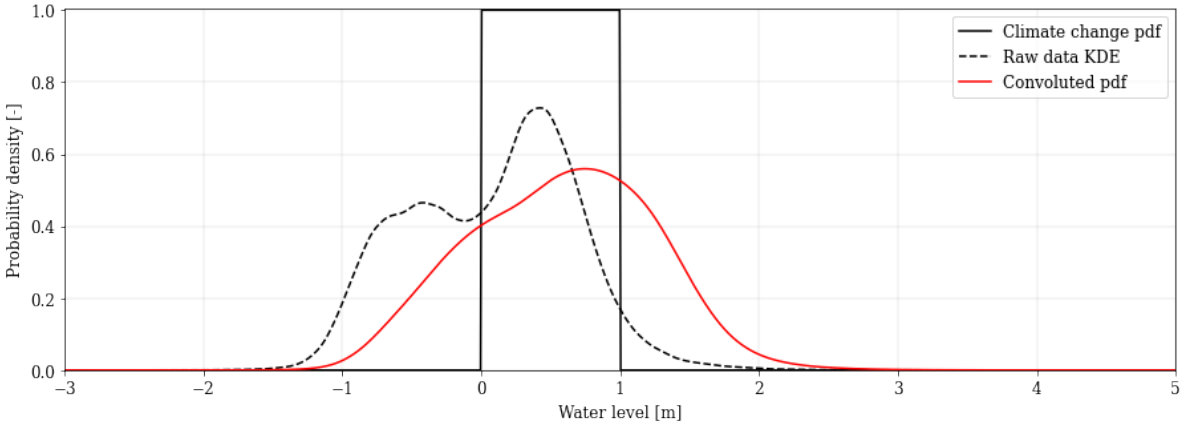

Figure 7.4: Probability density functions of raw water level data, a +2m climate change scenario, and their combined values.

7.2. Discrete load cases

Because the joint probability density function can't be run through the calculation directly, the data is instead discretised into a more manageable amount of representative cases which will be characterised by the expected values of the two variables over a certain segment of the density function. The resolution used to segment the probability density function has an effect on both the computation time and the accuracy, so a satisfactory compromise has to be found.

7.2.1. Method

In order to find a discrete set of load cases, the joint probability density function is divided into a grid of equal-sized segments, each of which is characterised by representative values for h_S and U_{10}, as well as a probability. The expected values of two independent random variables h_S and U_{10} with a probability density function $f_J(h_S, U_{10})$ on an interval $\left[(H_i < h_S < H_{i+1}), (U_j < U_{10} < U_{j+1})\right]$, is given by Equation 7.5.

$$E[(H_i < h_S < H_{i+1}), (U_j < U_{10} < U_{j+1})] = \frac{\int_{H_i}^{H_{i+1}} \int_{U_j}^{U_{j+1}} h_S \cdot U_{10} \cdot f_J(h_S, U_{10}) dU_{10} dh_S}{\int_{H_i}^{H_{i+1}} \int_{U_j}^{U_{j+1}} f_J(h_S, U_{10}) dU_{10} dh_S} \tag{7.5}$$

The probability associated with that particular segment is found by integrating $f_J(h_S, U_{10})$ over the interval:

$$p\left((H_i < h_S < H_{i+1}), (U_j < U_{10} < U_{j+1})\right) = \int_{H_i}^{H_{i+1}} \int_{U_j}^{U_{j+1}} f_J(h_S, U_{10}) dU_{10} dh_S \tag{7.6}$$

The sum of the probabilities of all these segments add back up to 1. The dimensions of the intervals are determined by the resolution parameters:

$$\text{res}_{h_S} = H_{i+1} - H_i \tag{7.7}$$

$$\text{res}_{U_{10}} = U_{j+1} - U_j \tag{7.8}$$

7.2.2. Resolution choice

In order to determine the optimal resolution in both directions, the effect on the standard deviation of the results will be measured. The upper limit for accuracy is a resolution of zero; the standard deviation of the fatigue associated with this result is found by running the exact same case multiple times. This was already done in Section 6.4. It reflects the uncertainty inherent to the physics of the fatigue model.

The result of a 2D-segment has more uncertainty, because now the inputs are also probabilistic. This is masked by taking the expected value of the segment and using it as a representative value, but in the probabilistic lifetime simulation at the end of the framework it should be artificially added back in to reflect the uncertainty introduced by the process of segmenting the joint probability function into discrete load cases.

For example, if res_{h_S} is 1 meter a random h_S-value from the segment with a representative value of $h_S = 5$m could be anywhere from 4.5m to 5.5m. This can have a large impact on the fatigue calculation.

The loss of accuracy due to the discretisation process is determined with the following steps:

1. Run the fatigue analysis N times for the representative values of h_S and U_{10}.
2. Run the fatigue analysis N times for random values in a range of res_{h_S} by $\text{res}_{U_{10}}$ around the representative values.
3. Compare the standard deviations of the two sets of results

This was done for a range of resolutions along both axes. The data used for this is from the case study in Chapter 8. Results are plotted in Figure 7.5.

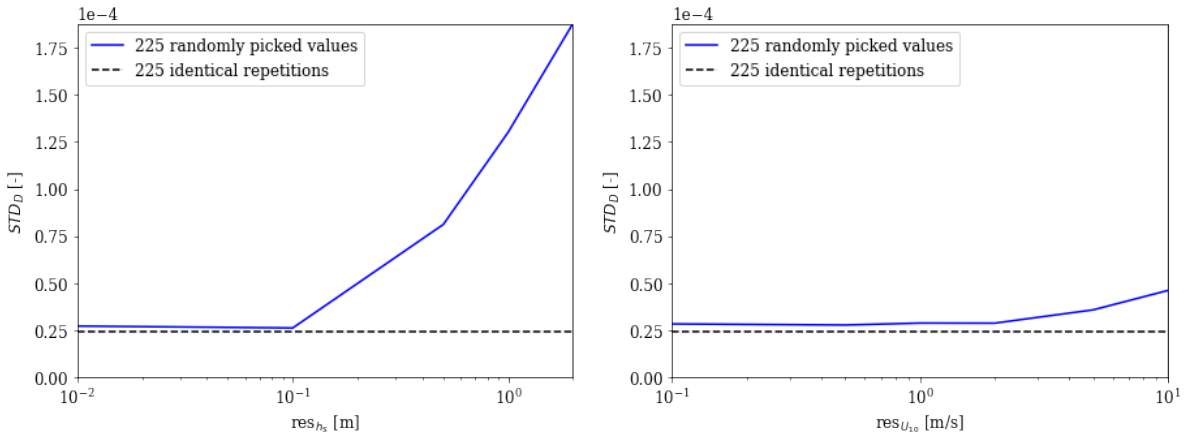

Figure 7.5: Boxplots of fatigue results.

It's clear that the water level has a much stronger effect on the uncertainty of the outcome than the wind velocity. Both will asymptotically approach the horizontal line which is the standard deviation for identical repetitions of the representative values. A trade-off has to be made between the difference between narrowing the gap between them and computation time. For this thesis, res_{h_S} is chosen at 0.1m and $\text{res}_{U_{10}}$ at 1m/s, because this is where they get close enough to the asymptote and the marginal gain of further increases becomes almost zero while computation time keeps rising. This is not a general rule however; for example in a case at open sea the result could be much more sensitive to wind because wave development isn't depth-limited there like it is for the data used here.
The result is a grid with segments of size res_{h_S} by $\text{res}_{U_{10}}$, each of which has a representative value for h_S and U_{10} as well as a probability. As an example the 4480 load cases for the case study are plotted in Figure 7.6.

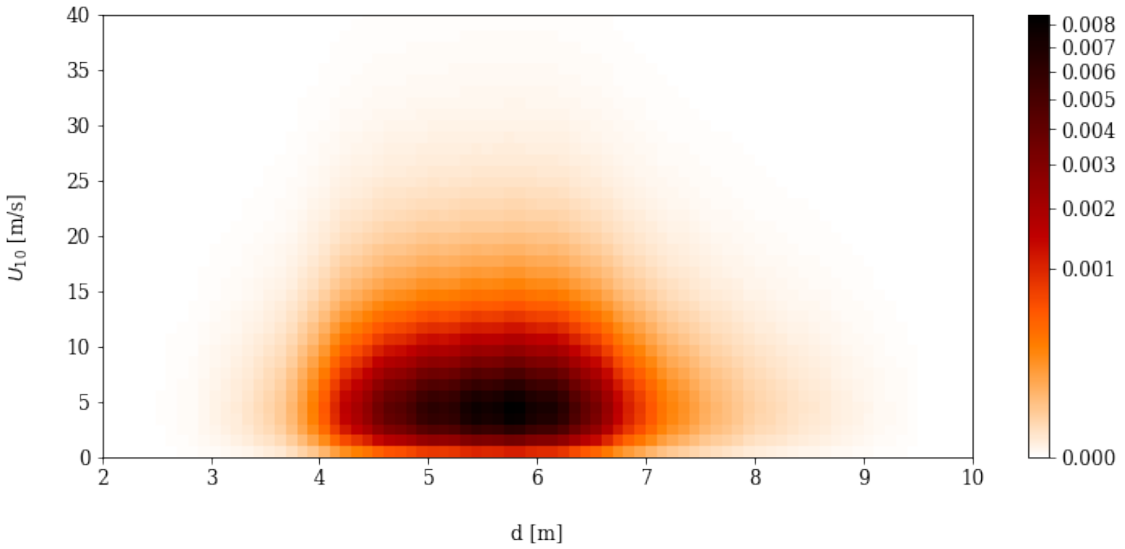

Figure 7.6: Grid of load cases for case, colour-coded to reflect their probability.

7.2.3. Filtering load events

A lot of the load cases defined in the previous section will not meaningfully contribute to the fatigue because either the wind is too weak to create significant waves, the water level too low for the waves to reach the overhang, or the probability so low that the chance of occurrence is negligible. To reduce computation time, these load cases will therefore be filtered before proceeding. This procedure is not necessary for the model to work, but can help make it more efficient.

- Wave height filtering

  A conservative filter is defined to remove the events where the sum of the statistical maximum wave height and the highest water level does not exceed the elevation of the overhang. These are statistically very unlikely to experience any impulsive impact forces at all. The statistical maximum wave height produced by a random realisation of a wave spectrum is generally defined as $H_{max} = 2H_{m0}$ [14]. Taking the reflection coefficient of the gate c_r into account, this gives a maximum water level fluctuation of $2H_{m0}(1+c_r)$. H_{m0} is found by generating the spectrum for each load case (See Chapter 3) and computing $H_{m0} = 4\sqrt{m_0}$, where m_0 has been defined in Equation 3.1. The check being performed is therefore:

  $$2H_{m0}(1+c_r) > h_G \tag{7.9}$$

  Any load events which do not satisfy this criterion are removed.

- Frequency filtering

  Next, the events with a negligible chance of occurrence are removed. For design purposes once in 10,000 year events are generally the rarest ones considered, so for this thesis all load cases with a lower probability than $(10{,}000 \cdot 365.25 \cdot 24)^{-1} = 1.14e^{-8}$ will be filtered as well.

When applying both filters to the example data shown in Figure 7.6, the amount of cases reduces with 66% from 4480 to 1483. The new load case grid is plotted in Figure 7.7 Running the fatigue analyses for the load cases on the edge of this filter confirms that they have a fatigue damage factor of 0.

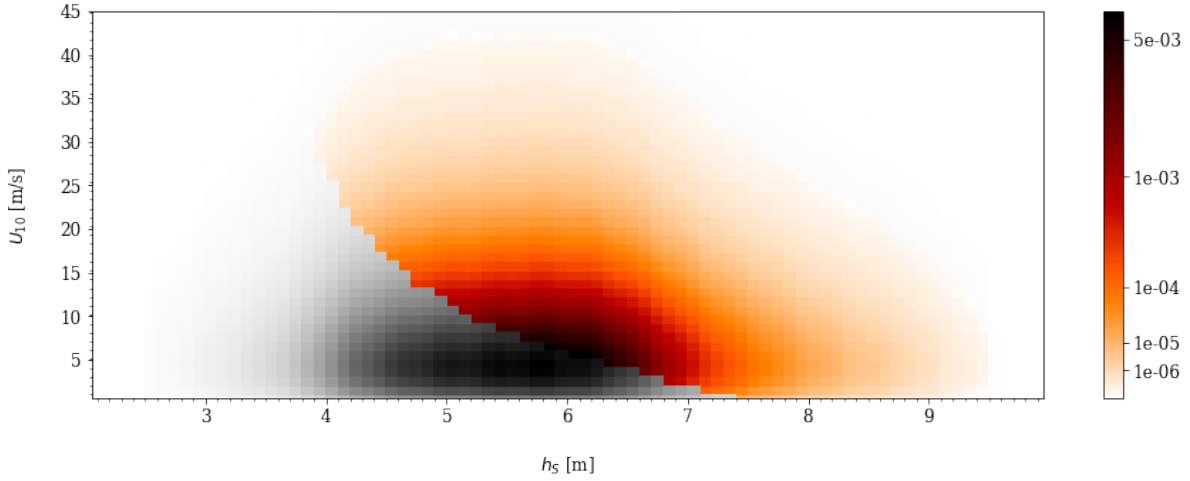

Figure 7.7: Grid of load cases for case, colour-coded to reflect their probability. Grey cases have been filtered out.

7.3. Lifetime fatigue

Now that the fatigue due to any 1-hour load case can be computed and a set of discrete load cases has been defined, these processes can be combined to simulate the entire lifetime of the structure. The fatigue D_i as a result of each of the 1000-2000 load cases with their representative values for $U_{10,i}$ and $h_{S,i}$ and associated probability $p(D_i)$ is computed. The total lifetime fatigue D_L is found by combining these load events with their probability of occurrence $p(D_i)$ and the amount of hours the structure is expected to endure (T_L). There are two ways to do this: the quickest is to simply add the products of the fatigue outcomes and their probabilities to find the average expected fatigue damage, and multiply it with the number of hours T_L to obtain the total expected fatigue damage D_E:

$$D_E = T_L \cdot \sum_{i=1}^{T_L} p(D_i) \cdot D_i \tag{7.10}$$

This does not reflect the sampling uncertainty however, as sometimes stronger load cases can occur more often compared to the average by chance. For a more comprehensive result a Monte Carlo analysis is needed.

7.3.1. Monte Carlo

The Monte Carlo analysis randomly samples T_L fatigue numbers based on the associated probability distribution. The lifetime of the structure is simulated 1000 times to capture this natural variance. The average result from the simulations D_L (which approaches D_E) is plotted in Figure 7.8 along with the maximum and minimum scenarios. All outcomes fall within a range of roughly 4% on either side of the average. A conservative value like the upper bound of the 95% confidence interval can then serve as the design value for the fatigue at the end of the lifetime.

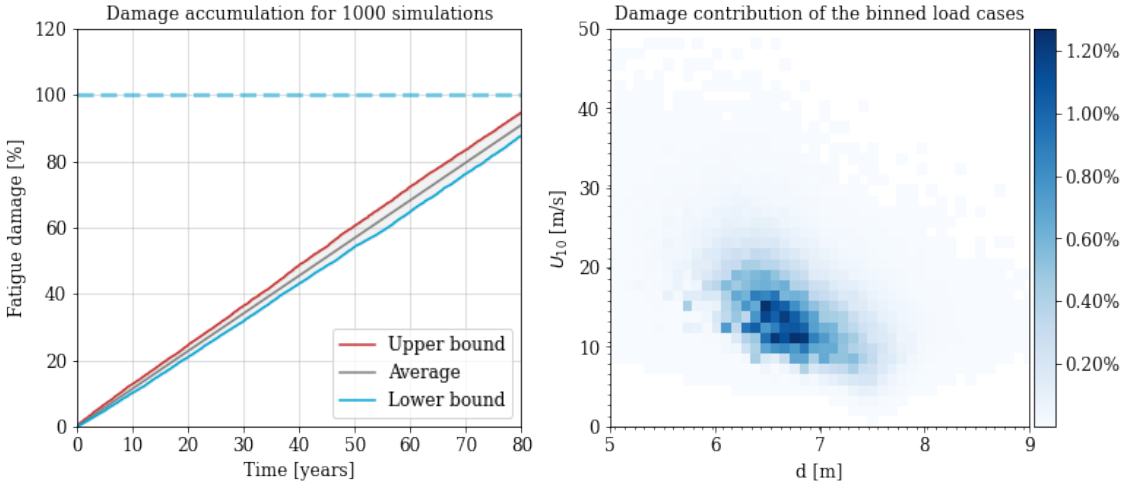

Figure 7.8: Left: Results of Monte Carlo analysis. Right: Average contribution of the different load cases.

The result shows that relatively common but non-negligible load combinations contribute most to the overall fatigue compared to more extreme events. Part of this is probably due to the shallow water depth, which limits the maximum wave height caused by extreme storms. This also follows from the earlier conclusion that fatigue scales roughly linearly with the wind velocity (Section 6.4); because the lognormal probability drops much faster than the damage increases, the overall contribution will decline as well.
Tests were run to determine to what extent the model uncertainty described in Sections 6.4 and 7.2.2 contributes to this spread, but the difference was found to be very minor. Lifetime simulations were performed for standard errors ranging from 0-50% (See Figure 7.9). While still relevant for individual simulations, it is therefore not very important for a lifetime analysis where these effects average out over time. A conservative standard error of 20% is applied to all cases based on the results from Section 6.4.

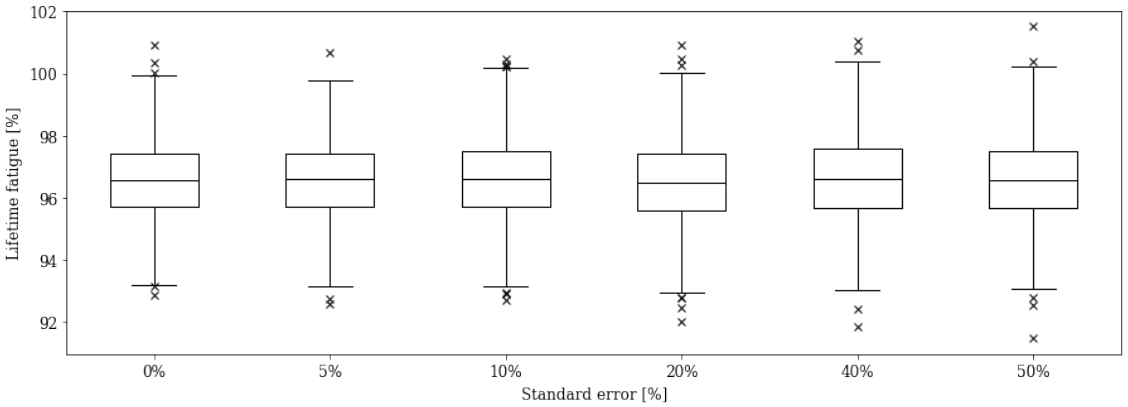

Figure 7.9: Boxplots of the lifetime fatigue results for different standard errors for the representative values.

8

Case study

The case study will consider a hypothetical gate adjacent to the Waddenzee, and evaluate different designs based on the methods outlined in Chapters 3 through 7. But first, the boundary conditions will be defined.

8.1. Site description

The site is located at the Den Oever sluice complex, at the lower end of the Afsluitdijk which separates the IJsselmeer and the Waddenzee. Because the complex has two gates per drainage channel and westerly winds are dominant, this report will only consider storm loads on the Waddenzee side of the discharge complex. For the purpose of modelling wind set-up and wave formation the maximum fetch is estimated at 30km (distance to Vlieland), and no swell waves are allowed to penetrate through the gaps in the island chain. It is assumed that the average depth at $t = 0$ is 5.0m over this entire distance (In reality it varies from 1m to 25m below NAP, see Figure 8.1). The gate will be designed to last up to the year 2100.

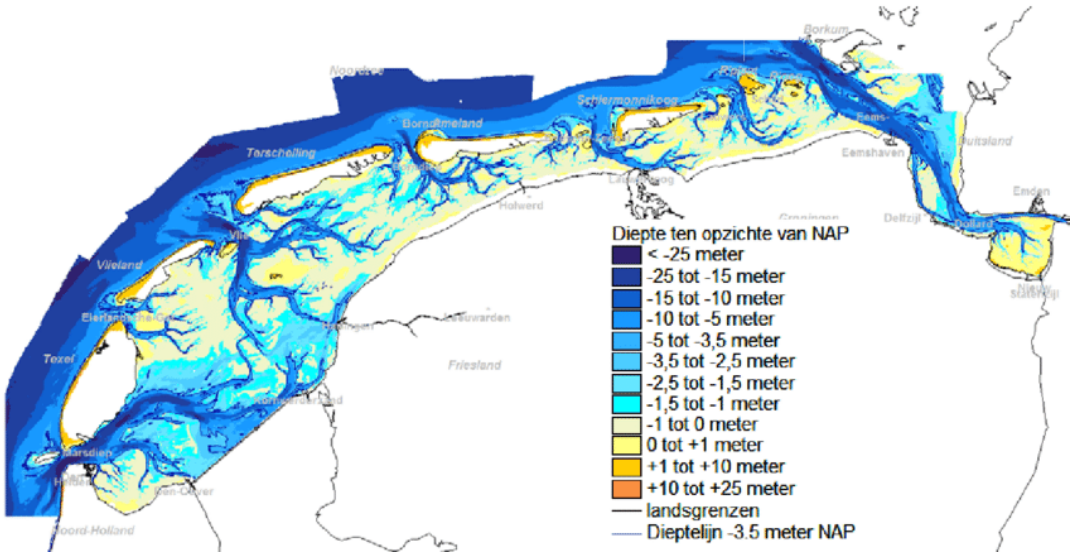

Figure 8.1: Map of the depth of the Waddenzee (RIKZ, 1998)

As has been mentioned in Chapter 7 creating a rigorous set of boundary conditions is outside of the scope of this study, but for verification purposes some readily available data will be used to approximate the storm climate at Den Oever. For the chosen measurement stations Rijkswaterstaat [29] and KNMI [16] provide hourly water level and wind velocity data going back to 1971. This simplified method will serve as a proof of concept and framework for a more rigorous design.

The water level data was measured on the location of the structure, at Den Oever. Wind data will obtained from the measuring station at De Kooy, 16.5km to the west. The location of these two measuring stations can be seen in Figure 8.2. Both stations have hourly data available from 01-01-1971 to 01-01-2020, meaning the raw data describes 49 years of environmental conditions.

Figure 8.2: Location of the measurement stations (Google Maps)

The covariance of these two variables is evaluated with the Pearson coefficient (Section 7.1.3):

$$\rho_{U_{10},h_S} = \frac{cov(U_{10},h_S)}{\sigma_{U_{10}}\sigma_{h_S}} = 0.158 \tag{8.1}$$

Values smaller than 0.3 are generally assumed to be independent, so this assumption will be made here as well. This means that two separate probability density functions will be fitted to the data. A least squares analysis was performed for all major distribution types, after which the wind velocity U_{10} was found to most closely resemble a lognormal distribution:

$$f(U_{10}) = \frac{1}{(U_{10}-\mu)\cdot\sqrt{2\pi\sigma^2}} e^{-\frac{log(\frac{U_{10}-\mu}{\alpha})^2}{2\sigma^2}} \tag{8.2}$$

where $\sigma = 0.35$, $\mu = -3.06$, and $\alpha = 8.34$. The water level doesn't follow a common distribution because the strong influence of the tides give it a bi-modal character. A Kernel Density Estimate is therefore performed, which assumes that the underlying data is Gaussian. The functions are plotted in Figure **??**. For reference the projected wave height for 1/10,000 year wind conditions and the least favourable water depth of 7.5m is 3.94m according to the extrapolation, whereas Groeneweg et al. [12] projects 3.25m as the 1/10.000 year wave condition. Even though the combined probability of the water level and wind velocity will be higher (See Section 8.5), this difference is deemed acceptable for this demonstration.
Next, the water level distribution is adjusted for climate change according to the method described in Section 7.1.3. The recommended design values for sea level rise h_{SLR} are +40cm by 2050 and +1m by 2100 [2]. It is not necessarily true that the worst climate scenario also corresponds to the worst fatigue lifetime however. If the gate is fully immersed during the strongest load events this can result in lower impact loads. A brief sensitivity analysis will therefore performed in Section 8.6 to investigate the effect of various climate change scenarios on the fatigue lifetime of the gate. The worst case scenario of +1m is assumed for this case study, and added to the data according to Equation 7.3. The resulting convoluted density function was shown in Figure 7.4.
These probability density functions are then transformed into 4480 discrete load cases according to the steps described in Section 7.2, the result of which was plotted in Figure 7.6. The load cases are then filtered based on their intensity and frequency according to the rules described in Section 7.2.3, which reduces the set of load cases to 1483. The resulting filtered set of load cases was plotted in Figure 7.7.

8.2. Gate designs

The parametric shape of the gate has already been defined in Chapter 5. In this case study, two valid variants of this parametric shape will be evaluated to compare the effect on the modes, and material efficiency. Each will be iteratively designed to fulfil the lifetime fatigue capacity requirement. Rather than showing all the iterations only the final designs will be discussed. The design process consists of the following steps:

1. Calculate the fatigue damage $D_i(x, y, z)$ due to a random storm event at every gate coordinate to identify where the gate experiences the most fatigue and which modes are mobilised.
2. Calculate the accumulated fatigue D_L over the lifetime of the structure at the previously identified critical coordinates (x_c, y_c, z_c) and check whether it exceeds the fatigue capacity.
3. Perform a probabilistic ULS check at (x_c, y_c, z_c) for the gate design using 1/10.000 year wind conditions and the least favourable water level to determine the failure probability under those circumstances.

Finally, the two designs will also be compared for material efficiency. The dimensions that will be used for these examples are not particularly realistic because the current iteration of the model is quite simplistic in the way the stiffeners are applied. A real gate will have secondary and tertiary stiffeners as well to help spread the load. The first gate design that will be considered will rely on large stiffeners to carry the load. Its geometry is defined in Table 8.1 under 'Gate 1'. The second design, called 'Gate 2' from here on, will instead be designed with smaller stiffeners but a very strong skin plate. This latter design will have its stiffness more uniformly distributed, and is therefore expected to mobilise the higher modes to a lesser degree. Both will be designed to approximately the same fatigue lifetime, but will respond differently due to their different shapes. The framework described in the report gives the user insight in which ways their respective responses and fatigue distributions differ.

		Gate 1		**Gate 2**	
Symbol	Description	Value	Unit	Value	Unit
W	Gate width	10	m	10	m
h_G	Gate height	7.5	m	7.5	m
t_G	Skin plate thickness	0.05	m	0.18	m
t_v	Vertical stiffener thickness	0.1	m	0.1	m
$t_{h,mid}$	Middle horizontal stiffener thickness	0.1	m	0.1	m
t_{h_edge}	Outer horizontal stiffener thickness	0.1	m	0.1	m
L_{web}	Vertical stiffener length	0.71	m	0.4	m
L_{girder}	Horizontal stiffener length	0.71	m	0.4	m
ρ_s	Density of steel	7,850	kg/m^3	7,850	kg/m^3
E_s	Young's Modulus of steel	210	GPa	210	GPa
f_{yd}	Yield strength	355	MPa	355	MPa
σ_C	Detail category	100	MPa	100	MPa
ζ	Damping ratio	0.02	-	0.02	-
m_G	Gate mass	70.9·10^3	kg	129.7·10^3	kg

Table 8.1: Case study gate design parameters.

The mass in Table 8.1 found with Equation 8.3.

$$m_G = \rho_s \cdot \left(h_G \cdot W \cdot t_G + n_v \cdot h_G \cdot t_v \cdot L_{girder} + n_h \cdot W \cdot t_h \cdot L_{web}\right) \tag{8.3}$$

The first in-vacuo and immersed eigenfrequencies of both gate systems are given in Table 8.2, and the corresponding stress modes shapes $S_{p,m}(x, y, z)$ in Figures 8.3 and 8.4.

	Gate 1				**Gate 2**			
Mode	In vacuo		Immersed		In vacuo		Immersed	
1	15.4	Hz	5.7	Hz	6.9	Hz	3.4	Hz
2	18.5	Hz	10.5	Hz	10.7	Hz	7.0	Hz
3	50.4	Hz	29.3	Hz	27.0	Hz	16.1	Hz
4	51.3	Hz	38.4	Hz	29.5	Hz	21.8	Hz

Table 8.2: In vacuo and immersed eigenfrequencies.

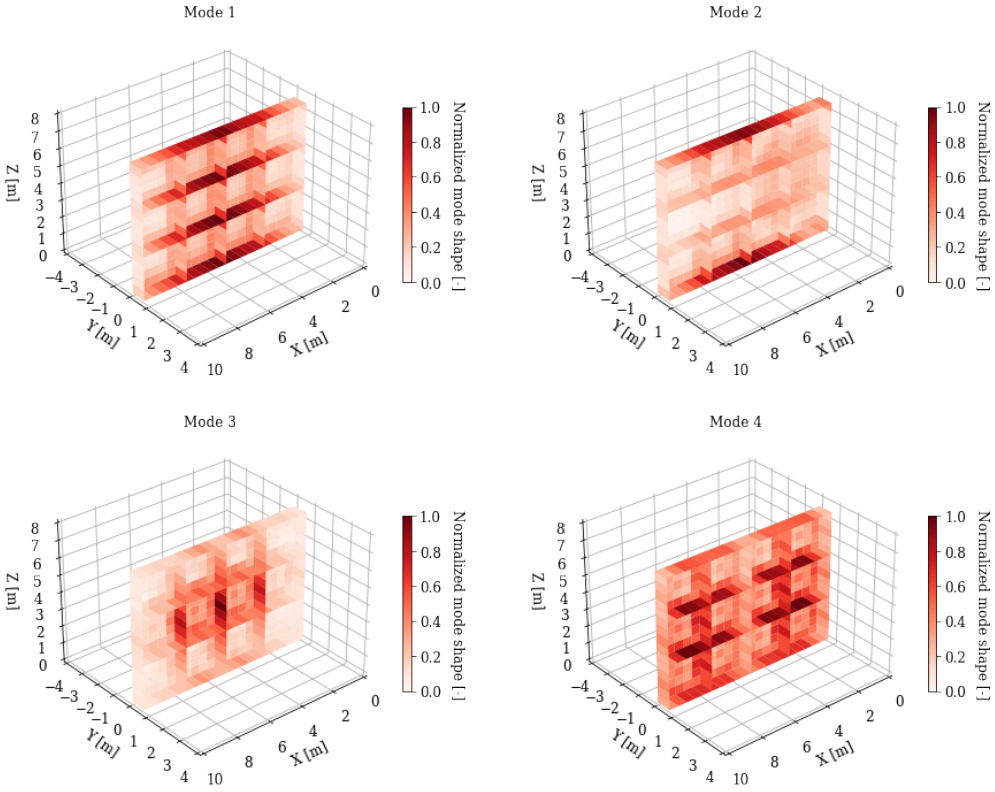

Figure 8.3: First four principal stress modes $S_{p,m}(x, y, z)$ for Gate 1

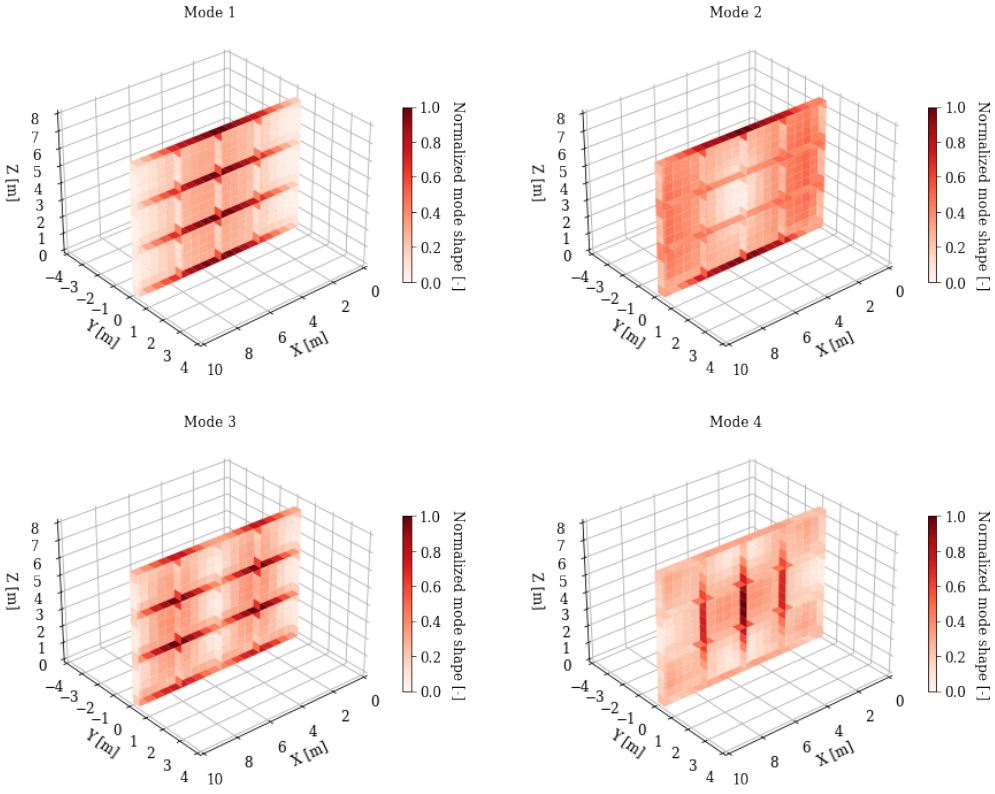

Figure 8.4: First four principal stress modes $S_{p,m}(x, y, z)$ for Gate 2

Before proceeding to the design, the response of the two gates will first be compared. The principal stress response of the two designs to a wave impact with wave height H_s = 1.5m, wave period T = 3s, and wave impact duration $\tau = 0.01s$ is plotted in Figure 8.5.

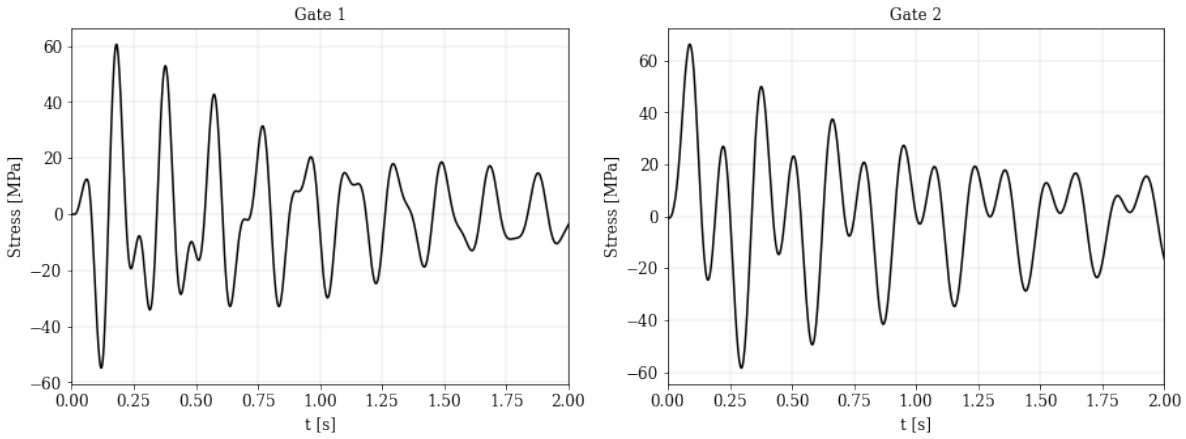

Figure 8.5: Response of both gates at (x=5;y=L_{web};z=7.5)

While the responses are clearly of a similar magnitude but different, it is not very intuitive what exactly causes it. To analyse this the response is split up into its constituent modes in Figure 8.6. Only modes whose peak value is higher than 1% of the peak value of the total response are plotted, for clarity.

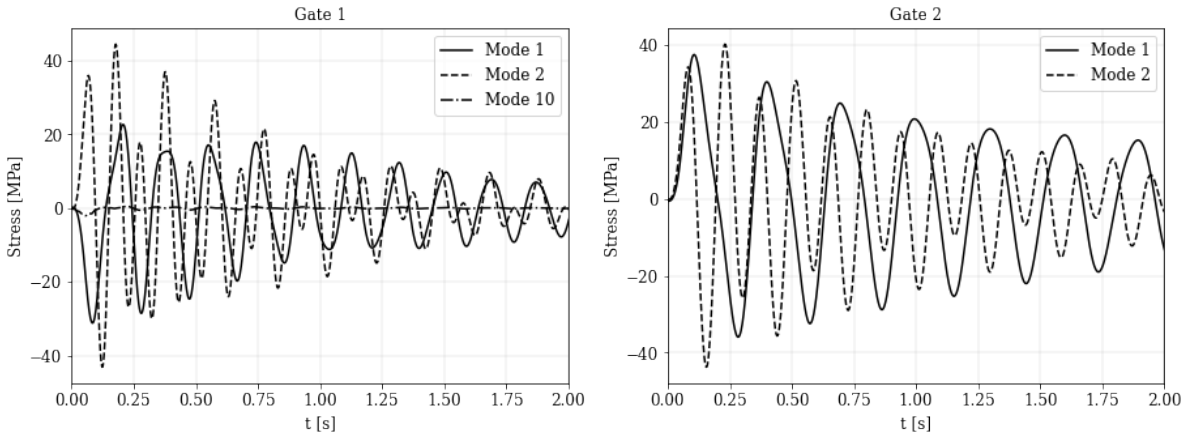

Figure 8.6: Response per mode of both gates at (x=5;y=L_{web};z=7.5)

This shows that in Gate 2 the first mode excited more strongly than in Gate 1, which lines up with the prediction made earlier. This is only one coordinate of the gate however, for a more comprehensive view of the response of the gate the response will have to be compared across the entire surface and for a full load spectrum rather than a single wave.

8.3. Fatigue distribution over gate surface

The fatigue damage factor $D_i(x,y,z)$ is computed at every coordinate of Gate 1 for a single load event to determine which points of the gate experience the most fatigue. In this case the example load event is one hour of 20m/s wind and a water depth of 7m. After finding the stress histories for every coordinate with the method from Chapter 5 their fatigue damage $D_i(x,y,z)$ is computed with the Palmgren-Miner method from Section 6. Based on these results, the critical points of the gate can be identified and reinforced at the expense of lesser affected areas if necessary. The fatigue damage factor D for this event across both gates is plotted in Figure 8.7.

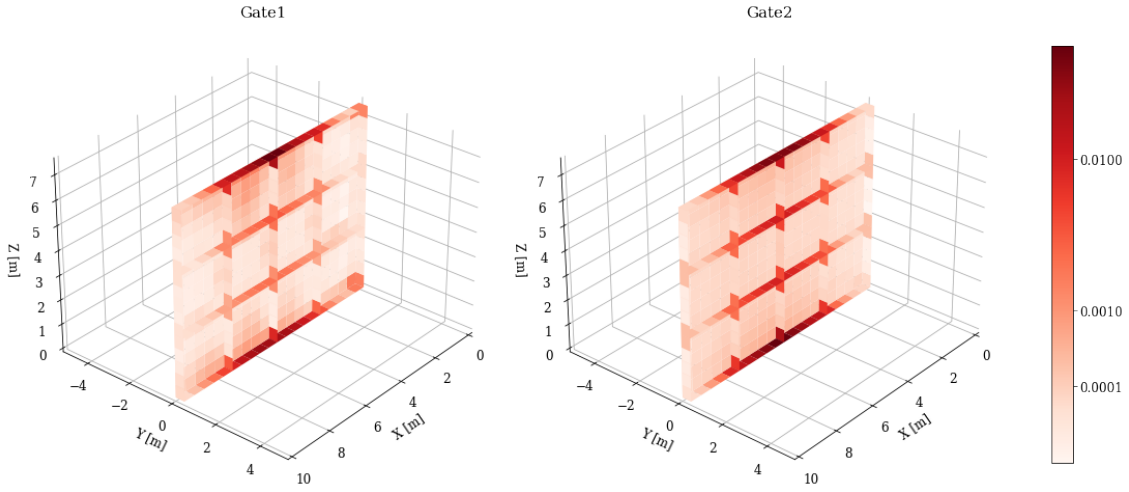

Figure 8.7: Fatigue damage factor D for every coordinate due to an example load event.

The upper and lower horizontal girders experience the most fatigue for both gates due to the asymmetric wave impact and the lack of supports leaving them free to deflect. The concentrations in the corners at $x = 0$ are due to the FEM model being supported in the x-direction only on that side. By reinforcing the high-fatigue areas at the cost of less affected ones the gate can be made to resist loads more effectively and efficiently. For both gates the highest fatigue damage occurs at the tips of the stiffeners ($x = 5; y = L_{web}; z = 7.5$).
But there are also differences. Gate 2 has its fatigue damage distributed much more uniformly because most of the stiffness being located in the thick plate makes it more similar to a homogeneous slab. The skin plate experiences more fatigue and the middle stiffeners are also mobilised more strongly. Gate 1 on the other hand has most of its fatigue concentrated in the upper and lower stiffeners, suggesting a strong effect of the second mode (Figure 5.3).
This second mode is mobilised by the asymmetric impact force which is concentrated at the top. The relative importance of the modes will first be quantified by comparing the integrals of the stress spectra for each mode. The stress spectrum of each mode ($R_m(f,x,y,z)$ from Eq. 5.38) was integrated and divided by the total at every coordinate to measure their relative contribution $C_{\%}(m)$ to the total response for all 16 modes.

$$C_{\%}(m) = \frac{\int R_m(f,x_c,y_c,z_c)df}{\sum_{m=1}^{16}\int R_m(f,x_c,y_c,z_c)df} \cdot 100\% \tag{8.4}$$

On the left of Figure 8.8 the average relative stress contribution $C_{\%}(m)$ is plotted. The bars indicate the mean of all coordinates and the error bars indicate the range. The graph on the right shows $C_{\%}(m)$ for each mode at the critical point.
On average the second mode is more important than the first for both gates. At the critical point (x=6;y=L_{web};z=7.5) it is dominant for Gate 1 and equally as important as the first mode for Gate 2. The cumulative graph shows that in order to capture 90% of the combined stress of the first sixteen modes at the critical point, 3 modes are needed for Gate 1 and 2 for Gate 2. The ranges in the leftmost image show that for some other, non-critical points the higher modes are more important, so that on average the first 14 modes would be needed to capture 90% of the response of the first 16 modes for Gate 1.
But this does not necessarily mean that the fatigue follows the same distribution. Adding separate modal stress histories has a nonlinear effect on the stress cycles, which together with the logarithmic fatigue calculation means a different comparison has to be made. To measure the effect of different modes on the fatigue,

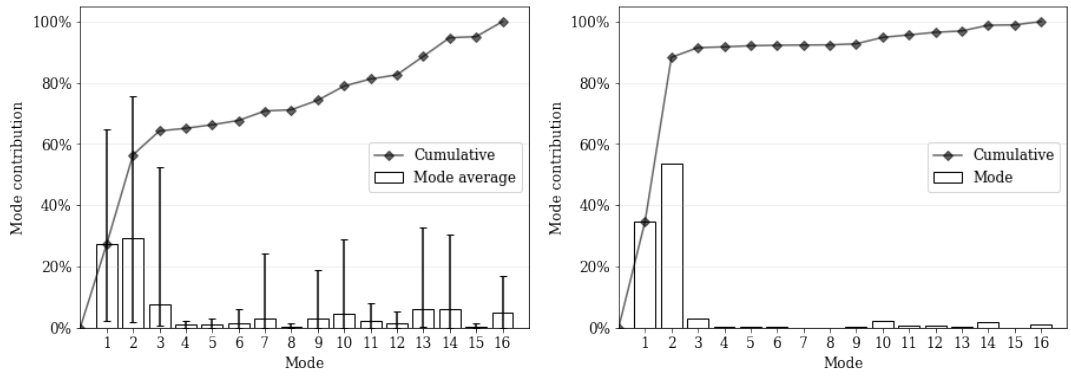

Figure 8.8: Left: Average $C_{\%}(m)$ and range over all coordinates for Gate 1. Right: $C_{\%}(m)$ at (x=5;y=0.71;z=7.5).

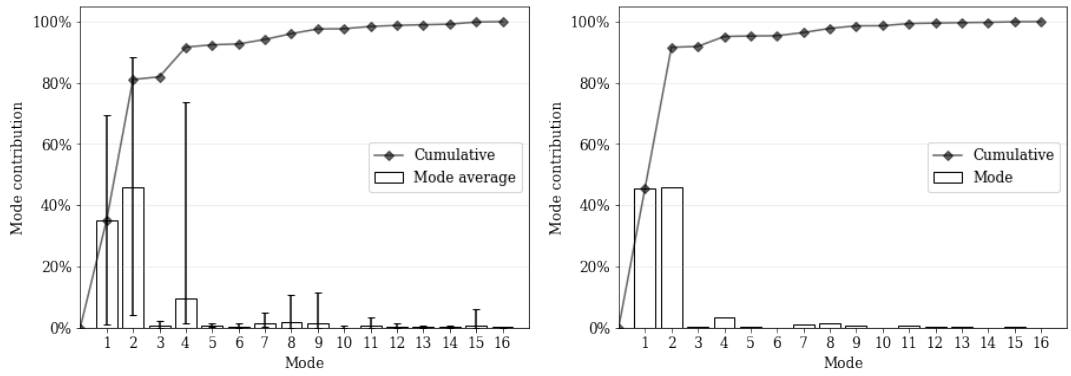

Figure 8.9: Left: Average $C_{\%}(m)$ and range over all coordinates for Gate 2. Right: $C_{\%}(m)$ at (x=5;y=0.4;z=7.5).

the desired coordinate will be evaluated for fatigue for the combined response of every mode except one (Mršnik et al. [26]). The difference between the total fatigue D_t and the partial fatigue with one mode missing D_{t-m} then gives a measure RI of how much that mode contributes:

$$RI = 100\% \left(1 - \frac{D_{t-m}}{D_t}\right) \tag{8.5}$$

These do not add up to 100%, but show how much of the total response is lost if the mode is removed. Results for both gate designs are plotted in Figure 8.10.

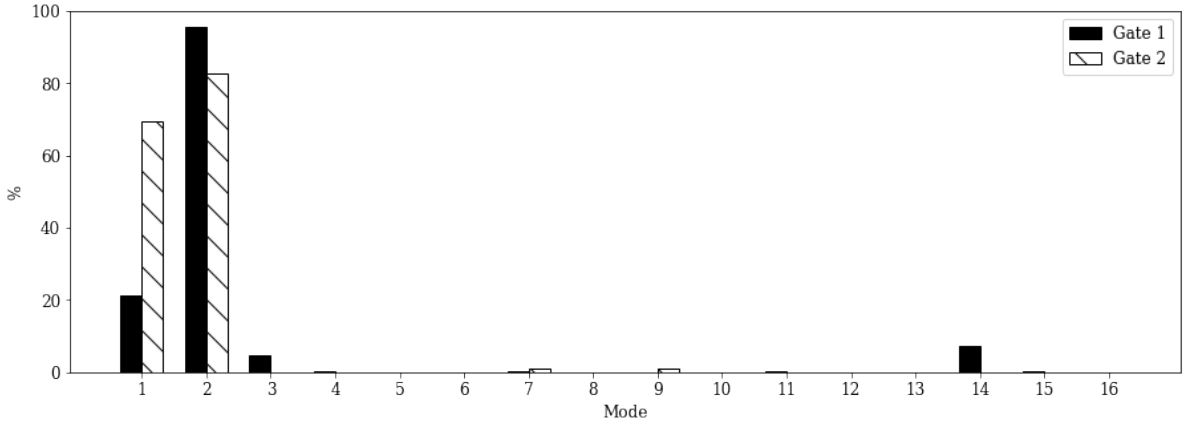

Figure 8.10: Relative importance RI of all modes at (x=5;y=L_{web};z=7.5).

This clearly shows that the second mode is by far the most important for the overall fatigue at the design

coordinate for Gate 1, followed by mode 1 and small contributions from modes 3 and 14. The fatigue of Gate 2 on the other hand can almost completely described by the first two modes, where the second is only slightly more important.

8.4. Fatigue accumulation over lifetime

Having gained insight into the fatigue across the gates and at the determined design coordinates for a single load event, the accumulated fatigue of the gates over their entire lifetime will now be calculated. For the purpose of this case study the gates will be designed to last 80 years. The representative boundary conditions which describe the projected wave climate over this period of time as determined in Chapter 7 will be applied to the fluid-structure system, and turned into a fatigue damage contribution at the critical point (x=5;y=L_{web};z=7.5). The Monte Carlo simulations are plotted in Figures 8.11-8.12.

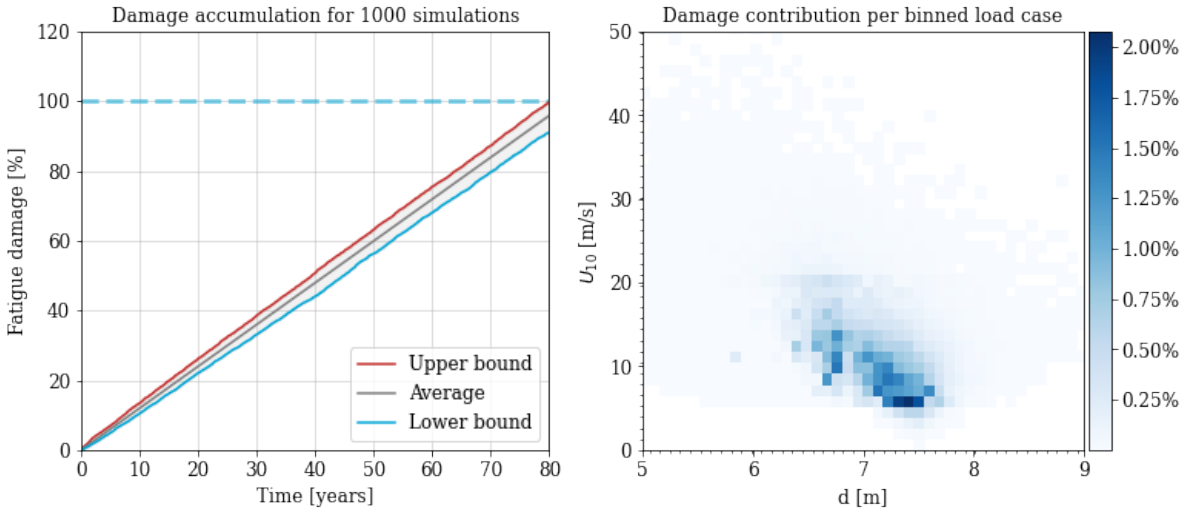

Figure 8.11: Monte Carlo simulation of the lifetime fatigue for Gate 1, and the relative contribution of the different load events.

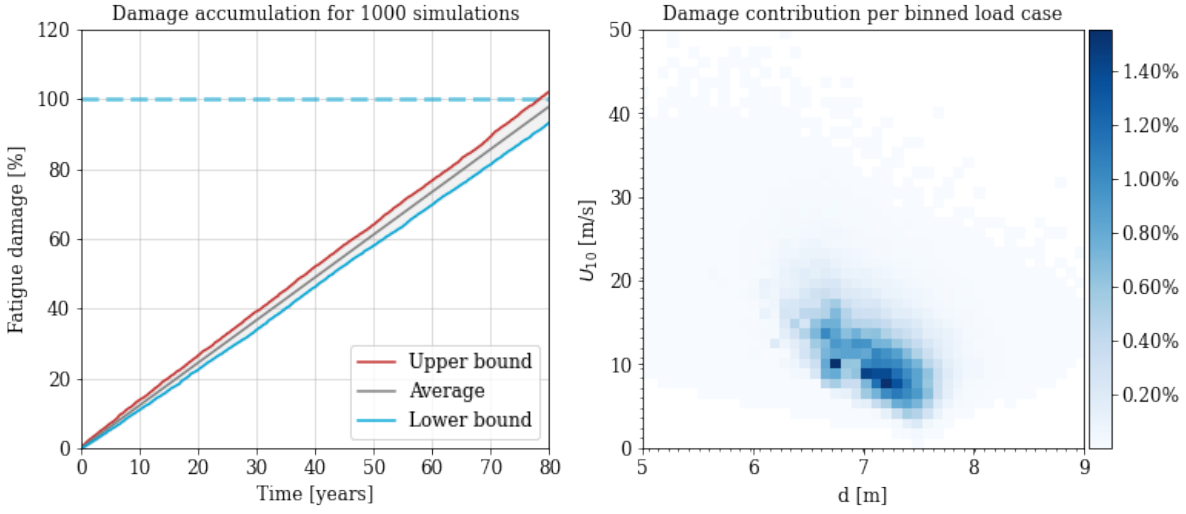

Figure 8.12: Monte Carlo simulation of the lifetime fatigue for Gate 2, and the relative contribution of the different load events.

The 95th percentile is at 95.88% and 99.9% of the fatigue capacity for gates 1 and 2 respectively, which means that both are sufficient. On the right the relative importance of the load combinations over the course of the lifetime is plotted. As previously established in Section 7.3 most of the damage is concentrated around relatively common (but not negligible) load events. A simple extrapolation can be used to estimate the expected lifetime for both: $\frac{80}{95.88\%} \approx 83.4$ years and $\frac{80}{99.9\%} \approx 80.1$ years.

The amount of steel needed to construct the gate can serve as a stand-in for its cost, so by comparing the masses of the designs an estimate of their relative efficiency can be found.
The results are shown in Table 8.3 and as expected Gate 1 is more efficient both in absolute mass and in amount of kg steel is required per year of lifetime. This comparison is mainly useful for designs where the difference in efficiency is less obvious.

	Mass		Longevity		Efficiency	
Type	Value	Unit	Value	Unit	Value	Unit
Gate 1	$70.9 \cdot 10^3$	kg	83.4	year	850	kg/year
Gate 2	$129.7 \cdot 10^3$	kg	80.1	year	1,619	kg/year

Table 8.3: Material efficiency of two designs.

8.5. Ultimate limit state

A probabilistic ULS check can also be performed to confirm the validity of the chosen gate design (Gate 1). Because fatigue is usually normative and the shallow depth of the Waddenzee limits how extreme the loads can get, the design is expected to be sufficient. It should also be noted that the method described in this report does not consider the plastic capacity of the material, which could be taken into account for a real ULS check. A once per 10,000 year wind load situation is derived from the probabilistic boundary conditions derived in Section 7.1.3, and applied 1000 times to check how often it fails. The design load case is a water depth of 7.5m (overhang level) and a wind velocity of 56.94m/s ($H_s = 3.94m$). To determine the probability of occurrence of this water level a range has to be chosen. If the load case resolution of 0.1m from Section 7.2 is used, the probability of occurrence is a little less than 1/1000 years. The combined independent probability of occurrence of these two circumstances is therefore approximately 10^{-7} per year. The peak stresses measured in Gate 1 for each simulated time series are plotted in Figure 8.13.

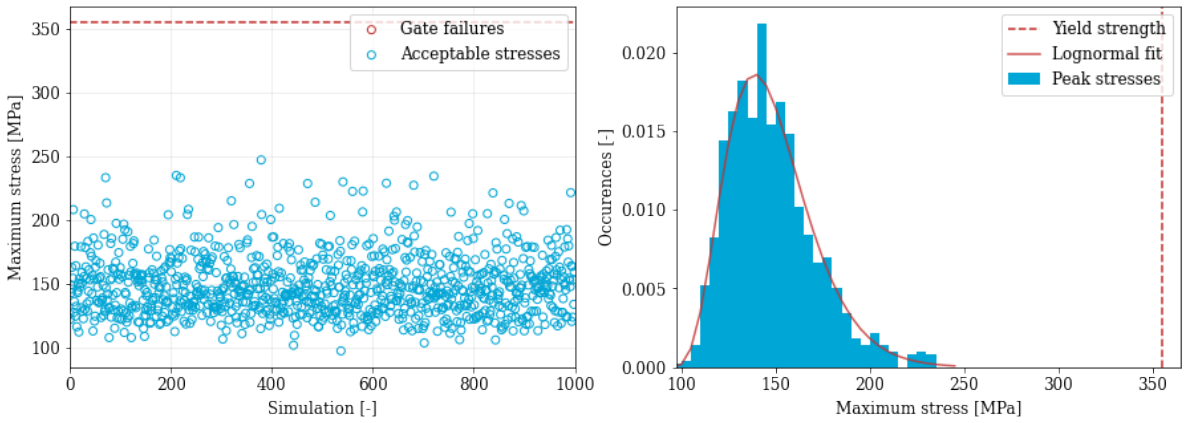

Figure 8.13: Individual 1/10,000 year load events plotted on the left; probability distribution on the right.

The gate fails in none of the simulations. A probability of failure can nevertheless be estimated by fitting a probability distribution to the outcome, as shown on the right. The probability that a given peak stress s_i exceeds the yield strength $f_{yd} = 355$ MPa is given by:

$$p(s > f_{yd}) = 1 - F_s(f_{yd}) \tag{8.6}$$

Where F_s is the cumulative density function associated with the results. This gives a failure rate of around 10^{-7} during the chosen design conditions, which is more than sufficient.

8.6. Climate scenarios

In the case study the extreme climate scenario of +1m sea level rise by 2100 was used, which is the most extreme IPCC estimate. But because a higher water level means that more wave impacts are likely to occur these scenarios have a large effect on the expected fatigue lifetime of the structure. It is therefore worth

briefly investigating how the outcome changes if a different one is picked. The results for a range of scenarios between +0.5m to +1.5m is plotted in Figure 8.14:

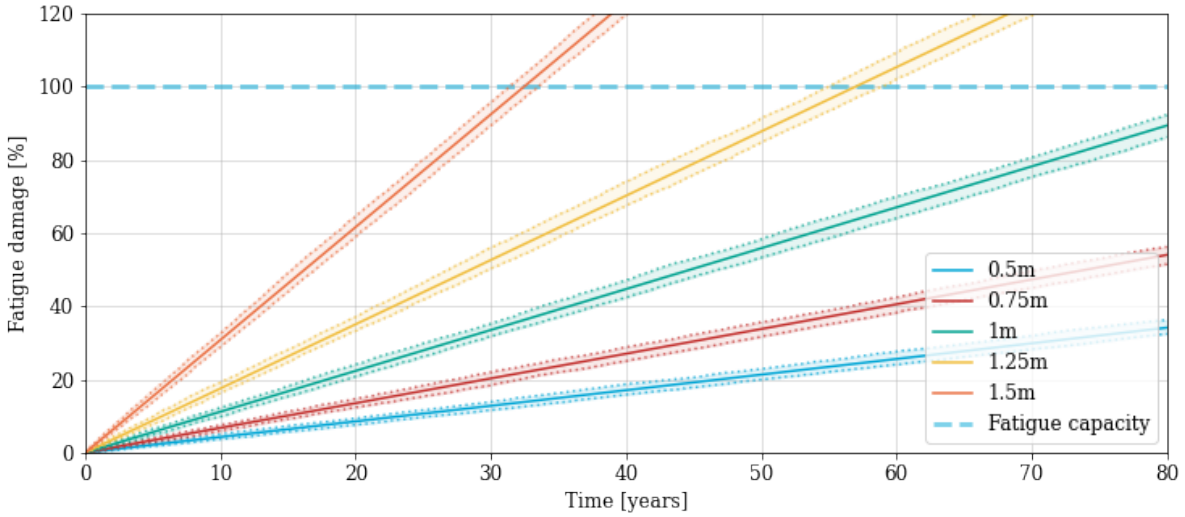

Figure 8.14: Development of cumulative fatigue over the lifetime of the structure for different climate scenarios.

The average projected lifetime of these scenarios is given in Table 8.4.

Scenario	Projected lifetime
+0.50m	293 years
+0.75m	185 years
+1.00m	112 years
+1.25m	71 years
+1.50m	41 years

Table 8.4: Expected lifetime for different climate scenarios

It shows that the fatigue damage keeps increasing for more intense climate change scenarios, but this is not true for all systems. A structure whose average water level is close to the overhang level will likely see the fatigue damage reduce with sea level rise, because the drowned channel will experience fewer wave impacts. This dependence on the difference between the water level and the overhang level was also noted in Figure 6.8. To test this hypothesis the average water depth was raised to 7m (from 5m), with the overhang level still at 7.5m:

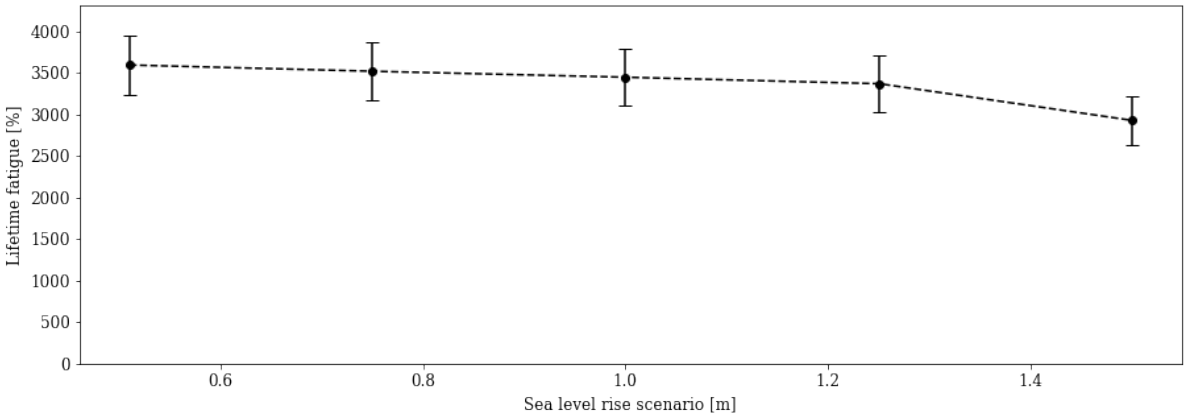

Figure 8.15: Fatigue for different climate change scenarios when the average depth is 7m.

As expected, in this case climate change has a positive effect on the lifetime of the structure. In cases where

the gate is almost completely submerged the lowest sea level rise scenario should therefore be taken as normative.

8.6.1. Influence of damping

The damping ratio of the gate-fluid system has been assumed at 2% in Section 5.4, but due to the significant importance of this parameter it is worth analysing how it affects the final outcome. At lower damping parameters the gate will damp out less quickly in between wave impacts, which besides causing stronger reverberations also means successive impacts can start reinforcing each other. The lifetime fatigue simulation is run thrice for different damping ratios. The result is plotted in Figure 8.16:

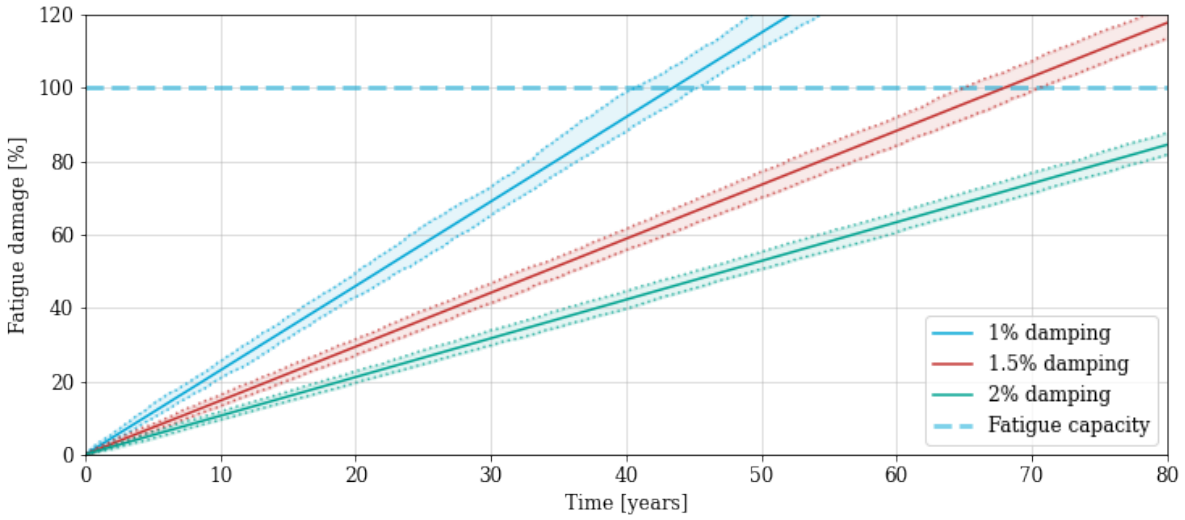

Figure 8.16: Lifetime Monte Carlo simulations for different damping ratios.

At a damping ratio of 1.5% the lifetime fatigue D_L increases by 40% to $D_L = 120\%$ of the capacity, causing the gate to fail. It is therefore very important that this parameter is defined well for the gate under consideration, and more research into an accurate way to determine it for structures like this will be one of the recommendations.

8.7. Comparison with alternative wave counting method

The spectral method described in Chapter 3 stochastically creates waves from an energy density spectrum with a random phase. In practice however, waves are commonly defined and evaluated individually and applied to the structure as many times as they are statistically expected to occur. This method, briefly introduced in Chapter 3, will be compared with the one described in the report. After establishing a significant wave height H_{m0} for the storm under consideration a probability distribution for the wave heights of individual waves can be found with Equation 3.1. This distribution is then simplified into a discrete set of waves, each of which is evaluated individually (see Figure 3.1).
For both the spectral method and the wave counting method the semi-analytic response method will be used to ensure the wave input is the only thing differentiating the two simulations.
As an example, a load event with $U_{10} = 20$m/s and $h_S = 7.5$m will be considered. The spectrum generated for this simulation has a significant wave height H_{m0} equal to [14]:

$$H_{m0} = 4\sqrt{m_0}, \qquad \text{where: } m_0 = \int_0^\infty \frac{S_{a,r}(f)^2}{2\Delta f} df \tag{8.7}$$

Equation 3.1 can then be used to create a probability distribution which is in turn discretized into 50 representative wave heights, as shown in Figure 8.17.
Each of these wave states has a characteristic wave height H_i which is the mean of the range it represents and a probability of occurrence $p(H_i)$ equal to the integral of the area under the curve ($p(H_i < H < H_{i+1})$). The total amount of waves expected to occur during the load case with duration T_L can be calculated from the spectrum with Equation 8.8 [14]:

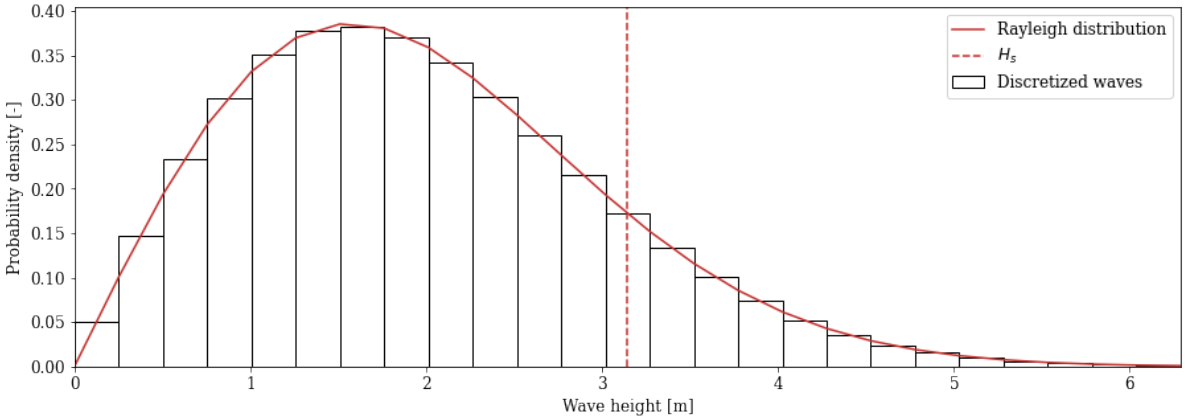

Figure 8.17: Continuous and discretized probability density of wave heights for $U_{10} = 25$m/s.

$$N_{tot} = T_L \cdot \sqrt{\frac{m_2}{m_0}} \tag{8.8}$$

The derivation of the spectral area moments m_n is described in Equation 3.18. The number of times each of the discretized waves is expected to occur follows from:

$$N_i = p(H_i) \cdot N_{tot} \tag{8.9}$$

Before proceeding, the amount of waves and their distribution is compared to those found from the spectrum to make sure they are comparable up to this point. Figure 8.18 shows a very similar distribution and besides some statistical variance the number of waves predicted by Equation 8.8 is equal to the number of waves found in random realisations of the spectrum ($N_{tot} \approx 863$ for $U_{10} = 20$m/s and $h_S = 7.5$m).

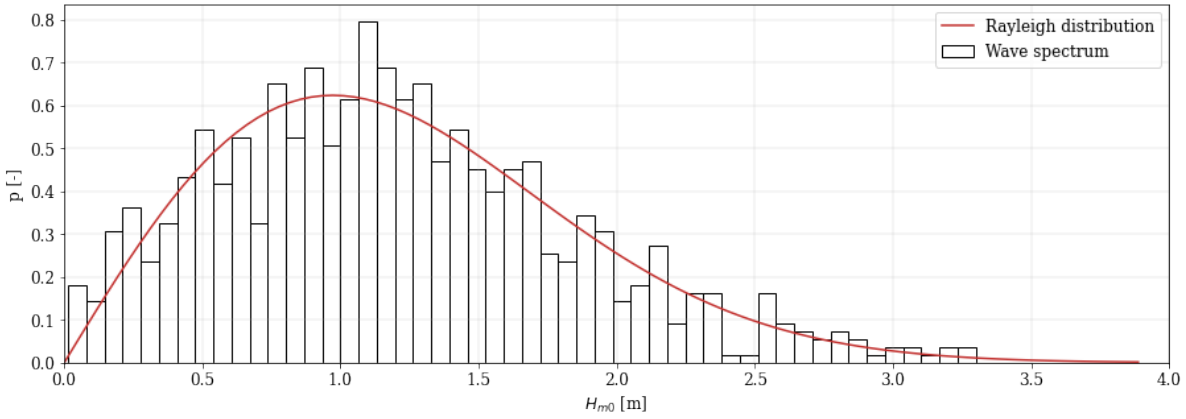

Figure 8.18: Theoretical probability distribution of wave heights and wave heights found in random realisation of spectrum.

Now all that remains is to compute the fatigue damage D_i associated with each of these wave states. A time series of the wave pressure will be created in the same way as in Section 4.2, except that the upward water surface velocity in Eq. 4.11 can't be obtained from the derivative of a water level time series in this case. According to linear wave theory the amplitude of the vertical velocity of water is given by [14]:

$$U_{w,i}(z,t) = \omega_i \frac{H_i}{2} \frac{\sinh k(z+h)}{\sinh kh} \sin(\theta) \tag{8.10}$$

Because the impact always occurs at the surface level $z = 0$ and an up-crossing where $\theta = 0$, this simplifies to:

$$U_{w,i} = \omega_i \frac{H_i}{2} \tag{8.11}$$

where $\omega = \frac{2\pi}{T}$. The wave period is a stochastic variable in reality, but as an approximation the average wave period $T_{m02} = \sqrt{\frac{m_0}{m_2}}$ is used [14]. This parameter has a large influence on the result but is not easy to define for individual wave states, because the values m_0 and m_2 relate to the spectrum rather than wave heights. Therefore two approximations will be used for the comparison. One relies on the range of empirical estimates and the other is derived by fitting a line through the results of a wide range of spectra. Empirical relations generally find the average wave period to be somewhere between $T_p/1.5$ and $T_p/2$ [21], where $T_p = 5\sqrt{(H_{m0})}$. Both of these will be evaluated to serve as a range between which the true values should be. In addition a list of spectra will be generated for a range of wind velocities, after which the ratio of H_{m0} to T_{m02} is determined and used to fit a line. Figure 8.19 shows graphs of these three $H_{m0} - T_{m02}$-relations.

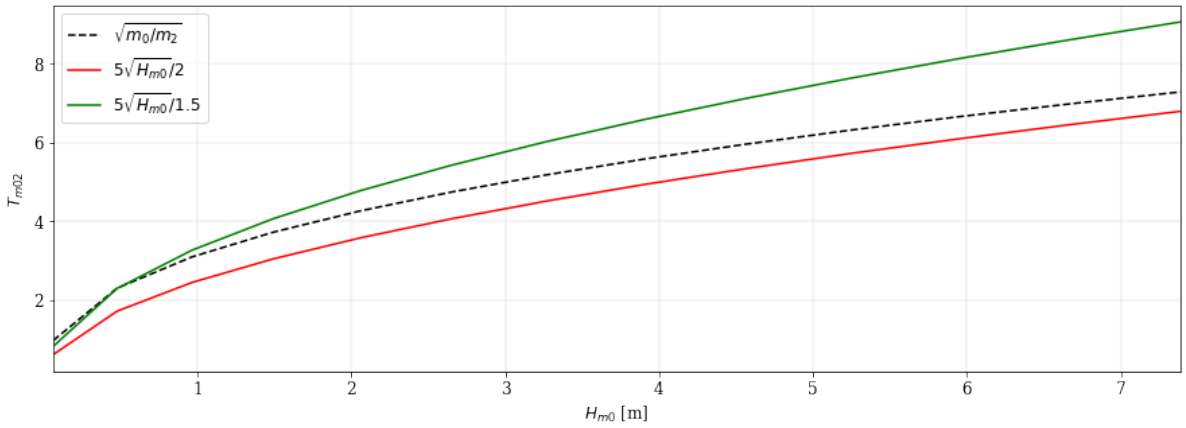

Figure 8.19: Average wave period T_{m02} according to three different definitions.

These relations will be used to derive a representative impact velocity $U_{w,i}$ for each of the representative wave states H_i with Equation 8.11. The resulting distributions of the impact velocity are plotted in Figure 8.20, along with the impact velocities observed in the random realisation of the wave spectrum.

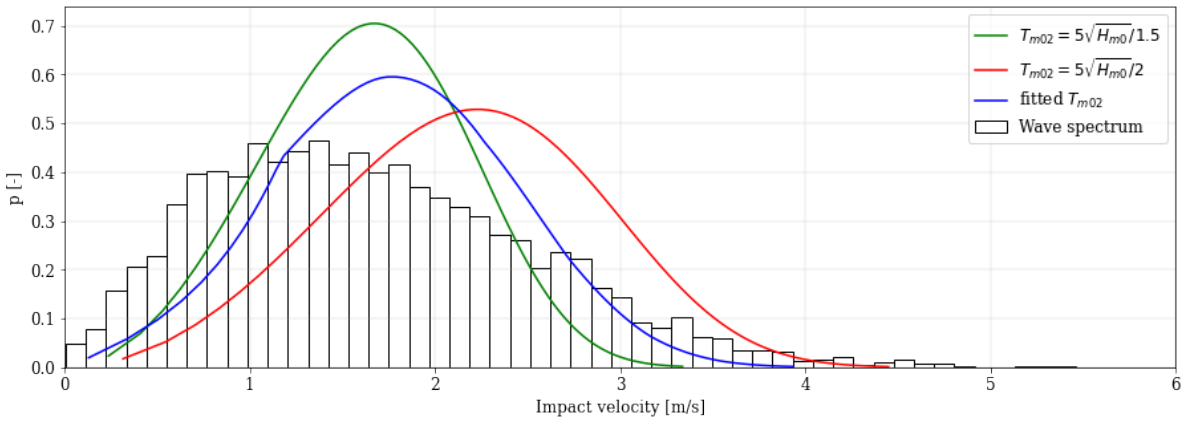

Figure 8.20: Probability comparison of impact velocities from signal generated from spectrum and individual waves.

Unlike the wave heights a significant difference between the approximate and observed impact velocities can be observed here. The impact velocities found in the random realisation of the wave spectrum have a wider distribution that skews to the left, because rather than being neatly separated waves the velocity of the surface level elevation follows from a superposition of all the different wave harmonics. The effect of this difference on the fatigue damage will be determined next.
The values variables β_{im} and τ are probabilistic, but for the fatigue damage comparison they will be fixed at 1 and 0.1 respectively. Furthermore the quasi-static wave fluctuation pressures are ignored in all simulations. After substituting the values for $U_{w,i}$, β_{im}, and τ into Equations 4.11 and 4.13, a time series with a single force impact is obtained. The effect of the different wave period approximations is shown in Figure 8.21.

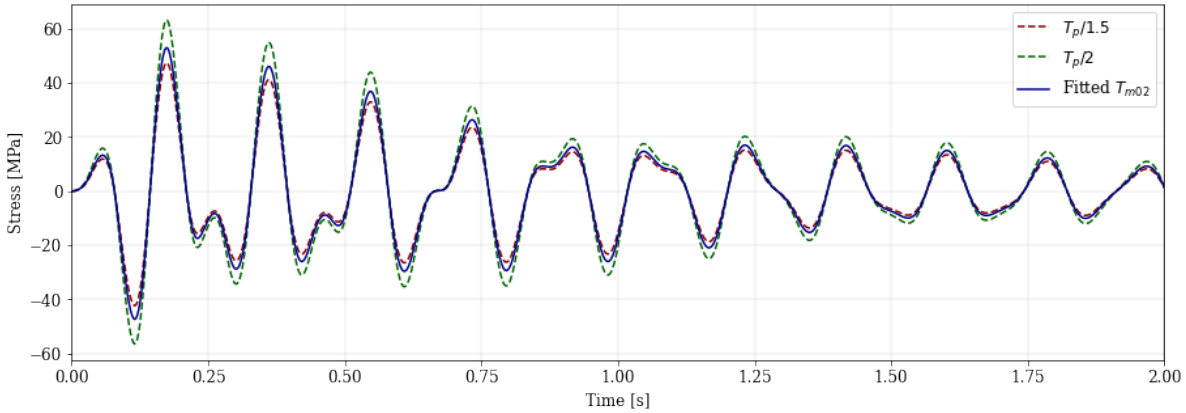

Figure 8.21: Stress response of identical wave for different approximations of T_{m02}.

Each individual wave impact is given 15 seconds to damp out (sufficient for 2% damping and forcings of this magnitude). A pressure spectrum is then obtained with the steps described in Section 4.2. This spectrum is evaluated with the methods described in Chapters 5 and 6, to find the fatigue damage factor D_i for each wave.
Now the fatigue damage factor D_i and number of occurrences N_i are know for each wave, for three different wave period approximations. The total fatigue damage contribution of a representative wave state is then given by:

$$D_{t,i} = D_i \cdot N_i \tag{8.12}$$

The total fatigue damage for the considered load event is then found by summing all the contributions of the representative waves:

$$D_t = \sum^{N} D_{t_i} \tag{8.13}$$

The same random realisation of the spectrum of that load case is then evaluated with the method from the main report. Another effect which differentiates the spectral method from the one described above is that it accounts for wave train effects, meaning that consecutive waves can reinforce each other (or cancel each other out). To isolate the significance of that effect as well, the wave impacts observed in the spectrum are also evaluated separately without combining them into a single time series. This eliminates that effect while keeping the rest of the method the same. Overall this means that the fatigue for the same load event was calculated in 5 different ways, the results of which are summarised below in Table 8.5. Each result is the average of 10 simulations to account for natural variance.

Method	Fatigue damage	Normalised
Spectrum with combined time series	$6.3 \cdot 10^{-4}$	1
Spectrum with isolated wave impacts	$5.4 \cdot 10^{-4}$	0.87
Wave counting with fitted T_{m02}	$6.0 \cdot 10^{-4}$	0.96
Wave counting with empirical limit $T_p/1.5$	$4.2 \cdot 10^{-4}$	0.67
Wave counting with empirical limit $T_p/2$	$11.7 \cdot 10^{-4}$	1.87

Table 8.5: Fatigue damage for $U_{10} = 20$m/s and $h_S = 7.5$m according to 5 different methods.

The rightmost column shows the values normalised to the simulation where the wave impact velocities are derived from the spectrum according to the method described in Chapter 5.28. It is found that the this spectral method gives a higher result than the simulation where each wave impact from the spectrum is evaluated in isolation, which suggests that waves reinforcing each other is a significant effect. Even though in theory the amount of negative and positive reinforcement should be equal, the nonlinear nature of fatigue makes it so that the positive reinforcement outweighs the negative. As expected the two empirical boundary values are respectively much higher and lower than the other methods. The fitted values of T_{m02} approximate the result of the full spectral method to within 4% even though in theory it should approach the spectral isolated wave impact method, which has a lower result.

8.8. Comparison with single-mode system

The semi-analytic method from Section 5.3 has so far been applied for 16 modes, of which the second has been found to be very important due the asymmetric wave impact shape. In practice these system are often simplified to a single mass-spring system which only takes the first mode into account. The difference between such a single-mode model and the version with a larger number of modes will be compared in this section.

First, the difference in response to singular waves will be compared. Next, full storm events will be simulated and finally the fatigue lifetime will be calculated at the respective critical locations for both models. During this comparison the amount of modes will be the only thing differentiating the two models.

The frequency response function (FRF) from Equation 5.33 for the only response mode of the system is shown in Figure 8.22.

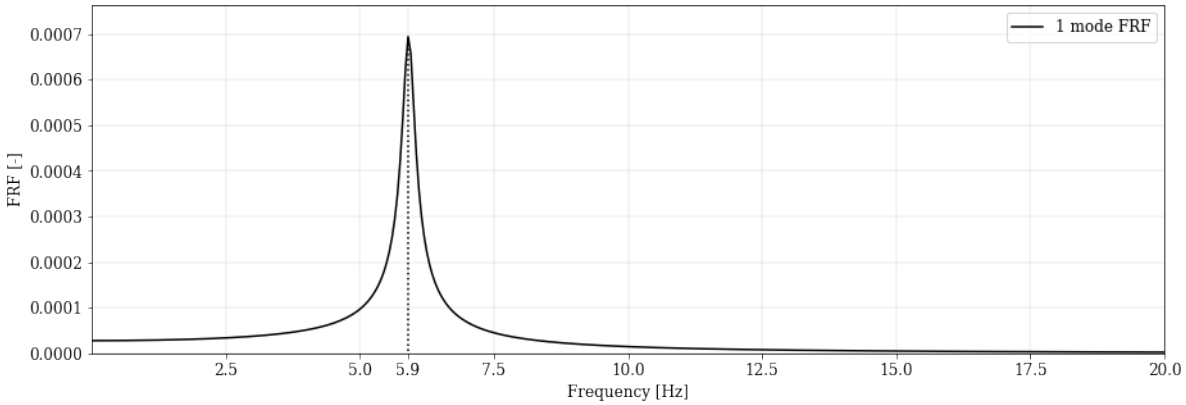

Figure 8.22: Frequency response function of Gate 1 for only the first mode.

The force $q_{ij}(f)$ for a single wave impact is determined with Equations 4.11 through 4.13 with an impact velocity U_w from Equation 8.11. The responses to a wave height H of 0.8m and a wave period T of 1.6s for both the upper and lower limit of the impact duration distribution (τ = 0.01s and τ = 0.2s) are plotted in Figure 8.23.

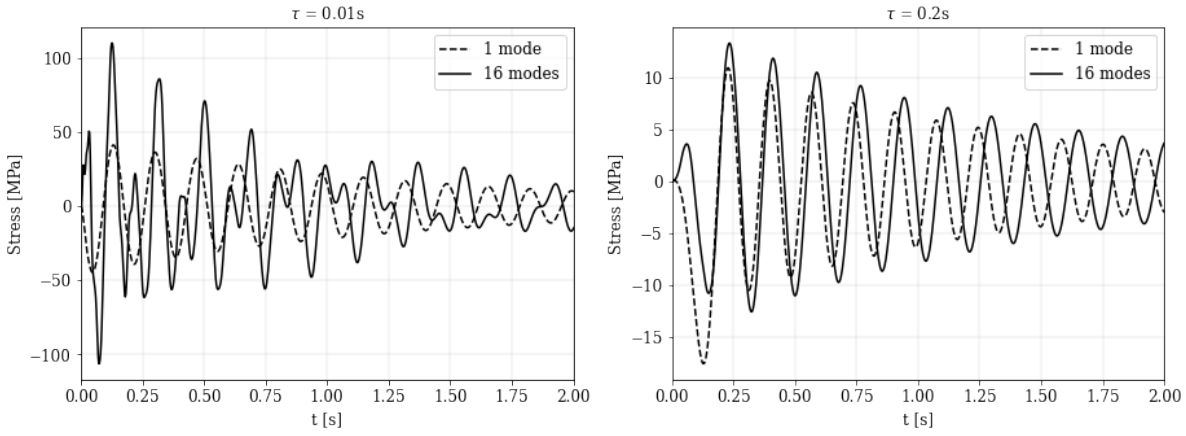

Figure 8.23: Comparison of response for 1 and 16 modes, for τ = 0.01s and τ = 0.2s.

It can be seen how for the shorter impact duration the second mode is mobilised more strongly, whereas for longer impacts the response is of a similar magnitude. Wave spectra contain impacts with durations ranging between these values, so the fatigue is computed at some selected coordinates for all possible impact durations for both the model with 16 modes and the version with just 1, and divided to obtain their ratio. The ratio for each value of τ is plotted in Figure 8.24, to show the relative strength of the fatigue response for the two models. The coordinates that will be considered are:

- (5; 0.71; 7.5), the critical coordinate of the gate design

- (5; 0.71; 2.55), the coordinate where the first mode is dominant
- (5; 0.71; 5), a reference coordinate where the contribution of the first mode is average

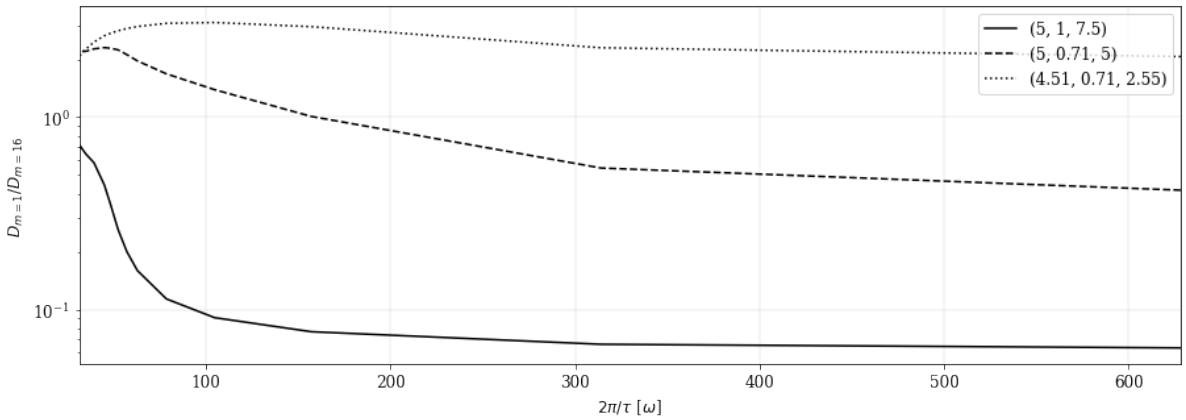

Figure 8.24: Ratio between fatigue damage factors for 1 and 16 modes at different impact durations τ.

The differences between the effect of including higher modes for these coordinates is significant. It was previously established that the second mode is dominant at the critical coordinate, and this is confirmed here as the result for the single-mode system is more than ten times lower for lower impact durations. This result agrees with the one found earlier in Figure 8.10, where removing the second mode alone decreases the fatigue at the critical point by more than 90%. Conversely, the coordinate where the first mode is dominant shows a higher response for all impact durations. The reference coordinate with a more balanced modal mobilisation is somewhere in between shows a lower result at higher frequencies and a higher result for lower ones.
A full wave spectrum will contain a combination of all of these impact durations, so the effect of including a different amount of modes on a random wave spectrum is evaluated next. A section of the time series of a random realisation of the stress response based on both 1 and 16 modes is plotted in Figure 8.25 for both the critical coordinate (5; 0.71; 7.5) and the coordinate where the first mode is dominant (5; 0.71; 2.55).

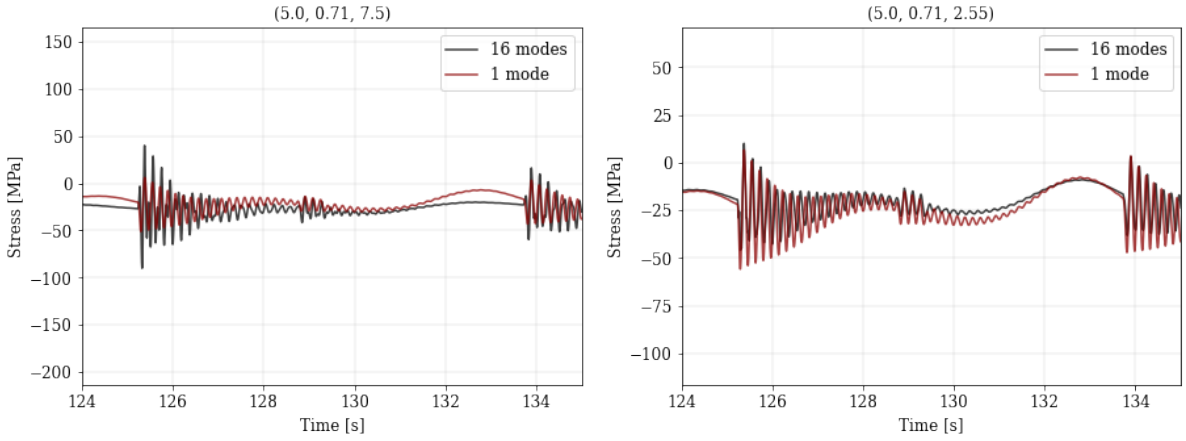

Figure 8.25: Left: Stress response for 1 and 16 modes at (5; 0.71; 7.5). Right: Stress response for 1 and 16 modes at (5; 0.71; 2.55)

Similar to what was found in Figure 8.24, the coordinate at the top of the gate loses much of its response in the single-mode system whereas the response at the coordinate where the first mode is dominant becomes stronger. This difference will also be noticeable in the fatigue at the critical point for a random realisation of the wave spectrum. The fatigue damage factors derived from identical load events with both the 16- and 1-mode model are shown in Table 8.6, and the distribution of fatigue across the gate for 1 and 16 modes are plotted in Figure 8.26:
As expected the model with 1 mode shows that the fatigue follows the shape of the first dry response mode (Figure 8.8), which gives very different results from the case with 16 modes where the asymmetric wave im-

Coordinate	Description	D_1	D_{16}	D_1/D_{16}
(5.00; 0.71; 7.50)	Critical coordinate	1.3×10^{-3}	2×10^{-4}	16%
(5.00; 0.71; 2.55)	First mode dominant	1×10^{-4}	2×10^{-4}	224%
(5.00; 0.71; 5.00)	Reference coordinate	2×10^{-4}	3×10^{-4}	131%

Table 8.6: Fatigue for 1 mode (D_1) and 16 modes (D_{16}) at different coordinates.

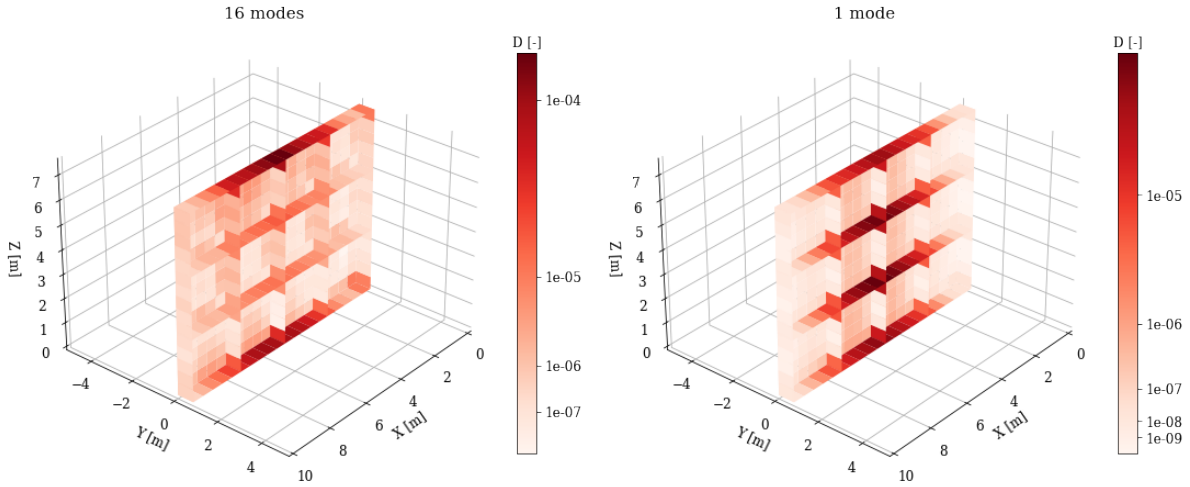

Figure 8.26: Fatigue over surface of Gate 1 evaluated with respectively 16 and 1 modes.

pact pressures are able to mobilise the higher modes. Table 8.6 shows that neither of the two models is conservative at all points in the gate simultaneously, but that including the higher modes does provide a more accurate response distribution and significantly higher fatigue requirements at the critical locations (almost an order of magnitude). For the remainder of the section, comparisons will be made between at the critical coordinates of both versions. These are (x=5; y=0.71; z=7.5) for the version with 16 modes and (x=5; y=0.71; z=2.55) for the version with 1 mode.
The maximum and mean stresses in both gates for a given one-hour load event at their respective critical coordinates are summarised in Table 8.7.

Coordinate	Modes	Peak stress	Normalized	Mean stress	Normalized
(5.00; 0.71; 7.50)	16	150 MPa	100%	27.5 MPa	100%
(5.00; 0.71; 2.55)	1	90 MPA	60%	23.6 MPa	85.8%

Table 8.7: Average stress characteristics for 50 simulations of a U_{10} = 20m/s, h_S = 7.5m load event at different coordinates.

The stresses are lower in the single-mode model for a few reasons: firstly in the version with 1 mode the stresses are distributed more evenly across the gate whereas in the 16-mode model they can concentrate (as seen in Figure 8.26). Secondly, the higher modes respond more strongly to shorter wave impacts, which cause the highest stresses (see Figure 8.25). Because fatigue scales logarithmically, this difference is further amplified.
For the final comparison a fatigue lifetime analysis is performed for both models at their respective critical coordinates. The results are plotted in Figure 8.27.
Compared to a 95th percentile result of 96% of the fatigue capacity for the version with 16 modes, the version with 1 mode only reaches 15%. This is in line with the ratio found in Figure 8.26 and represents a significant difference.

8.9. Influence of impact duration

Because the triangular impact duration distribution found in Section 4.2 has been found to be important for the strength of the response but not necessarily verified for the scale considered in this report, a sensitivity analysis is performed where the response to a range of impact durations is calculated and the effect of different distributions on the lifetime fatigue is compared.

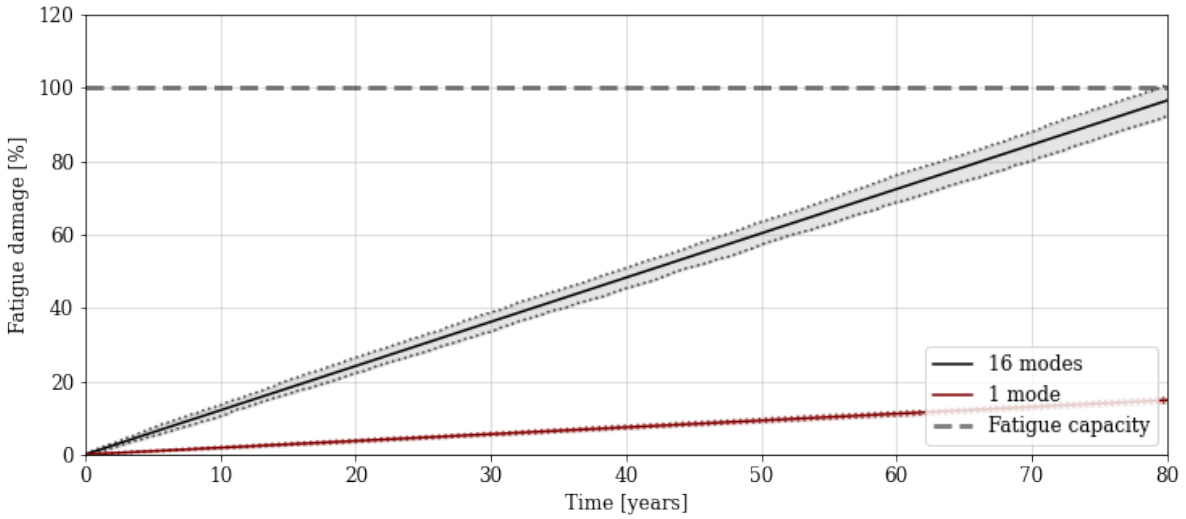

Figure 8.27: Accumulated fatigue damage over the lifetime of Gate 1, evaluated at the critical coordinates for 16 and 1 modes.

First, the response to a single wave is calculated for values of τ ranging from 0.0005s to 0.25s. The fatigue damage factors D are plotted in Figure 8.28.

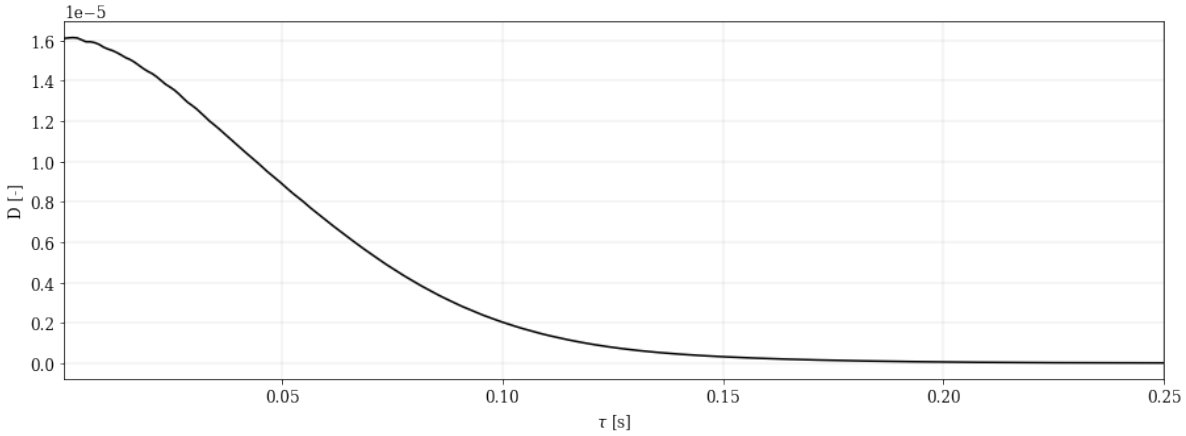

Figure 8.28: Fatigue for a single wave with different values of τ, H_{m0} = 1m, and T = 2s.

As expected shorter impact durations result in a stronger dynamic response and therefore more fatigue. Random realisations of the wave spectrum will contain waves all with random values of τ from a triangular distribution. The choice of distribution will therefore also have a large impact on the lifetime fatigue experienced by the structure. To show the effect of different distributions, simulations are run for a selection of distributions:

- (0.01; 0.105; 0.2), the distribution used in the report.
- (0.02; 0.105; 0.19), a narrower spread around the same statistical mode.
- (0.001; 0.105; 0.21), a wider spread around the same statistical mode.
- (0.02; 0.115; 0.215), entire distribution shifted towards longer wave impacts.
- (0.001; 0.095; 0.19), entire distribution shifted towards shorter wave impacts.

Where the three values stand for the lower limit, statistical mode, and upper limit of the triangular distribution. Besides the impact duration distributions everything is the same. The distributions are plotted in Figure 8.29 and the resulting lifetime fatigue graphs are plotted in Figure 8.30.
Because the lower impact durations cause most of the fatigue, the distributions which include more of them show a higher cumulative fatigue and vice versa. Even for the wider distribution the extra fatigue from the lower impact durations is not cancelled out by the fact that longer impacts also occur more often.

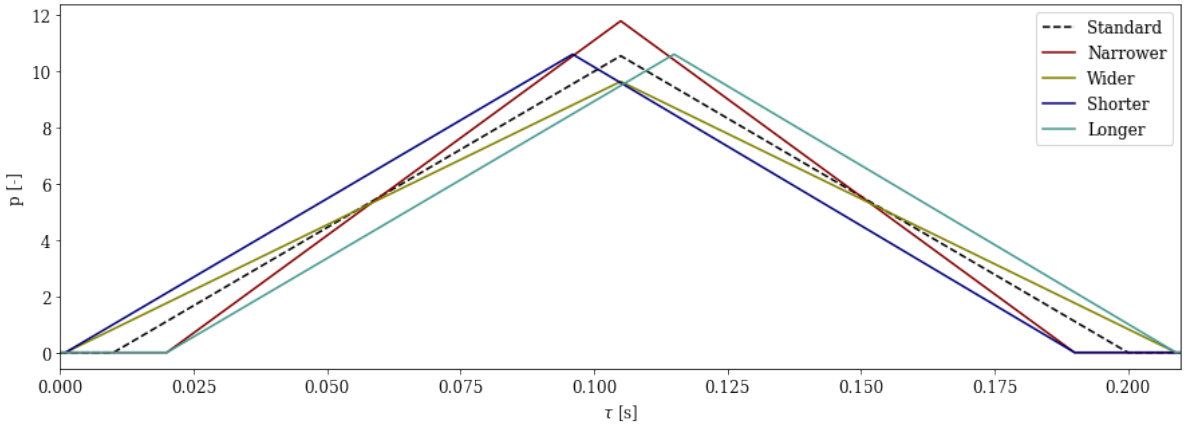

Figure 8.29: Different impact duration distributions applied in sensitivity analysis.

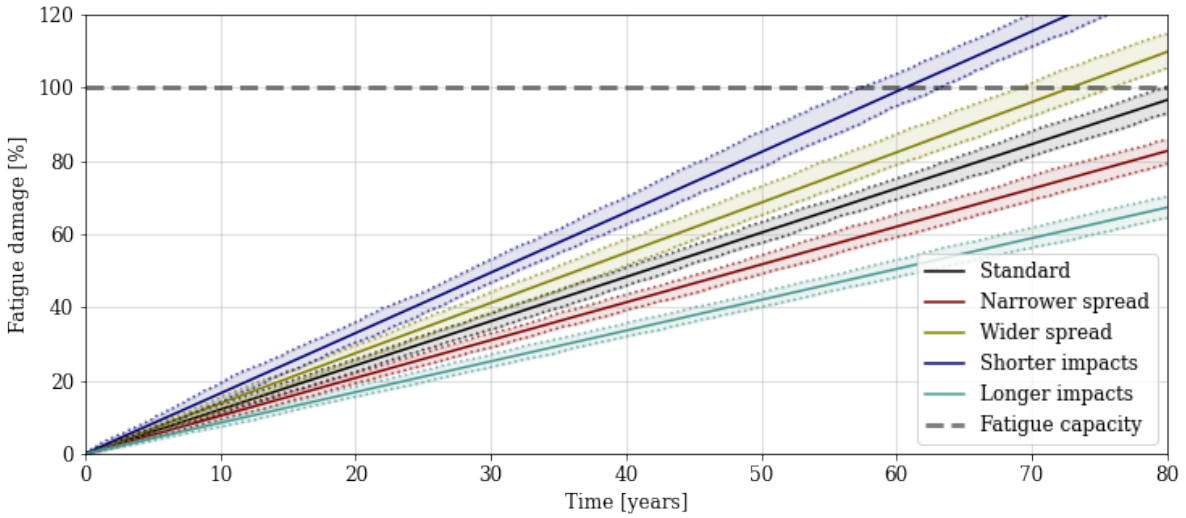

Figure 8.30: Lifetime fatigue damage development for different impact duration distributions.

Symbol	Description	Value	Unit
	Model settings		
n_m	Amount of considered modes	16	-
n_x	Subdivisions in x-direction	4	-
n_z	Subdivisions in z-direction	5	-
f_{max}	Highest analysis frequency	200	Hz
υ	Poisson's ratio	0.3	-
	Fatigue constants		
γ_{Mf}	Factor for fatigue strength	1.15	-
γ_{Ff}	Factor for fatigue loading	1	-

Table 8.8: Summary of parameters used for case study.

9

Conclusion and recommendations

The research questions and plan in Chapter 2 set out the goals of this project, and in the subsequent chapters 3-7 a method to realise them was formulated. In this final chapter the conclusions drawn from this process will be summarised, the applicability of the model delineated, and recommendations will be given for the most promising areas of further research.

9.1. Conclusion

The objective of this thesis was to formulate an integral framework which can accurately and efficiently compute the fatigue of flood gates under dynamic wave loading to a wide variety of boundary conditions. Adaptability was also important, which meant it should be possible to replace individual steps to better suit specific cases without the overall structure of the framework being affected. Along the way the applicability and uncertainties associated with the method also had to be quantified.
First, the model had to be split up into self-contained modules with defined in- and outputs, each of which takes care of one step in the process of transforming probabilistic boundary conditions into a lifetime fatigue assessment. Appropriate solutions were found for each of these steps, with suggestions for possible alternatives or improvements where possible.

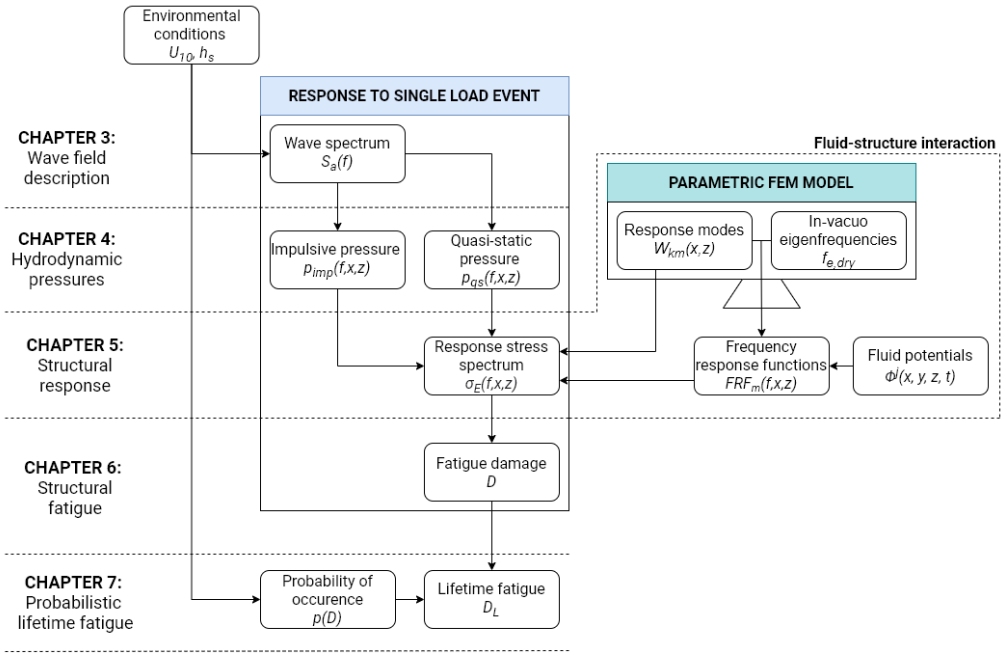

Figure 9.1: Structure of the framework.

The goal of the first set of modules was to solve the fatigue damage caused by a single load event.
Spectral methods offered an efficient way of doing this and were therefore employed throughout. With the wind velocity, site properties, and average water level as input a wave spectrum can be generated. It was found that a TMA-spectrum is most suitable for modelling locally generated wind waves in shallow seas. With the help of established wave pressure theories these were used to generate separate quasi-static and impulsive pressure spectra for short overhangs.
These wave spectra were then evaluated with a mode matching method coupled with a parametrically defined finite element model of a gate, which efficiently computes the modal response of the fluid-structure system. The level of accuracy can be changed to match the design stage; for an exploratory design a very coarse model can be coupled but the method works equally well for complex ones. Conventional Eurocode checks or more efficient spectral methods can then be used to turn the resulting response spectra into a fatigue damage factor, which shows how much of the structure's fatigue capacity is used by a specific load event. It was found that the standard time domain method is most suitable for this purpose, though spectral methods can be used to speed up the computation.
This response calculation is combined with a joint probability density function of the boundary conditions, based on a best fit of historical data. Historical water level data was used to derive wave spectra to describe short-term fluctuations and represent various combinations of long term fluctuations like tides as hourly averages. It was found that these long-term fluctuations do not cause significant stress cycles in most cases. After the joint probability function was integrated into discrete load cases characterised by their average values and a probability of occurrence, a manageable set of load events was found which can be evaluated in an acceptable time-frame. The resolution of this discretization process was based on the marginal effect of further refinement on the variance of the fatigue outcomes. In addition, two filters based on the strength and frequency of the load cases are applied to further reduce the amount of load cases. Each case is then evaluated with the previously described fatigue model, after which a Monte Carlo analysis can be run on the resulting fatigue damage factors and their associated probabilities. 1000 full lifetimes are simulated to obtain a probabilistic estimate of the structural fatigue lifetime. This 95th percentile of this estimate was found to be roughly 4% above the average for a lifetime of 80 years and a standard deviation of 20% for the fatigue of individual load events.
A case study was performed to demonstrate how the method can be applied and how different parameters affect the response. Two preliminary designs were verified and compared. Analysis of the lifetime fatigue result showed that common events of intermediate strength are the most important for the cumulative fatigue damage because water levels higher than the overhang level result in a lower response and the shallow depth limits how high waves can become. The response can be split up by mode to see which are most important for the total fatigue, and both a design with a very thick gate and a design with large stiffeners showed that the second mode has a dominant role in the response for systems of this type. The importance of including these higher order effects was further confirmed by a comparison with a single-mode version of the same model in Section 8.8, which showed that the latter method gives much lower critical fatigue values. Furthermore the model was used to perform a ULS check to confirm the validity of the chosen design.
A comparison was made between the response obtained from a wave spectrum and the response of the same wave state when calculated with a conventional method where the individual waves are derived from a Rayleigh distribution. It was found that whether the wave counting method is conservative depends on the values chosen for T_{m02}, but that all things being equal calculating the response to all the waves separately does give a lower result than evaluating the full spectrum. This is hypothesised to be a result of the fact that consecutive waves can't reinforce each other in the wave counting method.
The method gives insight into the relative importance of different modes and load events, can compute fatigue for the entire gate or just a critical coordinate, and does so in a much more time-efficient manner than current numerical models. Plotting the fatigue over the entire gate surface shows where material can be added or removed to make the design more efficient. It gives a more comprehensive view of the fatigue over the lifetime of the gate by modelling its entire lifespan rather than a set of design load events.

9.2. Applicability

Throughout the report different tools, theories, and models have been employed, each of which comes with limitations. This constrains the applicability of the overall method within those boundaries, and during application it should be confirmed whether the situation under consideration satisfies them. If not, the modular nature of the method generally means one part can be swapped out for another. In this section these con-

straints and their possible alternatives will be briefly recapped. Table 9.1 gives an overview of the limitations.

Chapter	Module	Limitations and simplifications
3	Wave spectra	• JONSWAP is only applicable in deep waters. TMA extends this to shallow seas but both are calibrated for the North Sea wave climate. If the project site is governed by a different spectrum it can be swapped out. • Sea states are assumed to be fully developed. • The spectrum describes non-steep waves. For non-linear effects Stokes theory should be applied. • Spectral components not generated by local wind (such as swell) have not been considered but can be added to the spectrum. • The approach angle was simplified to always be perpendicular.
4	Pressures	• Pressures are modelled as uniform across the width. • For Wood-Peregrine wave impact pressures: – Long wavelengths relative to overhang size ($L_{wave} > 10L_y$). – Low steepness waves ($0.023 < s < 0.042$). – No wave breaking at structure. – No gap between overhang and gate. • The probabilistic impact duration is derived from small scale experiments and not verified for full scale structures. • The reflection coefficient was estimated but could be more complex (e.g. variable based on wave height due to interaction with the overhang) • Linear wave theory for quasi-static pressures does not hold for non-linear waves.
5	Gate response	• Response is computed elastically; no plastic deformation. • Stress-free surface and no radiation damping ($\frac{\omega^2 h}{g} > 10$). • Frequency-independent 2% material damping was assumed; true values will be variable and somewhere between 1-3%. • Constant water level during reverberation. • Inviscid and compressible fluid. • Wave impacts are modelled as independent excitation forces, not altered by the response of the fluid-structure system. • The FEM model used in the case study is simplified to basic geometry, but the method also works for more complex structures.
6	Fatigue	• Only implemented for principal stresses in parent material. • Spectral method only valid for broad-banded spectra. • Fatigue sources besides wave loading were not considered (e.g. due to operation).
7	Probabilistic boundary conditions	• Only hydraulic loads considered; no wind or operating-related stresses. • Requires historical data at site location. • Probability density functions assume independence. • Very simplified bathymetry of Waddenzee. • Wind velocity probabilities assumed stationary over time. • Deterministic climate scenario rather than full probabilistic analysis. • Stress cycles from tides and other long-term fluctuations are all below the fatigue cut-off limit.

Table 9.1: Assumptions and limitations.

Some improvements to the wave spectrum-, response-, and fatigue calculations have already been suggested in the relevant chapters. Some are more demanding than others; expanding the model for more complex gate geometries or welds for example would simply be a matter of creating a more detailed model. Others require additional theory or research. If the model has to be re-purposed for a system without an overhang but with wave breaking for example, the impulsive wave theory from Chapter 4 should be replaced with one which accounts for it. A more in-depth boundary condition model can be substituted for the relatively simple fitting procedure described in Section 7.1.3 without altering the discretisation method and subsequent calculations. Some changes will have ramifications across multiple modules however; adding dependence on the angle of approach would require an additional probabilistic boundary condition, a directional wave spectrum, and non-uniform pressures over the gate width. Everything from the response calculation onward would remain unaffected.

9.3. Recommendations

While the modular nature of the method means any part of it allows for further refinement or generalisation and a lot of options have already been discussed in the text, some areas offer particularly promising possibilities for improvement.

9.3.1. Damping

The damping of the system is still subject to a lot of uncertainty. Conservative values have been applied in this thesis because the contribution of the added water mass to damping was found to be negligible in Section 8.6.1, but because the effect of damping on the result is so large (See Figure 8.16) it can be of great value to get an improved estimate with from either practical experiments or more in-depth theoretical modelling of damping in fluid-structure systems.

9.3.2. Short waves

The current version is limited to long waves or, equivalently, short overhangs ($L_y < 10L_{wave}$). It was shown in Section 4.2.1 that this is not a major problem for the overhang size chosen in this report, but for a more generally applicable model the wave impact forces should be determined in a way which does not have the constraints of the current Wood & Peregrine pressure-impulse theory (Section 4.2).

9.3.3. Wave impact duration

The impact duration was shown to have an important effect on the stresses and therefore fatigue in Section 8.9, but is based on small-scale tests that don't necessarily scale well to larger structures. A more robust schematisation of the impact duration distribution could be obtained from either large scale tests or numerical simulations.

9.3.4. Oblique wave impacts

In reality waves will not all hit the structure head-on, but approach from a range of angles. The interference, local pressure variations, and hydrodynamic effects caused by this more general model could have a significant effect. Unlike other improvements this would require multiple modules to be changed:
- The load events would have to include the angle of approach as another dimension in addition to the wind velocity and average water depth.
- The pressure computation has to account for pressure differences over the width and local pressure spikes due to partial wave impacts.
- The fluid-structure interaction model is built on the assumption that the water level is constant and uniform across the width. Whether this is still valid for a situation with significant water level differences across the width should be confirmed.

For gates in a channel, like the one considered in the case study, this is unlikely to make a very significant difference, but for gates located right next to a large, deep body of water where refraction isn't as strong this could be important for a more comprehensive result.

Appendices

A

Python code

This appendix will briefly summarise relevant information about the Python code used to run the calculations and analyses described in the report. Printouts of most important Python scripts are also included. Software required to run the model are SCIA Engineer 19.1, Jupyter Notebook, and Python.
First, a short list of performance benchmarks for a laptop with 16GB RAM and an i7-7700HQ 2.8GHz CPU with 4 cores and 8 logical processors is provided. Some operations make use of multi-threading.

- Running SCIA coupling and generating transfer functions: 5m-10m
- Single 1 hour wave spectrum fatigue calculation at specified coordinate: 6s-7s
- Single 1 hour wave spectrum fatigue calculation across full gate with 480 nodes: 4m-5m (4 threads)
- Fatigue calculation at specified coordinate for 1483 load cases: 35m-40m (8 threads)
- Monte Carlo simulation of 1000 lifetimes: 1m10s-1m20s

A.1. Spectrum definition

```
""" Generates either a JONSWAP- or a TMA-spectrum,
based on the wind velocity and average water depth.

"""
import random
import numpy as np
from scipy.optimize import root
import matplotlib.pyplot as plt
from src.configuration import g, N_HOURS, F, C_ts

def jonswap(u_wind, depth, timestep):
    """Generates a JONSWAP spectrum based on the wind velocity,
    the average water depth, and a timestep provided by the generator.

    Parameters:
    u_wind: Wind velocity of load event (m/s)
    depth:  Average water depth during load event (m)
    timestep: Desired timestep of final water level series (s)

    Returns:
    freqs: Frequencies of JONSWAP spectrum (Hz)
    amp: Amplitude spectrum values (m)
    k: Wave numbers (rad/m)

    """

    ## Define frequencies
    f0 = 1/(N_HOURS*3600)
    freqs = np.fft.rfftfreq(int(N_HOURS*3600/timestep), timestep)
```

```
    ## Determine k for each frequency. Made faster with Airy wave theory
    def wavenumber(x,f):
        return (2*np.pi*f)**2 - x*g*np.tanh(x*depth)
    shallow_limit = np.sqrt(2*np.pi*g/(20*depth)*np.tanh(2*np.pi/20))/(2*np.pi)
    deep_limit = np.sqrt(np.pi*g/(depth)*np.tanh(np.pi))/(2*np.pi)

    k = np.zeros(len(freqs))
    for i,f in enumerate(freqs):
        if f < 0.5*shallow_limit:       # Factor 0.5 to make transition smoother
            k[i] = 2*np.pi*f/np.sqrt(g*depth)
        elif f > 1.5*deep_limit:        # Factor 1.5 to make transition smoother
            k[i] = (2*np.pi*f)**2/g
        else:
            k[i] = root(wavenumber, 0.01, args=(f)).x[0]

    if u_wind == 0:
        return freqs,np.zeros(len(freqs)),k

    # Lewis and Allos, 1990
    F_dim = g*F/u_wind**2               # Dimensionless fetch
    f_p_dim = 2.18*F_dim**-0.27         # Dimensionless peak frequency
    f_p = f_p_dim*g/u_wind              # peak frequency
    alpha = 0.0317*f_p_dim**0.67
    gamma = 5.87*f_p_dim**0.86
    sigma_a = 0.0547*f_p_dim**0.32
    sigma_b = 0.0783*f_p_dim**0.16

    # Creating spectrum
    amp = np.zeros(len(freqs), dtype='complex')
    phase = [random.uniform(-np.pi,np.pi) for _ in range(len(freqs))] # Generate random
                                                                       phases
    for i,f in enumerate(freqs):
        if f == 0:
            continue
        if f > f_p:
            sigma = sigma_a
        else:
            sigma = sigma_b
        pm_shape = alpha*g**2*(2*np.pi)**-4*f**-5*np.exp(-5/4*(f/f_p)**-4)
        S = pm_shape*gamma**np.exp(-0.5*((f/f_p-1)/sigma)**2)
        spec =  np.sqrt(S*f0*2)                 # From power density to amplitude
        amp[i] = spec*np.exp(1j*phase[i])       # Add random phase
    return freqs, amp, k

def TMA(f, amp_jon, k):
    """Creates a TMA spectrum from a JONSWAP-spectrum with the depth correction factor
                                                phi.

    Parameters:
    f: Frequencies of JONSWAP spectrum (Hz)
    amp_jon: Amplitude spectrum values of JONSWAP spectrum (m)
    k: Wave numbers (rad/m)

    Returns:
    amp_tma: New amplitude spectrum values (m)

    """

    k_inf = (2*np.pi*f)**2/g            # k for infinite depth
    dk_inf = 2*(2*np.pi)**2*f/g         # df/dk for intinite depth
    dk_d = np.gradient(k, f)            # df/dk for inputs
    phi = np.true_divide(k_inf, k, out=np.zeros_like(k), where=k>0)**3\
    *np.true_divide(dk_d, dk_inf, out=np.zeros_like(k), where=dk_inf>0)
    amp_tma = phi*amp_jon
    return amp_tma

def spectrum_generator(u_wind, depth, spec='TMA'):
    """Generates a spectrum from the wind velocity and average water depth.
    Defaults to the TMA-spectrum, but an unmodified JONSWAP spectrum can be
    created if desired.
```

```
    Parameters:
    u_wind: Wind velocity of load event (m/s)
    depth:  Average water depth of load event (m)
    spec: Spectrum type ("TMA"/"JONSWAP")

    Returns:
    f: Spectrum frequencies (Hz)
    amp_tma: New amplitude spectrum values (m)
    k: Wave numbers (rad/m)
    Hm0: Significant wave height (m)
    Tp: Peak period (s)

    """

    F_dim = g*F/u_wind**2              # Dimensionless fetch
    f_p_dim = 2.18*F_dim**-0.27        # Dimensionless peak frequency (Kahma and Calkoen
                                                1992)
    f_p = f_p_dim*g/u_wind             # peak frequency
    Tp = 1/f_p
    timestep = round(Tp/C_ts,3)
    f, amp, k = jonswap(u_wind, depth, timestep)
    if spec == 'TMA':
        amp = TMA(f,amp,k)
        Tp = 1/f[np.argmax(abs(amp))]
    elif spec != 'JONSWAP':
        print('error, wrong spectral type. Defaulting to JONSWAP')
    f0 = 1/(N_HOURS*3600)
    Hm0 = 4*np.sqrt(np.trapz(abs(amp)**2/(2*f0),f)) #4*sqrt(m0)
    return f, amp, k, Hm0, Tp
```

A.2. Pressure

```
"""This script computes the pressure on the gate surface due to a given wave spectrum
                                                """
import dill
import numpy as np
from scipy.interpolate import InterpolatedUnivariateSpline
from src.spec import spectrum_generator
from src.configuration import g, rho, cr, dt, t, H_LAKE, N_HOURS,\
                              tri_min, tri_mode, tri_max, beta_std, beta_mean
with open('../data/06_transferfunctions/current_case.pkl', 'rb') as file:
    GATE = dill.load(file)

def hydrostatic(hsea):
    """Calculates the net hydrostatic water pressure on the gate."""
    fhs_z     = []        # Hydrostatic pressure as function of z
    for i,z in enumerate(GATE.z_coords):
        if z < H_LAKE:
            fhs_lake = rho*g*(H_LAKE - z)
        else:
            fhs_lake = 0
        if z < hsea:
            fhs_sea = rho*g*(hsea - z)
        else:
            fhs_sea = 0
        fhs_z.append(fhs_sea-fhs_lake)
    return fhs_z

def linearwavetheory(amp_gate, k, h_sea):
    """Calculates the quasi-static wave pressure on the gate from a wave spectrum.

    Parameters:
    amp_gate: Reflected water level spectrum at the gate (m)
    k:  Wave numbers of spectrum (rad/m)
    h_sea: Average sea water level (m)

    Returns:
    fqs_fz: Quasi-static pressure spectrum (N/m2)
```

```
    """

    # Split spectrum based on whether it is deep, shallow, or intermediate water depth
    # Multiplied transition k's by factor to minimize discontinuities.
    shallow_k = 0.5*np.pi/(10*h_sea)
    deep_k = 2*np.pi/h_sea

    # Define precise function, and approximations for deep and shallow water (helps
                                                prevent overflow errors in cosh)
    def shallow(a):
        return a*rho*g
    def intermediate(a, k, z):
        return a*rho*g*np.cosh(k*z)/np.cosh(k*h_sea)
    def deep(a, k, z):
        return a*rho*g*np.exp(k*(z-h_sea))
    amp_shallow = amp_gate[k<shallow_k]
    amp_inter = amp_gate[(k>=shallow_k) & (k<=deep_k)]
    k_inter = k[(k>=shallow_k) & (k<=deep_k)]
    amp_deep = amp_gate[k>deep_k]
    k_deep = k[k>deep_k]

    ## Quasi-static pressure
    fqs_fz    = []
    for j, z in enumerate(GATE.z_coords):
        fqs_z =[]
        if z <= h_sea:
            p_shallow = shallow(amp_shallow)
            p_inter = intermediate(amp_inter, k_inter, z)
            p_deep = deep(amp_deep, k_deep, z)
            fqs_z = np.concatenate([p_shallow, p_inter, p_deep])
        else:
            fqs_z = np.zeros(len(k))
        fqs_fz.append(fqs_z)
    return np.array(fqs_fz)

def impactloads(wl_tot, tau_par):
    """Calculates the highly dynamic wave pressure on the gate due to
    impacts on the overhang.

    Parameters:
    wl_tot: Time series of water surface (m)

    Returns:
    impact_force_t: Time series of impact forces (N)

    """

    ## Interpolate and determine impact velocities
    t_eta = np.linspace(0,3600*N_HOURS,len(wl_tot))
    spl = InterpolatedUnivariateSpline(t_eta,wl_tot)
    wl_interpolated = spl(t)
    ## Find zero crossings and impact velocities
    pos = np.array(wl_interpolated < GATE.HEIGHT)
    crossings = (pos[:-1] & ~pos[1:]).nonzero()[0]
    impact_vel = np.diff(wl_interpolated)[crossings]/dt
    ## Generate probabilistic wave impact parameters and create wave forces
    tau = np.random.triangular(tau_par[0], tau_par[1], tau_par[2], size=len(impact_vel)
                                                    )
    beta = np.random.normal(beta_mean, beta_std, size=len(impact_vel))
    impact_vel = impact_vel/(tau*0.5)*beta
    impact_force_t = np.zeros(len(t))
    for i, crossing in enumerate(crossings):
        steps = np.int(np.ceil(tau[i]/dt/2)*2+1)
        slope_up = np.linspace(0,impact_vel[i],int((steps+1)/2))
        slope_down = np.linspace(impact_vel[i],0,int((steps+1)/2))
        pulse = np.concatenate([slope_up,slope_down[1:]])
        if (crossing+steps) < len(wl_interpolated)-1:
            impact_force_t[crossing:int(crossing+steps)] = pulse
    return impact_force_t

def pressure(u_wind, hsea, tau_par=[0.01,0.105,0.2], spec='TMA'):
```

```
    """Calculates the static, quasi-static, and highly dynamic wave pressures
    on the gate due to water level fluctuations and impacts on the overhang.

    Parameters:
    u_wind: Average wind velocity during load event (m/s)
    hsea: Average water level during load event (m)

    Returns:
    freqs: Frequencies of JONSWAP spectrum (Hz)
    pqs_f: Quasi-static pressure spectrum (N/m2)
    impact_force_t: Time series of impact forces (N)
    Hs: Significant wave height (m)
    Tp: Peak period (s)

    """

    h_sea_r = round(hsea,1) # so it fits mesh
    ## Generate JONSWAP spectrum
    freqs, amp, k, Hs, Tp = spectrum_generator(u_wind, h_sea_r, spec)
    amp_gate = (1+cr)*amp
    eta = np.fft.irfft(amp_gate)*len(k)
    pqs_f = linearwavetheory(amp_gate, k, h_sea_r)
    fhs_z = hydrostatic(h_sea_r)
    pqs_f[:,0] = fhs_z              # Add hydrostatic pressure at zero frequency

    wl_tot = eta + h_sea_r  # Add depth to wave fluctuations
    if (wl_tot < GATE.HEIGHT).all():
        return freqs, pqs_f, np.zeros(int(3600*N_HOURS/dt+1)), Hs, Tp
    impact_force_t = impactloads(wl_tot, tau_par)
    return freqs, pqs_f, impact_force_t, Hs, Tp
```

A.3. Wood and Peregrine pressure shape

```
'''Originally created in Matlab by B. Hofland, including all notes '''

import numpy as np
from src.configuration import rho, dz

def woodandperegrine(GATE):
    a = GATE.HEIGHT/GATE.Ly
    adz = dz/GATE.Ly

    x = np.transpose([np.linspace(0, GATE.WIDTH, int(GATE.WIDTH/0.005+1))]*(round((1/
                                                    adz)*a)+1))
    y = (200*GATE.WIDTH+1)*[np.linspace(0, a, int(a/adz+1))]
    z = x + np.multiply(1j, y)

    ## STEP 1 - CONFORMAL MAP
    w= np.cosh(np.multiply(np.pi/a, z))

    ## STEP 2 - TRANSLATION AND MAGNIFICATION
    M = 2/(np.cosh(np.pi/a)-1)
    N = M + 1
    h = M*w + N

    ## STEP 3 - CONFORMAL MAP 2
    zeta = a*np.arccosh(h)/np.pi
    ksi = np.real(zeta)
    eta = np.imag(zeta)

    ## set variables for integration over eta
    Nint     = 1000
    deta_int = a/Nint
    eta_int  = np.multiply([x - 1/2 for x in range(1,1001)], deta_int)
    b_int    = (np.cos(np.multiply(np.pi/a, eta_int))-N)/M
    P = 0

    for n in range(1,31):
        alphan = (n-1 + 1/2)*np.pi/a
```

```
        # I sum from n=0 , so take n-1 such that n can be used as index
        # numerical integration to determine Fourier coefficients
        An = 2/alphan/a * sum(np.sin(np.pi*eta_int/a)*np.cos(alphan*eta_int)/np.sqrt(
                                                    b_int**2-1) / M ) * deta_int
        # says Am in paper, I don't see where a comes from
        # % sum Fourier modes to get P
        P += An * np.cos(alphan*eta) * np.exp(-alphan*ksi)
        # not sure about the real() in right expression in paper
    return P[1,:]*rho*GATE.Ly   #per m width
```

A.4. Stress calculation

```
""" Calculates the stress at a specified point in the gate,
based on previously calculated quasi-static stress spectra and wave impact time series.

"""
import os
import sys
import dill
import numpy as np
import matplotlib.pyplot as plt
import pyfftw
from scipy.interpolate import interp1d, InterpolatedUnivariateSpline
from src.configuration import N_HOURS, dz, t, n_z
from src.woodandperegrine import woodandperegrine
pyfftw.config.NUM_THREADS = 4
root_dir = os.path.join(os.getcwd(), '..')
sys.path.append(root_dir)
# Load system properties
with open('../data/06_transferfunctions/current_case.pkl', 'rb') as file:
    GATE = dill.load(file)
directory = '../data/06_transferfunctions/'+str(GATE.case)+'/FRF_'+str(GATE.case)+'_'+
                                            str(GATE.n_modes)+'modes.npy'
try:
    frf_intpl = np.load(directory, mmap_mode='r')
    # Map mode only loads parts of 3Gb matrix when needed instead of keeping it all in
                                                RAM.
except OSError:
    print("An exception occurred: no FRF found at "+directory)
# Stress functions
def qs_discretize(pqs_f):
    """Integrates the quasi-static pressure spectrum over the gate sections."""
    # does not integrate over x!
    # Becomes problem if segments are variable or inputs not uniform in x-direction
    return np.array([np.sum(np.split(pqs_f, GATE.ii_z[1:-1], axis=0)[i], axis=0)*dz/\
                    (GATE.z_coords[GATE.ii_z[i+1]]-GATE.z_coords[GATE.ii_z[i]])\
                    for i in range(n_z)])

def imp_discretize(impact_force_t):
    """Integrates the impulsive pressure time series over the gate sections."""
    Pz_impact_U1 = woodandperegrine(GATE)
    # Construct force-time matrix for all z-coordinates
    p_matrix = np.zeros((len(impact_force_t), len(Pz_impact_U1)))
    np.multiply.outer(impact_force_t, Pz_impact_U1, out = p_matrix)
    # does not integrate over x!
    # Becomes problem if segments are variable or inputs not uniform in x-direction
    return np.array([np.sum(np.split(p_matrix, GATE.ii_z[1:-1], axis=1)[i], axis=1)*dz/
                                                \
                    (GATE.z_coords[GATE.ii_z[i+1]]-GATE.z_coords[GATE.ii_z[i]]) for i
                                                            in range(n_z)])

def stress_time(freqs, pqs_f, impact_force_t, coords, stresstype = None,
                plot=False, plotrange = [50,80]):
    """Generates a time series of the stress at a given gate coordinate.

    Parameters:
    freqs: Frequencies of JONSWAP spectrum (Hz)
    pqs_f:  Quasi-static wave pressure spectrum (N/m2)
    impact_force_t: Wave impact time series (s)
```

```
    coords: X,Y,Z gate coordinates (m)
    plot: Whether to plot the result (True/False)

    Returns:

    F_tot: Wave force integrated over gate height (N/m)
    response_tot_t: Time series of gate stress at coordinate (N/m2)

    """

    # IRFFT of quasi-static part
    pqs_sections = qs_discretize(pqs_f)
    q_tot = pqs_sections.sum(axis=(0))*(GATE.HEIGHT/n_z)
    # N/m (only works if sections are of constant size)
    # Interpolate FRF to correct resolution
    func = interp1d(GATE.f_tf, GATE.FRF, axis=3)
    frf_qs = func(freqs)
    if stresstype == 'pos':
        mode_shape = GATE.stresspos3D.loc[coords].to_list()
    elif stresstype == 'neg':
        mode_shape = GATE.stressneg3D.loc[coords].to_list()
    else:
        if sum(GATE.stressneg3D.loc[coords] - GATE.stresspos3D.loc[coords])>0:
            mode_shape = GATE.stressneg3D.loc[coords].to_list()
        else:
            mode_shape = GATE.stresspos3D.loc[coords].to_list()
    response_qs = np.zeros(len(freqs), dtype=np.complex)
    np.einsum('jl,ijkl,k->l',pqs_sections, frf_qs, mode_shape,
              out=response_qs, dtype=np.complex)
    response_qs_t = len(response_qs)*pyfftw.interfaces.numpy_fft.irfft(response_qs)
    t_qs = np.linspace(0, 3600*N_HOURS, 2*(len(pqs_f[0])-1))
    # Interpolate qs
    func_qs = InterpolatedUnivariateSpline(t_qs, response_qs_t)
    resp_qs_intpl = func_qs(t)

    F_qs = pyfftw.interfaces.numpy_fft.irfft(q_tot)*len(q_tot)
    func_F_qs = InterpolatedUnivariateSpline(t_qs, F_qs)
    F_qs_intpl = func_F_qs(t)

    # IRFFT of impulsive part
    p_sections = imp_discretize(impact_force_t)
    p_imp_f = pyfftw.interfaces.numpy_fft.rfft(p_sections, axis=1)
    # Find total force
    F_gate = p_sections.sum(axis=(0))*(GATE.HEIGHT/n_z)
    # N/m over width (only works if sections are of constant size)

    # Compute response for modes
    response_imp = np.zeros(len(GATE.f_intpl), dtype=np.complex)
    np.einsum('jl,ijkl,k->l', p_imp_f, frf_intpl, mode_shape,
              out=response_imp, dtype=np.complex)
    response_imp_t = pyfftw.interfaces.numpy_fft.irfft(response_imp)
    response_imp_t = np.append(response_imp_t,response_imp_t[-1])

    # Combine responses and forces
    response_tot_t = resp_qs_intpl + response_imp_t
    F_tot = F_qs_intpl + F_gate
    if plot:
        plot_stress_time(F_tot, -response_tot_t, coords, plotrange)
    return F_tot, response_tot_t
```

A.5. Fatigue

```
""" Functions to calculate and plot the fatigue damage for a stress time series.
"""
import rainflow
import numpy as np
import matplotlib.pyplot as plt
from src.utilities import PlotText
from src.pressure import pressure
```

```
from src.stress import stress_time
from src.configuration import gamma_Mf, gamma_Ff

# Characteristic values
m1 = 3
m2 = 5
Nc = 2e6
Nd = 5e6

def fatigue(response_t, cat):
    """Calculates the fatigue according to the Eurocode two-slope Miner method.

    Parameters:
    response_t: Time series of the gate stress at a certain point (Pa)
    cat: Detail category of material at coordinate (MPa)

    Returns:

    D: Fatigue damage factor (-)

    """
    amp, cycles = np.array(rainflow.count_cycles(response_t, nbins=None)).T

    # Palmgren-Miner
    loads = amp/10**6*gamma_Ff
    sigma_c = cat/gamma_Mf
    sigma_D = (2/5)**(1/3)*sigma_c
    sigma_L = (5/100)**(1/5)*sigma_D

    sig_i = loads[loads>sigma_D]
    n_i = cycles[loads>sigma_D]
    sig_j = loads[loads<=sigma_D]
    n_j = cycles[loads<=sigma_D]
    Q = sum(n_i*sig_i**3) + sum(n_j*sig_j**3*(sig_j/sigma_D)**2)
    D_eq = Q/(Nd*sigma_D**3)
    return D_eq
```

A.6. Lifetime fatigue

```
""" Functions to evaluate the fatigue over the lifetime of the gate at a specified
                                                coordinate,
    and plot the results.
"""
import os
import numpy as np
import pandas as pd
import dill
import multiprocess
from src.pressure import pressure
from src.stress  import stress_time
from src.fatigue import fatigue
from src.configuration import hlife
import matplotlib.pyplot as plt
import matplotlib.ticker as mtick
from mpl_toolkits.axes_grid1 import make_axes_locatable
TUred = "#c3312f"
TUblue = "#00A6D6"
TUgreen = "#00a390"
# Load system properties
with open('../data/06_transferfunctions/current_case.pkl', 'rb') as file:
    GATE = dill.load(file)
def simulations(runs, version, average_only=False, std=0.1):
    """Runs probabilistic simulations on previously computed list of fatigue load cases
                                                .

    Parameters:
    runs: Amount of simulations to run (-)
    version: Version name under which results are stored
    average_only: If True, the function only calculates the expected value,
```

```
                rather than performing a Monte Carlo simulation.

    Returns:

    fig = Figure of cumulative fatigue development and relative importance of load
                                                cases.
    D_expected = Expected value of lifetime fatigue damage.
    totals = List of final lifetime fatigue values for all simulations.
    [maxes,means,mins]: List of maximum, mean, and minimum values
                        across all simulation at every point in time.

    """
    rng = np.random.default_rng()
    case_directory = '../data/07_fatigue/%s'%GATE.case
    if not os.path.exists(case_directory):
        os.mkdir(case_directory)
    with open('%s/%s.pkl' %(case_directory, version), 'rb') as f:
        cases_calc = dill.load(f).sort_values(['D'])
    cases_calc['damage'] = 100*cases_calc['D']*cases_calc['p'].to_list() # in %
    # Add 'empty' cases that were filtered out earlier
    cases = cases_calc.append({'mean_u':0,'mean_h':6,'D':0,'p':1-sum(cases_calc['p']),
                                                    'damage':0},
                              ignore_index=True)
    T = int(hlife*24*365.25)
    t = np.linspace(0,hlife,T)
    # Expected lifetime fatigue
    D_expected = sum(cases['damage'])*T
    if average_only:
        return D_expected

    runs_path = '%s/%s_lifetimes_v%s.pkl'%(case_directory, runs, version)
    if os.path.exists(runs_path):
        print("Using old simulations from %s"%runs_path)
        with open(runs_path, 'rb') as file:
            fig, D_expected, totals, [maxes,means,mins] = dill.load(file)
    else:
        print('Running %s Monte Carlo simulations...'%runs)
        # Randomly generate 100 years of hourly simulations, 'n' at a time
        n = 100  #chunk row size
        totals = []
        maxes = np.zeros(T)
        mins = np.ones(T)*10**6
        means = np.zeros(T)
        for i in range(int(np.ceil(runs/n))):
            events = rng.choice(cases['D'], [n,T], p=cases['p'])
            res = np.random.normal(events, std*events)*100 #in %
            cumulative=np.cumsum(res,axis=1)
            totals += np.max(cumulative,axis=1).tolist()
            means += cumulative.sum(axis=0)
            maxes = np.max(np.vstack((maxes,cumulative)),axis=0)
            mins  = np.min(np.vstack((mins,cumulative)),axis=0)
        means /= runs
    fig, (ax1,ax2) = plt.subplots(1,2,figsize=[12,5])
    ax1.grid(alpha=0.5)
    ax1.hlines(100,0,100,ls='--', alpha=0.5, lw=3, color='#00A6D6')
    ax1.set_title('Damage accumulation for '+str(runs)+' simulations')
    ax1.set_xlim(0,hlife)
    ax1.set_ylim(0,120)
    ax1.plot(t,maxes,label='Upper bound', color='#c3312f')
    ax1.plot(t,means,label='Average', color='gray')
    ax1.plot(t,mins,label='Lower bound', color='#00A6D6')
    ax1.fill_between(t, mins, maxes, alpha=0.1, color='gray')
    ax1.set_xlabel('Time [years]')
    ax1.set_ylabel('Fatigue damage [%]')
    ax1.legend(loc='lower right')

    with open('../data/03_loadevents/currentbins.cp.pkl', 'rb') as f:
        x_u, x_h, u_bins, h_bins = dill.load(f)
    hist = ax2.hist2d(cases_calc['mean_h'], cases_calc['mean_u'], bins=[h_bins,u_bins],
                      range=[(min(x_h),max(x_h)),(min(x_u),max(x_u))],
                      weights=cases_calc['damage']*100, cmap='Blues', cmin=1e-6)
```

```
    divider = make_axes_locatable(ax2)
    cax = divider.append_axes('right', size='5%', pad=0.05)
    cb = fig.colorbar(hist[3], cax=cax, orientation='vertical')
    cb.ax.yaxis.set_major_formatter(mtick.PercentFormatter())
    ax2.set_title('Damage contribution per load case')
    ax2.set_xlabel('d [m]')
    ax2.set_ylabel('$U_{10}$ [m/s]')
    ax2.set_xticks(np.linspace(min(x_h), max(x_h), h_bins+1), minor=True)
    ax2.set_yticks(np.linspace(min(x_u), max(x_u), u_bins+1), minor=True)
    ax2.set_xlim(5,9)
    ax2.set_ylim(min(cases['mean_u']),50)
    with open(runs_path, 'wb') as f:
        dill.dump([fig, D_expected, totals, [maxes,means,mins]], f)
    plt.close(fig)
    return fig, D_expected, totals, [maxes,means,mins]
```

List of Figures

List of Tables

Bibliography

[1] Technisch rapport ontwerpbelastingen voor het rivierengebied. Technical report, 2007.

[2] KNMI'14-klimaatscenario's voor Nederland; Leidraad voor professionals in klimaatadaptatie. Technical report, KNMI, 2015.

[3] SCIA Engineer - Theory: Physical and shape orthotropy of plates, 2016. URL https://help.scia.net/download/16.0/en/OtrhotropTB_enu.pdf.

[4] S. Been. Smoothed Particle Hydrodynamic Modelling of Wave Impact. Delft University of Technology, 2020. doi: http://resolver.tudelft.nl/uuid:da456924-c5e4-4e93-8780-cc0853850ddc.

[5] J. Blaauwendraad. Plate analysis, theory and application, volume 1. TU Delft, Civil Engineering and Geosciences, Section of Structural Mechanics, 2006.

[6] J. Blaauwendraad. Plates and FEM. Springer, 2010. doi: 10.1007/978-90-481-3596-7.

[7] E. Bouws, H. Günther, W. Rosenthal, and C.L. Vincent. Similarity of the wind wave spectrum in finite depth water: 1. Spectral form. Journal of Geophysical Research: Oceans, 90(C1), 1985. doi: https://doi.org/10.1029/JC090iC01p00975.

[8] E. de Almeida and B. Hofland. Validation of pressure-impulse theory for standing wave impact loading on vertical hydraulic structures with short overhangs. Coastal Engineering, 159, 2020. doi: https://doi.org/10.1016/j.coastaleng.2020.103702.

[9] T. Dirlik. Application of Computers in Fatigue. 1985.

[10] European Committee for Standardisation. Eurocode 3: Ontwerp en berekening van staalconstructies - Deel 1-9: Vermoeiing. Technical report, 2012.

[11] H.W. Groenendijk. Shallow foreshore wave height statistics. Technical report, 1989.

[12] J. Groeneweg et al. Hydraulische Randvoorwaarden. Deltares, 2013.

[13] K Hasselmann et al. Measurements of wind-wave growth and swell decay during the Joint North Sea Wave Project (JONSWAP). Jan 1973. doi: http://resolver.tudelft.nl/uuid:f204e188-13b9-49d8-a6dc-4fb7c20562fc.

[14] L.H. Holthuijsen. Waves in Oceanic and Coastal Waters. Cambridge University Press, 2007. ISBN 978-0-521-86028-4.

[15] Stichting Koninklijk Nederlands Normalisatie Instituut. NEN-EN-ISO 19902: Aardolie- en aardgasindustrie - Vaste buitengaatse staalconstructies. Technical report, Stichting Koninklijk Nederlands Normalisatie Instituut, 2020.

[16] KNMI. Daggegevens van het weer in nederland, 2020. URL https://waterinfo.rws.nl/#!/nav/bulkdownload/huidige-selectie/. data retrieved in October 2020.

[17] P.A. Kolkman and T.H.G. Jongeling. Dynamic behaviour of hydraulic structures. Deltares, 2007.

[18] B. Le Méhauté. An introduction to hydrodynamics and water waves. Springer, 1976. ISBN 978-0-387-07232-6.

[19] A.W. Lewis and R.N. Allos. JONSWAP's parameters: Sorting out the inconsistencies. Ocean Engineering, 17(4):409–415, 1990.

[20] M. Matsuishi and T. Endo. Fatigue of metals subjected to varying stress. 1968.

[21] S. Mazaheri and Z. Ghaderi. Shallow Water Wave Characteristics in Persian Gulf. Journal of Coastal Research, 2011.

[22] R.D. Mindlin. Influence of rotary inertia and shear on flexural motions isotropic, elastic plates. ASME Journal of Applied Mechanics, 18:1031–6, 1951.

[23] H. Mitsuyasi. Experimental study on wave force against a wall. Coastal Engineering in Japan, 5:23–47, 1966.

[24] W.F. Molenaar and M.Z. Voorendt. Manual Hydraulic Structures. Delft University of Technology, 2018. ISBN 978-0-387-07232-6.

[25] M. Mršnik, J. Slavič, and M. Boltežar. Frequency-domain methods for a vibration-fatigue-life estimation. International Journal of Fatigue, 47:8–17, 2016. doi: 10.1016/j.ijfatigue.2012.07.005.

[26] M. Mršnik, J. Slavič, and M. Boltežar. Vibration fatigue using modal decomposition. Mechanical Systems and Signal Processing, 98:548–556, 2018. doi: 10.1016/j.ymssp.2017.03.052.

[27] M. K. Ochi and E. N. Hubble. Six-parameter wave spectra. Proceedings of the 15th Coastal Engineering Conference, pages 301–328, 1976.

[28] C. Ramkema. Stormvloedkering Oosterschelde: Golfklappen tegen betonnen roosterschuiven. Technical report, 1978.

[29] Rijkswaterstaat. Rijkswaterstaat waterinfo, 2020. URL `http://projects.knmi.nl/klimatologie/daggegevens/selectie.cgi`. data retrieved in October 2020.

[30] M.W. Sracic and W.J. Elke. Effect of Boundary Conditions on Finite Element Submodeling. Nonlinear Dynamics, 1, 2019. doi: https://doi.org/10.1007/978-3-319-74280-9_16.

[31] O.C. Tieleman. The dynamic behaviour of pump gates in the Afsluitdijk, 2015.

[32] O.C. Tieleman, A. Tsouvalas, B. Hofland, Y. Peng, and S.N. Jonkman. A three dimensional semi-analytical model for the prediction of gate vibrations immersed in fluid. Marine Structures, 65:134–153, 2019. doi: https://doi.org/10.1016/j.marstruc.2018.12.007.

[33] O.C. Tieleman, A. Tsouvalas, B. Hofland, E. de Almeida, and S.N. Jonkman. A fluid-structure interaction model for assessing the safety of flood gate vibrations due to wave impacts. 2020.

[34] A. Tsouvalas and A. Metrikine. Parametric study of noise reduction by an air-bubble curtain in offshore pile driving. Journal of Sound and Vibration, 371:150–170, 2016. doi: http://resolver.tudelft.nl/uuid:ada8888d-cc6d-42ae-835a-83323b48c5b4.

[35] A. Tsouvalas, A. Metrikine, and A.V. Metrikine. The significance of the evanescent spectrum in structure-waveguide interaction problems. The Journal of the Acoustical Society of America, 138:2574–2588, 2015. doi: https://doi.org/10.1121/1.4932016.

[36] R.F. Vorderegger. Optimization of gate design in the Afsluitdijk based on dynamic wave impact, 2019.

[37] D.J. Wood and D.H. Peregrine. Wave impact beneath a horizontal surface. Coastal Engineering, 1(25), Jan 1996. doi: https://doi.org/10.9753/icce.v25.\%25p.

[38] X.Y. Zheng, S. Gao, and Y. Huang. Cross-mode couplings for the fatigue damage evaluation of tri-modal Gaussian processes. Ocean Engineering, 202, 2020. doi: https://doi.org/10.1016/j.oceaneng.2020.107177.